Title: The landscape of tolerated genetic variation in humans and primates

Authors: Hong Gao[1]†, Tobias Hamp[1]†, Jeffrey Ede[1], Joshua G. Schraiber[1], Jeremy McRae[1], Moriel Singer-Berk[2], Yanshen Yang[1], Anastasia Dietrich[1], Petko Fiziev[1], Lukas Kuderna[1,3], Laksshman Sundaram[1], Yibing Wu[1], Aashish Adhikari[1], Yair Field[1], Chen Chen[1], Serafim Batzoglou[1], Francois Aguet[1], Gabrielle Lemire[2,4], Rebecca Reimers[4], Daniel Balick[5], Mareike C. Janiak[6], Martin Kuhlwilm[3,7,8], Joseph D. Orkin[3,9], Shivakumara Manu[10,11], Alejandro Valenzuela[3], Juraj Bergman[12,13], Marjolaine Rouselle[12], Felipe Ennes Silva[14,15], Lidia Agueda[16], Julie Blanc[16], Marta Gut[16], Dorien de Vries[6], Ian Goodhead[6], R. Alan Harris[17], Muthuswamy Raveendran[17], Axel Jensen[18], Idriss S. Chuma[19], Julie Horvath[20,21,22,23,24], Christina Hvilsom[25], David Juan[3], Peter Frandsen[25], Fabiano R. de Melo[26], Fabricio Bertuol[27], Hazel Byrne[28], Iracilda Sampaio[29], Izeni Farias[27], João Valsecchi do Amaral[30,31,32], Malu Messias[33], Maria N. F. da Silva[34], Mihir Trivedi[11], Rogerio Rossi[35], Tomas Hrbek[27,36], Nicole Andriaholinirina[37], Clément J. Rabarivola[37], Alphonse Zaramody[37], Clifford J. Jolly[38], Jane Phillips-Conroy[39], Gregory Wilkerson[40], Christian Abee[40], Joe H. Simmons[40], Eduardo Fernandez-Duque[41], Sree Kanthaswamy[42], Fekadu Shiferaw[43], Dongdong Wu[44], Long Zhou[45], Yong Shao[44], Guojie Zhang[45,46,47,48,49], Julius D. Keyyu[50], Sascha Knauf[51], Minh D. Le[52], Esther Lizano[3,53], Stefan Merker[54], Arcadi Navarro[3,55,56,57], Thomas Batallion[12], Tilo Nadler[58], Chiea Chuen Khor[59], Jessica Lee[60], Patrick Tan[59,61,62], Weng Khong Lim[61,62,63], Andrew C. Kitchener[64,65], Dietmar Zinner[66,67,68], Ivo Gut[16], Amanda Melin[69,70], Katerina Guschanski[18,71], Mikkel Heide Schierup[12], Robin M. D. Beck[6], Govindhaswamy Umapathy[10,11], Christian Roos[72], Jean P. Boubli[6], Monkol Lek[73], Shamil Sunyaev[74,5], Anne O'Donnell[2,4,75], Heidi Rehm[2,75], Jinbo Xu[1,76], Jeffrey Rogers[17]*, Tomas Marques-Bonet[3,16,53,55]*, Kyle Kai-How Farh[1]*

Affiliations:

[1]Illumina Artificial Intelligence Laboratory, Illumina Inc.; Foster City, California, 94404, USA.

[2]Program in Medical and Population Genetics, Broad Institute of MIT and Harvard; Boston, Massachusetts, 02142, USA.

[3]Institute of Evolutionary Biology (UPF-CSIC); PRBB, Dr. Aiguader 88, 08003 Barcelona, Spain.

[4]Division of Genetics and Genomics, Department of Pediatrics, Boston Children's Hospital, Harvard Medical School; Boston, Massachusetts, 02115, USA.

[5]Division of Genetics, Brigham and Women's Hospital, Harvard Medical School; Boston, Massachusetts, 02115, USA.
[6]School of Science, Engineering & Environment, University of Salford; Salford, M5 4WT, United Kingdom.
[7]Department of Evolutionary Anthropology, University of Vienna; Djerassiplatz 1, 1030, Vienna, Austria.
[8]Human Evolution and Archaeological Sciences (HEAS), University of Vienna; 1030, Vienna, Austria.
[9]Département d'anthropologie, Université de Montréal; 3150 Jean-Brillant, Montréal, QC, H3T 1N8, Canada.
[10]Academy of Scientific and Innovative Research (AcSIR); Ghaziabad, 201002, India.

[11]Laboratory for the Conservation of Endangered Species, CSIR-Centre for Cellular and Molecular Biology; Hyderabad, 500007, India.
[12]Bioinformatics Research Centre, Aarhus University; Aarhus, 8000, Denmark.
[13]Section for Ecoinformatics & Biodiversity, Department of Biology, Aarhus University; Aarhus, 8000, Denmark.
[14]Research Group on Primate Biology and Conservation, Mamirauá Institute for Sustainable Development; Estrada da Bexiga 2584, Tefé, Amazonas, CEP 69553-225, Brazil.
[15]Faculty of Sciences, Department of Organismal Biology, Unit of Evolutionary Biology and Ecology, Université Libre de Bruxelles (ULB); Avenue Franklin D. Roosevelt 50, 1050, Brussels, Belgium.
[16]CNAG-CRG, Centre for Genomic Regulation (CRG), Barcelona Institute of Science and Technology (BIST); Baldiri i Reixac 4, 08028, Barcelona, Spain.
[17]Human Genome Sequencing Center and Department of Molecular and Human Genetics, Baylor College of Medicine; Houston, Texas, 77030, USA.
[18]Department of Ecology and Genetics, Animal Ecology, Uppsala University; SE-75236, Uppsala, Sweden.
[19]Tanzania National Parks; Arusha, Tanzania.
[20]North Carolina Museum of Natural Sciences; Raleigh, North Carolina, 27601, USA.
[21]Department of Biological and Biomedical Sciences, North Carolina Central University; Durham, North Carolina , 27707, USA.
[22]Department of Biological Sciences, North Carolina State University; Raleigh, North Carolina , 27695, USA.
[23]Department of Evolutionary Anthropology, Duke University; Durham, North Carolina , 27708, USA.
[24]Renaissance Computing Institute, University of North Carolina at Chapel Hill, Chapel Hill, NC 27599, USA.
[25]Copenhagen Zoo; 2000 Frederiksberg, Denmark.
[26]Universidade Federal de Viçosa; Viçosa, 36570-900, Brazil.
[27]Universidade Federal do Amazonas, Departamento de Genética, Laboratório de Evolução e Genética Animal (LEGAL); Manaus, Amazonas, 69080-900, Brazil.
[28]Department of Anthropology, University of Utah; Salt Lake City, Utah, 84102, USA.
[29]Universidade Federal do Para; Guamá, Belém - PA, 66075-110, Brazil.
[30]Research Group on Terrestrial Vertebrate Ecology, Mamirauá Institute for Sustainable Development; Tefé, Amazonas, 69553-225, Brazil.
[31]Rede de Pesquisa para Estudos sobre Diversidade, Conservação e Uso da Fauna na Amazônia – RedeFauna; Manaus, Amazonas, 69080-900, Brazil.
[32]Comunidad de Manejo de Fauna Silvestre en la Amazonía y en Latinoamérica – ComFauna; Iquitos, Loreto, 16001, Peru.
[33]Universidade Federal de Rondonia; Porto Velho, Rondônia, 78912-000, Brazil.
[34]Instituto Nacional de Pesquisas da Amazonia; Petrópolis, Manaus - AM, 69067-375, Brazil.
[35]Universidade Federal do Mato Grosso; Boa Esperança, Cuiabá - MT, 78060-900, Brazil.
[36]Department of Biology, Trinity University; San Antonio, Texas, 78212, USA.
[37]Life Sciences and Environment, Technology and Environment of Mahajanga, University of Mahajanga; Mahajanga, 401, Madagascar.
[38]New York University; New York City, 10012, USA.

[39]Washington University in St. Louis; St. Louis, Missouri,63130, USA.
[40]Keeling Center for Comparative Medicine and Research, MD Anderson Cancer Center; Houston, Texas, 77030, USA.
[41]Yale University; New Haven, Connecticut, 06520, USA.
[42]Arizona State University; Tempe, Arizona, 85281, USA.
[43]Hawassa University; Hawassa, 005, Ethiopia.
[44]State Key Laboratory of Genetic Resources and Evolution, Kunming Institute of Zoology, Chinese Academy of Sciences; Kunming, Yunnan, 650223, China.
[45]Center for Evolutionary & Organismal Biology, Zhejiang University School of Medicine, Hangzhou, 310058, China.
[46]Villum Center for Biodiversity Genomics, Section for Ecology and Evolution, Department of Biology, University of Copenhagen; Copenhagen, DK-2100, Denmark.
[47]State Key Laboratory of Genetic Resources and Evolution, Kunming Institute of Zoology, Chinese Academy of Sciences, Kunming, Yunnan, 650223, China
[48]Liangzhu Laboratory, Zhejiang University Medical Center; 1369 West Wenyi Road, Hangzhou, 311121, China
[49]Women’s Hospital, School of Medicine, Zhejiang University; 1 Xueshi Road, Shangcheng District, Hangzhou, 310006, China
[50]Tanzania Wildlife Research Institute (TAWIRI), Head Office; P.O.Box 661, Arusha, Tanzania.
[51]Institute of International Animal Health/One Health, Friedrich-Loeffler-Institut, Federal Research Institute for Animal Health; 17493 Greifswald - Isle of Riems, Germany.
[52]Department of Environmental Ecology, Faculty of Environmental Sciences, University of Science and Central Institute for Natural Resources and Environmental Studies, Vietnam National University; Hanoi, 100000, Vietnam.
[53]Institut Català de Paleontologia Miquel Crusafont, Universitat Autònoma de Barcelona, Barcelona, Spain; Catalan Institution of Research and Advanced Studies (ICREA), Barcelona, Spain
[54]Department of Zoology, State Museum of Natural History Stuttgart; 70191 Stuttgart, Germany.
[55]Institució Catalana de Recerca i Estudis Avançats (ICREA) and Universitat Pompeu Fabra, Pg. Luís Companys 23, Barcelona, 08010, Spain.
[56]Centre for Genomic Regulation (CRG), The Barcelona Institute of Science and Technology; Av. Doctor Aiguader, N88, Barcelona, 08003, Spain.
[57]BarcelonaBeta Brain Research Center, Pasqual Maragall Foundation; C. Wellington 30, Barcelona, 08005, Spain.
[58]Cuc Phuong Commune; Nho Quan District, Ninh Binh Province, 430000, Vietnam.
[59]Genome Institute of Singapore (GIS), Agency for Science, Technology and Research (A*STAR), 60 Biopolis Street, Genome, Singapore 138672, Republic of Singapore.
[60]Mandai Nature; 80 Mandai Lake Road, Singapore 729826, Republic of Singapore.
[61]SingHealth Duke-NUS Institute of Precision Medicine (PRISM); Singapore 168582, Republic of Singapore.
[62]Cancer and Stem Cell Biology Program, Duke-NUS Medical School; Singapore 168582, Republic of Singapore.
[63]SingHealth Duke-NUS Genomic Medicine Centre; Singapore 168582, Republic of Singapore.
[64]Department of Natural Sciences, National Museums Scotland; Chambers Street, Edinburgh, EH1 1JF, UK.

[65]School of Geosciences, University of Edinburgh; Drummond Street, Edinburgh, EH8 9XP, UK.
[66]Cognitive Ethology Laboratory, Germany Primate Center, Leibniz Institute for Primate Research; 37077 Göttingen, Germany.
[67]Department of Primate Cognition, Georg-August-Universität Göttingen; 37077 Göttingen, Germany.
[68]Leibniz Science Campus Primate Cognition; 37077 Göttingen, Germany.
[69]Department of Anthropology & Archaeology and Department of Medical Genetics
[70]Alberta Children's Hospital Research Institute; University of Calgary; 2500 University Dr NW T2N 1N4, Calgary, Alberta, Canada.
[71]Institute of Evolutionary Biology, School of Biological Sciences, University of Edinburgh; Edinburgh, EH8 9XP, UK.
[72]Gene Bank of Primates and Primate Genetics Laboratory, German Primate Center, Leibniz Institute for Primate Research; Kellnerweg 4, 37077 Göttingen, Germany.

[73]Department of Genetics, Yale School of Medicine; New Haven, Connecticut, 06520, USA.

[74]Department of Biomedical Informatics, Harvard Medical School, Boston, Massachusetts, 02115, USA.

[75]Analytic and Translational Genetics Unit, Department of Medicine, Massachusetts General Hospital and Harvard Medical School; Boston, Massachusetts, 02115, USA.

[76]Toyota Technological Institute at Chicago; Chicago, Illinois, 60637, USA.

† These authors contributed equally to this work

*Corresponding authors. Email: tomas.marques@upf.edu, jr13@bcm.edu, kfarh@illumina.com

Abstract: Personalized genome sequencing has revealed millions of genetic differences between individuals, but our understanding of their clinical relevance remains largely incomplete. To systematically decipher the effects of human genetic variants, we obtained whole genome sequencing data for 809 individuals from 233 primate species, and identified 4.3 million common protein-altering variants with orthologs in human. We show that these variants can be inferred to have non-deleterious effects in human based on their presence at high allele frequencies in other primate populations. We use this resource to classify 6% of all possible human protein-altering variants as likely benign and impute the pathogenicity of the remaining 94% of variants with deep learning, achieving state-of-the-art accuracy for diagnosing pathogenic variants in patients with genetic diseases.

One Sentence Summary: Deep learning classifier trained on 4.3 million common primate missense variants predicts variant pathogenicity in humans.

Main Text:

A scalable approach for interpreting the effects of human genetic variants and their impact on disease risk is urgently needed to realize the promise of personalized genomic medicine (*1-3*). Out of more than 70 million possible protein-altering variants in the human genome, only ~0.1% are annotated in clinical variant databases such as ClinVar (*4*), with the remainder being variants of uncertain clinical significance (*5, 6*). Despite collaborative efforts by the scientific community, the rarity of most human genetic variants has meant that progress towards deciphering personal genomes has been incremental (*7, 8*). Consequently, clinical sequencing tests frequently return without definitive diagnoses, a frustrating outcome for both patients and clinicians (*9, 10*). In certain cases, patients have needed to be recontacted and diagnoses reversed when the presumed pathogenic variant was later found to be a common variant in previously understudied human populations (*11-13*). Common variants can often be ruled out as the cause of penetrant genetic disease, since their high frequency in the population indicates that they are tolerated by natural selection, aside from rare exceptions due to founder effects and balancing selection (*14-16*).

An emerging strategy for solving clinical variant interpretation on a genome-wide scale is the use of information from closely related primate species to infer the pathogenicity of orthologous human variants (*17*). Because chimpanzees and humans share 99.4% protein sequence identity (*18*), a protein-altering variant present in one species can be expected to produce similar effects on the protein in the other species. By conducting population sequencing studies in closely related non-human primate species, it is feasible to systematically catalog common variants and rule these out as pathogenic in human, analogous to how sequencing more diverse human populations has helped to advance clinical variant interpretation (*8, 17*). Nonetheless, earlier work (*17*) was limited by the very small primate population sequencing datasets available, which bounded the number of common variants discovered, and the scale of machine learning classifiers that could be trained.

RESULTS

A database of 4.3 million benign missense variants across the primate lineage

To expand upon this strategy, we sequenced 703 individuals from 211 primate species (*19*), and aggregated these with data from previous studies (*19-26*), yielding a total of 809 individuals from 233 species. We identified 4.3 million unique missense (protein-altering) variants and 6.7 million unique synonymous (non-protein altering) variants (Fig. 1A), after excluding variants at positions that lacked unambiguous 1:1 mapping with human, or which resulted in non-concordant amino acid translation outcomes because of changes at neighboring nucleotides (fig. S1). The species selected for sequencing represent close to half of the 521 extant primate species on Earth (*27*) and cover all major primate families, from Old World monkeys and New World monkeys to lemurs and tarsiers. We targeted a small number of individuals per species (3.5 on average) to ensure that we primarily sampled common variants that have been filtered by natural selection rather than rare mutations (fig. S2).

Compared to the genome Aggregation Database (gnomAD) cohort of 141,456 human individuals from diverse populations (*28, 29*), the primate sequencing cohort contained ~20% more exome variants despite sequencing 1/175th the number of individuals (Fig. 1A and fig. S3), attesting to the remarkable genetic diversity present in non-human primate species (*19, 30*), many of which are critically endangered (*31*). The overlap of primate variants with gnomAD was low, consistent with independent mutational origins in each species (fig. S3). Out of the 22 million possible synonymous variants in the human genome, 30% were observed in the primate cohort, compared to just 6% of possible missense mutations (Fig. 1B). Because de novo mutations would have laid down unbiased proportions of missense and synonymous variants, the observed depletion of missense mutations in the primate cohort is consistent with the majority of newly-arising human missense mutations being removed by natural selection due to their deleteriousness (*8, 32-34*). The surviving missense variants are seen at high frequencies in primate populations, and represent a subset of missense variants that have tolerated filtering by natural selection and are unlikely to be pathogenic (*35*).

Missense variants from the primate cohort are strongly enriched for benign consequence in the ClinVar clinical variant database (Fig. 1C). Amongst ClinVar variants with higher review levels (2-star and above, indicating consensus by multiple submitters) (*4*), missense variants found in at least one non-human primate species were Benign or Likely Benign ~99% of the time, compared to 63% for ClinVar missense variants in general, and 80% for missense variants seen in gnomAD (Fig. 1C). The high fraction of pathogenic variants in gnomAD is consistent with the majority of these variants having arisen recently. Indeed, recent exponential human population growth introduced large numbers of rare variants through random de novo mutations (95% of variants in the gnomAD cohort are at < 0.01% population allele frequency), without sufficient time for selection to purge deleterious variants from the population (*36-40*). Consequently, the gnomAD cohort provides a comparatively unfiltered look at variation caused by random mutations, whereas primate common variants represent the subset of random mutations that have survived.

The regions of human disease genes that were most densely populated by ClinVar pathogenic variants were also strongly depleted for primate common variants, with examples shown for *CACNA1A* (Fig. 1D) and *CREBBP* (fig. S4), genes responsible for familial epilepsy (*41, 42*) and Rubinstein-Taybi syndrome (*43, 44*). Missense variants in the gnomAD cohort were partially depleted within these same critical regions (Fig. 1D and fig. S4), indicating that humans and primates experience similar selective pressures. However, deleterious variants were incompletely removed in humans, consistent with the shorter amount of time they were exposed to natural selection.

Prior to using primate data as an indicator of benign consequence in a diagnostic setting, it is vital to understand why a handful of human pathogenic ClinVar variants appear as tolerated common variants in primates. Our clinical laboratory independently reviewed evidence for each of the 36 ClinVar pathogenic variants that appeared in the primate cohort, according to ACMG guidelines (*14*). Among these 36 variants, 8 were reclassified as variants of uncertain significance based on insufficient evidence of pathogenicity in the literature and an additional 9 were hypomorphic or mild clinical variants (table S1). The remaining 19 variants appear to be truly pathogenic in human, and are presumably tolerated in primate because of primate-human differences, such as interactions with changes in the neighboring sequence context (*45, 46*). In one such example, a compensatory synonymous sequence change at an adjacent nucleotide explains why the variant is benign in primate, but creates a pathogenic splice defect in human (Fig. 1E). We also expect that some of the variants identified among primates are rare pathogenic variants by chance, despite the small number of individuals sequenced within each species. By expanding our cohort to sequence a large number of individuals per species, we would definitively exclude rare variation from our catalogue of primate variation, as well as grow the database of benign variants to improve clinical variant interpretation.

As evolutionary distance from human increases, cases where the surrounding sequence context has changed sufficiently to alter the effect of the variant should also increase, until common variants in more distant species could no longer be reliably counted on as benign in human. We examined variation in each major branch of the primate tree, as well as variation from mammals (mouse, rat, cow, dog), chicken, and zebrafish, and evaluated their pathogenicity in ClinVar (Fig. 1F). Common variants from species throughout the primate lineage, including more distant branches such as lemurs and tarsiers, varied from 98.6% to 99% benign in the human ClinVar database, but this dropped to 87% for placental mammals, and 71% for chicken. The high fraction of variants that are pathogenic in human, yet tolerated as common variants in more distant vertebrates, indicates that selection on orthologous variants diverges substantially in distantly-related species, as a consequence of changes in the surrounding sequence context and other differences in the species' biology (fig. S5).

We have made the primate population variant database, which contains over 4.3 million likely benign missense variants, publicly available at https://primad.basespace.illumina.com as a reference for the genomics community. Overall, this resource is over 50 times larger than ClinVar in terms of number of annotated missense variants, and consists almost entirely of variants of previously unknown significance. Most primate variants are rare or absent in the human population, with 98% of these variants at allele frequency < 0.01% (fig. S6). This makes it challenging to establish their pathogenicity through other means, since even the largest sequencing laboratories would be unlikely to observe any given variant in more than one unrelated patient. Despite their rarity, the subset of human variants that appear in primates have a low missense : synonymous ratio consistent with being depleted of deleterious missense variants (Fig. 1G). This contrasts with the high missense : synonymous ratio for rare human variants in the overall gnomAD cohort, which approaches the 2.2:1 ratio expected for random de novo mutations in the absence of selective constraint (*47*). At higher allele frequencies, natural selection has had more time to purge deleterious missense variants, allowing the human missense : synonymous ratio to start to converge toward the ratio observed for the subset of human variants that are present in other primates.

Gene-level selective constraint in humans versus non-human primates

The primate variant resource makes it possible to compare natural selection acting on individual genes across the primate lineage and identify human-specific evolutionary differences. Since the current primate cohort only contains an average of 3-4 individuals per species, we focused on comparing selective constraint in human genes versus primates as a whole. We found that the missense : synonymous ratios of individual genes were well-correlated between human and primates (Spearman r = 0.637) (Fig. 2A), indicating that genes which were depleted for deleterious missense mutations in human were also consistently depleted throughout the primate lineage. Moreover, the missense : synonymous ratios of both human and primate genes correlated similarly well with the probability of genes being loss of function intolerant (pLI) (Spearman correlation -0.534 and -0.489, respectively) (*28*). Had there been substantial divergence between human and primate, pLI, an independent metric derived from human protein-truncating variation, would have been expected to show much clearer agreement with human missense : synonymous ratios than primate.

To measure the selective constraint on each gene, we calculated the observed versus expected number of variants per gene, using trinucleotide mutation rates to model the expected probability of observing each variant (fig. S7) (*28, 29*). We modeled each primate species separately to account for differences in genetic diversity and the number of individuals sampled per species. The expected and observed counts of synonymous variants were highly correlated in both the gnomAD and primate cohorts, indicating that our model accurately captured the background distribution of neutral mutations (Fig. 2B; Spearman correlation 0.933 and 0.949, respectively). In contrast, for missense variants the expected and observed counts per gene diverged substantially (Spearman correlation 0.896 and 0.561 for human and primate, respectively), due to depletion of deleterious missense variants by natural selection in highly constrained genes (for example, high pLI genes). The most highly constrained genes were almost completely scrubbed of common missense variants in the primate cohort, whereas rare missense variants in the gnomAD cohort were depleted to a more modest extent due to the large sample size of gnomAD (Fig. 2C).

We next aimed to identify genes whose selective constraint was different in human compared to the rest of the primate lineage, a task made difficult by differences in diversity, allele frequency, and sample size between the human and primate cohorts (*34, 48, 49*). To this end, we developed two orthogonal strategies, and took the intersection of genes identified under both approaches. First, we used population genetic modeling (*34, 50, 51*) to estimate the average selection coefficient, s, ranging from 0 (benign) to 1 (severely pathogenic), of missense mutations in each gene, using a model of recent human population growth (figs. S7 and S8). We fit a single value of s per gene across non-human primate species, and identified genes that differed between $s_{primate}$ and s_{human} using a likelihood ratio test, which we validated using population simulations (fig. S9). In a second approach, we fit a curve approximating the relationship between human and primate missense : synonymous ratios using a Poisson generalized linear mixed model (*52*), and identified genes where the observed human missense : synonymous ratio deviated from what would have been expected given the gene's missense : synonymous ratio in primates (fig. S10). We also adjusted for gene length to account for shorter genes having more variability in their missense : synonymous ratio measurements than longer genes. The two methods were broadly concordant, with a Spearman correlation of 0.80 between the genes' effect sizes in the two tests. Estimates of selection coefficients and observed and expected counts for each gene in human and primate are provided in table S2.

In total, we found 39 genes where selective constraint differed significantly between human and other primates under both methods (Benjamini-Hochberg FDR < 0.05 (*53*); Fig. 2D). The top three genes where s_{human} decreased the most relative to $s_{primate}$ were *CFTR*, *GJB2*, and *CD36*, autosomal recessive disease genes for cystic fibrosis (*54*), hereditary deafness (*55*), and platelet glycoprotein deficiency (*56*), respectively. All three genes are known for deleterious mutations that are unusually common in local geographic human populations (*57-60*), suggesting that they may be experiencing reduced selection due to heterozygote advantage that protects against specific environmental pathogens (*60-64*). On the other end of the spectrum, *TERT*, known for its role in maintaining telomere length (*65, 66*), was among the top genes where s_{human} increased the most relative to $s_{primate}$. Humans have adapted to a much longer lifespan compared with other primate species, which have a median lifespan of 20-30 years, suggesting that increased selection on *TERT* may have occurred as part of human adaption towards extended longevity. We note that with the current size of the primate cohort, it is not possible to distinguish whether the increased selection on *TERT* occurred only in humans, or if it is part of a gradual trend towards extended longevity that began earlier in the great ape lineage, which also have longer lifespans relative to other primates (~40 years). Expanding the primate cohort by sequencing more individuals per species would improve detection of additional species-specific and lineage-specific evolutionary adaptation, and shed light on the evolutionary path that led to the present human condition.

PrimateAI-3D, a deep learning network for classifying protein-altering variants

We constructed PrimateAI-3D, a semi-supervised 3D-convolutional neural network for variant pathogenicity prediction, which we trained using 4.5 million common missense variants with likely benign consequence (Fig. 3A). In a departure from prior deep learning architectures that operated on linear sequence (*17, 67*), we voxelized the 3D structure of the protein at 2 Angstrom resolution (figs. S11 and S12) and used 3D-convolutions to enable the network to recognize key structural regions that may not be apparent from sequence alone (Fig. 3A). As an example, we show PrimateAI-3D predictions for *STK11* (Fig. 3B), the tumor suppressor gene responsible for Peutz-Jeghers hereditary polyposis syndrome (*68-71*), with each amino acid position colored by the average PrimateAI-3D score at that position. Common primate variants used for training and annotated ClinVar pathogenic variants from separate parts of the linear sequence form distinct clusters in 3D space. Although ClinVar variants are shown for illustration, it is important to note that the network was not trained on either human-engineered features or annotated variants from clinical variant databases, thereby avoiding potential human biases in variant annotation. Rather, it learns to infer pathogenicity based on the local enrichment or depletion of common primate variants, taking only the protein's multiple sequence alignment and 3D structure as inputs.

PrimateAI-3D can utilize protein structures from either experimental sources or computational prediction (*72-76*); we used AlphaFold DB (*72, 73*) and HHpred (*74*) predicted structures for the broadest coverage across human genes. For training data, we incorporated all common missense variants from the 233 non-human primate species (*17*), and common human missense variants (allele frequency > 0.1% across populations) in gnomAD (*28, 29*), TOPMed (*77, 78*), and UK Biobank (*79, 80*), resulting in a total of 4.5 million unique missense variants of likely benign consequence. This dataset covers 6.34% of all possible human missense variants, and is over 50-fold larger than the current ClinVar database (79,381 missense variants after excluding variants of uncertain significance and those with conflicting annotations), greatly enlarging the training dataset available for machine learning approaches. Because the training dataset consists only of variants labeled as benign, we created a control set of randomly selected variants that were matched to the common variants by trinucleotide mutation rate, and trained PrimateAI-3D to separate common variants from matched controls as a semi-supervised learning task.

In parallel with the variant classification task, we generated amino acid substitution probabilities for each position in the protein by masking the residue and using the sequence context to predict the missing amino acid, borrowing from language model architectures that are trained to predict missing words in sentences (*81, 82*). We trained both a 3D convolutional "fill-in-the-blank" model, which tasked the network with predicting the missing amino acid in a gap in the voxelized 3D protein structure, and separately, a language model utilizing the transformer architecture to predict the missing amino acid using the surrounding multiple sequence alignment as context (*83*). We implemented these models as additional loss functions to further refine the PrimateAI-3D predictions (fig. S13). We also trained a variational autoencoder (*67*) on multiple sequence alignments and found that it performed comparably to our transformer architecture (fig. S14). Hence, we incorporated the average of their predictions in the loss function, which performed better than either alone.

We evaluated PrimateAI-3D and 15 other published machine learning methods (*67, 84*) on their ability to distinguish between benign and pathogenic variants along six different axes (Fig. 3C, 3D, and fig. S15): predicting the effects of rare missense variants on quantitative clinical phenotypes in a cohort of 200,643 individuals from the UK Biobank (UKBB); distinguishing de novo missense mutations (DNM) seen in 31,058 patients with neurodevelopmental disorders (*85-87*) (DDD) from de novo missense mutations in 2,555 healthy controls (*88-93*); distinguishing de novo missense mutations seen in 4,295 patients with autism spectrum disorders (*88-94*) (ASD) from de novo missense mutations in the shared set of 2,555 healthy controls; distinguishing de novo missense mutations seen in 2,871 patients with congenital heart disease (*95*) (CHD) from de novo missense mutations in the shared set of 2,555 healthy controls; separating annotated ClinVar benign and pathogenic variants (ClinVar) (*4*); and average correlation with in vitro deep mutational scan experimental assays across 9 genes (*96-105*) (DMS assays). Our set of clinical benchmarks is the most comprehensive to date, and has a particular focus on rigorously testing the performance of classifiers on large patient cohorts across a diverse range of real world clinical settings (table S3).

For the UK Biobank benchmark, we analyzed 200,643 individuals with both exome sequencing data and broad clinical phenotyping, and identified 42 genes where the presence of rare missense variants was associated with changes in a quantitative clinical phenotype controlling for confounders such as population stratification, age, sex, and medications (table S4). These gene-phenotype associations included diverse clinical lab measurements such as low-density lipoprotein (LDL) cholesterol (increased by rare missense variants in *LDLR*, decreased by variants in *PCSK9*), blood glucose (increased by variants in *GCK*), and platelet count (increased by variants in *JAK2*, decreased by variants in *GP1BB*), as well as other quantitative phenotypes such as standing height (increased by variants in *ZFAT*) (table S4). To test each classifier's ability to distinguish between pathogenic and benign missense variants, we measured the correlation between pathogenicity prediction score and quantitative phenotype for patients carrying rare missense variants in each of these genes. We report the average correlation across all gene-phenotype pairs for each classifier, taking the absolute value of the correlation, since these genes may be associated with either increase or decrease in the quantitative clinical phenotype.

The neurodevelopmental disorders cohort (DDD), autism spectrum disorders cohort (ASD), and congenital heart disease cohort (CHD) are among the largest published trio-sequencing studies to date, and consist of thousands of families with a child with rare genetic disease and their unaffected parents. In each cohort, we cataloged de novo missense mutations that appeared in affected probands but were absent in their parents, as well as de novo missense mutations that appeared in a set of shared healthy controls. We evaluated the ability of each classifier to separate the de novo missense mutations that appear in cases versus controls on the basis of their prediction scores, using the Mann-Whitney U test to measure performance.

PrimateAI-3D outperformed all other classifiers at distinguishing pathogenic from benign variants in the four patient cohorts we tested (UKBB, DDD, ASD, CHD); it was also the top performer at separating pathogenic from benign variants in the ClinVar annotation database, and had the highest average correlation with the deep mutational scan assays (Fig. 3D and fig. S15). After PrimateAI-3D, there was no clear runner-up, with second place occupied by six different classifiers in the six different benchmarks. We observed a moderate correlation between the performance of different classifiers in UKBB and DDD (Spearman r = 0.556; Fig. 3C), which are the two largest clinical cohorts and therefore likely the most robust for benchmarking (with 200,643 and 33,613 patients, respectively), but outside of PrimateAI-3D, strong performance of a classifier on one task had limited generalizability to other tasks. Our results underscore the importance of validating machine learning classifiers along multiple dimensions, particularly in large real-world cohorts, to avoid overgeneralizing a classifier's performance based upon an impressive showing along a single axis.

PrimateAI-3D's top-ranked performance at separating benign and pathogenic missense variants in ClinVar was unexpected, since the other machine learning classifiers (with the exception of EVE) were trained either directly on ClinVar, or on other variant annotation databases with a high degree of content overlap. Because they are primarily based on variants described in the literature, clinical variant databases are subject to ascertainment bias (*12, 106, 107*), which may have contributed to supervised classifiers picking up on tendencies of human variant annotation that are unrelated to the task of separating benign from pathogenic variants (figs. S16, S17, and S18). Given the challenges with human annotation, we also investigated whether PrimateAI-3D could assist in revising incorrectly labeled ClinVar variants, by comparing annotations in the current ClinVar database and those from a September 2017 snapshot. Disagreement between PrimateAI-3D and the 2017 version of ClinVar was highly predictive of future revision and the odds of revision increased with PrimateAI-3D confidence (fig. S19). Among variants with the 10% most confident PrimateAI-3D predictions, the odds of revision were 10-fold elevated if PrimateAI-3D was in disagreement with the ClinVar label ($P < 10^{-14}$).

The performance of PrimateAI-3D on clinical variant benchmarks scaled directly with training dataset size, indicating that additional primate sequencing data will be the key to unlocking further gains (Fig. 4 and fig. S20). The current primate cohort already covers 30% of all possible synonymous variants in the human genome, despite containing only 809 individuals from 233 species (Fig. 4B). By increasing the number of species and the number of individuals sequenced per species, we expect to saturate the majority of the remaining tolerated substitutions in the human genome (fig. S21), including both coding and noncoding variation, leaving the remaining deleterious variants to be deduced by process of elimination.

Discovery of candidate disease genes for neurodevelopmental disorders

We applied PrimateAI-3D to improve statistical power for discovering candidate disease genes that are enriched for pathogenic de novo mutations in the neurodevelopmental disorders cohort (fig. S22). De novo missense mutations from affected individuals in the DDD cohort (*87*) were enriched 1.36-fold above expectation, based on estimates of background mutation rate using trinucleotide context (*47*). We selected a PrimateAI-3D classification threshold of 0.821, which called an equal number of pathogenic missense mutations (n=7,238) as the excess of de novo missense mutations in the cohort (Fig. 5A). Stratifying missense mutations by this threshold increased enrichment of pathogenic de novo missense mutations to 2.0-fold, substantially increasing statistical power for disease gene discovery in the cohort (Fig. 5B).

By applying PrimateAI-3D to prioritize pathogenic missense variants, we identified 290 genes associated with intellectual disability at genome-wide significance ($P < 6.4 \times 10^{-7}$) (Table 1), of which 272 were previously discovered genes that either appeared in the Genomics England intellectual disability gene panel (*108*), or were already identified in the prior study (*109*) without stratifying missense variants (table S5). We excluded two genes, *BMPR2* and *RYR1* as borderline significant genes that already had well-annotated non-neurological phenotypes. Further clinical studies are needed to independently validate this list of candidate genes and understand their range of phenotypic effects.

Discussion

Our results demonstrate the successful pairing of primate population sequencing with state-of-the-art deep learning models to make meaningful progress towards solving variants of uncertain significance. Primate population sequencing and large-scale human sequencing are likely to fill complementary roles in advancing clinical understanding of human genetic variants. From the perspective of acquiring additional benign variants to train PrimateAI-3D, humans are not suitable, as the discovery of common human variants (>0.1% allele frequency) plateaus at roughly ~100,000 missense variants after only a few hundred individuals (*17*), and further population sequencing into the millions mainly contributes rare variants which cannot be ruled out for deleterious consequence. On the other hand, these rare human variants, because they have not been thoroughly filtered by natural selection, preserve the potential to exert highly penetrant phenotypic effects, making them indispensable for discovering new gene-phenotype relationships in large population sequencing and biobank studies. Fittingly, classifiers trained on common primate variants may accelerate these target discovery efforts, by helping to differentiate between benign and pathogenic rare variation.

The genetic diversity found in the 520 known non-human primate species is the result of ongoing natural experiments on genetic variation that have been running uninterrupted for millions of years. Today, over 60% of primate species on Earth are threatened with extinction in the next decade due to man-made factors (*31*). We must decide whether to act now to preserve these irreplaceable species, which act as a mirror for understanding our genomes and ourselves, and are each valuable in their own right, or bear witness to the conclusion of many of these experiments.

Materials and Methods

Primate polymorphism data

We aggregated high-coverage whole genomes of 809 primate individuals across 233 primate species, including 703 newly sequenced samples and 106 previously sequenced samples from the Great Ape Genome project (*19*). Samples that passed quality evaluation were then aligned to 32 high-quality primate reference genomes (*110*) and mapped to the GRCh38 human genome build.

We developed a random forest (RF) classifier to identify false positive variant calls and errors resulting from ambiguity in the species mapping. In addition, we removed variants that fell in primate codons that did not match the human codon at that position, as well as those residing in primate transcripts with likely annotation errors. We also devised quality metrics based on the distribution of RF scores and Hardy-Weinberg equilibrium, and developed a unique mapping filter to exclude variants in regions of non-unique mapping between primate species.

Identifying differential selection between humans and primates via population modeling

We first established a neutral background distribution of mutation rates per gene for each primate species by fitting the Poisson Random Field (PRF) model to the segregating synonymous variants in each species. The observed number of segregating synonymous sites is a Poisson random variable, with the mean determined by mutation rate, demography, and sample size (*34*). For simplicity, we assumed an equilibrium (i.e. constant) demography for all species besides human; for human, we used Moments (*51*) to find a best fitting demographic history based on the folded site frequency spectrum of synonymous sites. We adopted a Gamma distributed prior on mutation rates, which also accounts for the impact of GC content on mutation rate. We optimized the prior parameters via maximum likelihood and computed the posterior distribution of the mutation rate per gene.

The number of segregating nonsynonymous sites is modeled as a Poisson random variable similar to synonymous sites with additional selection parameters. We assumed that every nonsynonymous mutation in a gene shares the same population scaled selection coefficient γ_{ig}. To explicitly estimate selection coefficient of each gene per species, we devised a two-step procedure analogous to an EM algorithm to control for differences in population size across species.

To identify genes where human constraint is different from non-human primate selection, we developed a likelihood ratio test to test whether population scaled selection coefficients are significantly different between human and other primates. We then assessed whether our population genetic modeling improved the correlation of selection estimates of our primate data with previous gene-constraint metrics in humans, including pLI (*28*) and s_het (*111*). To validate the performance of our model, we performed population genetic simulations.

Poisson generalized linear mixed modeling of selection between humans and primates

In addition to population genetics model described above, we also applied an orthogonal approach to detect differences in selection between humans and primates based on missense-to-synonymous ratio (MSR). We fit a Poisson generalized linear mixed model (GLMM) to the pooled polymorphic synonymous and missense mutations across all primates to estimate the depletion of missense variants in each gene. Then, we fit a second Poisson GLMM to the human data, controlling for the primate depletion estimates, and compared the pooled primate MSR to the human MSR for each gene.

PrimateAI-3D Model

PrimateAI-3D is a 3D convolutional neural network that uses protein structures and multiple sequence alignments (MSA) to predict the pathogenicity of human missense variants. To generate the input for a 3D convolutional neural network, we voxelized the protein structure and evolutionary conservation in the region surrounding the missense variant. The network was trained to optimize three objectives: distinction between benign and unknown human variants; prediction of a masked amino acid at the variant site; per-gene variant ranks based on protein language models.

Protein structures and multiple sequence alignments

For 341 species, we used vertebrate and mammal MSAs from UCSC Multiz100 (*112, 113*) and Zoonomia (*114*). Another 251 species appeared in Uniprot for least 75% of all human proteins (*115*). For each protein, alignments from all 341+251=592 species were merged. Human protein structures were taken from AlphaFold DB (June 2021) (*73*). Proteins that did not sequence-match exactly to our hg38 proteins (2590; 13.5%) were homology modeled using HHpred (*74*) and Modeller (*116*).

Protein voxelization and voxel features

A regular sized 3D grid of 7x7x7 voxels, each spanning 2Åx2Åx2Å, was centered at the Cα atom of the residue containing the target variant (Fig. S11). For each voxel, we provided a vector of distances between its center and the nearest Cα and Cβ atoms of each amino acid type (Fig. S11; details in Supplementary Text section 1). We also provided additional voxel features including the pLDDT confidence metric from AlphaFold DB (Fig. S12), and the evolutionary profile, consisting of each amino acid's frequency at the corresponding position in the 592 species alignment.

Model architecture

The first layers of the PrimateAI-3D model reduce the voxel tensor to a 64-vector through repeated valid-padded 3D convolutions with a kernel size of 3x3x3. A final hidden dense layer transforms this 64-length vector into a 20-length vector, corresponding to one output unit per amino acid at that position. The model was trained simultaneously using multiple loss functions to optimize the following complementary aspects of pathogenicity:

Benign primate variants

Using 4.5 million benign missense variants from primates, we sampled the same number of unknown variants from the set of all possible human missense variants, with the distribution of mutational probabilities matching the benign set, based on a trinucleotide mutation rate model. Variants for the same protein position were combined in a 20-length vector (benign: 0, unknown: 1) which was the target label for the network. We used mean squared error (MSE) as the loss function for non-missing labels and ignored missing labels.

3D fill-in-the-blank

We removed all atoms of a target residue before voxelization, discarding any information about the residue from the input tensor to the network. The network was then trained to predict a 20-

length vector, labeled 0 (benign) for amino acids that occur at the target site in any of the 592 species and 1 (pathogenic) otherwise. All human protein positions with at least one possible missense variant were included in this dataset.

Variant ranks from language models

For each gene, we took the average pathogenicity ranking from two protein language models, PrimateAI LM, a MSA transformer (described below) and our reimplementation of the EVE variational autoencoder algorithm which we extended to all human proteins (EVE*) (*67*). We calculated the pairwise logistic rank loss as described in Pasumarthi *et al.*(*117*).

PrimateAI Language Model

The PrimateAI language model (PrimateAI LM) is a MSA transformer (*83*) for fill-in-the-blank residue classification, which is trained end-to-end on MSAs of UniRef-50 proteins (*118, 119*) to minimize an unsupervised masked language modelling (MLM) objective (*81*). Our model requires ~50x less computation for training than previous MSA transformers due to several improvements in architecture and training (Fig. S9).

Model training procedure

Each batch had the same number of samples from each of the three variant datasets (~33 with a batch size of 100). For the language model ranks dataset, all 33 samples had to come from the same protein. The number of times a protein was chosen for a batch was proportional to the length of the protein. In order to make our model robust against protein orientations, we randomly rotated the protein atomic coordinates in 3D before voxelizing a variant.

Model Evaluation

We compared performance of our model and other models (*84*) on variants for which all models had scores. Deep mutational scanning assays were available for 9 human genes: Amyloid-beta (*102*), *YAP1* (*96*), *MSH2* (*120*), *SYUA* (*101*), *VKOR1* (*121*), *PTEN* (*99, 100*), *BRCA1* (*122*), *TP53* (*123*), and *ADRB2* (*124*). For each assay and prediction model, we calculated the absolute Spearman rank correlation between prediction and assay scores. The UK Biobank dataset (*79, 80*) contains 42 gene-phenotype pairs which were significantly associated by rare variant burden testing using all rare missense variants, without applying missense pathogenicity prioritization. The evaluation was the same as with DMS assays, except that correlations were calculated from the quantitative phenotypes of individuals carrying the variant, instead of the assay score for the variant. For ClinVar (*4*), we filtered to high-quality 2-star variants and evaluated model performance by calculating per-gene area under the receiver operating characteristic curve (AUC). For the rare disease cohorts, we collected de novo missense mutations from patients with developmental disorders (*85-87*), autism spectrum disorders (*88-94*) or congenital heart disorders (*95*). For all three datasets, we compared against DNM variants from healthy controls (*88-93*). We applied the Mann-Whitney U test to measure how well each model's prediction scores could distinguish patient variants from control variants.

References and Notes:

1. D. G. MacArthur *et al.*, Guidelines for investigating causality of sequence variants in human disease. *Nature* **508**, 469-476 (2014).

2. R. L. Nussbaum, H. L. Rehm, ClinGen, ClinGen and Genetic Testing. *N Engl J Med* **373**, 1379 (2015).
3. H. L. Rehm *et al.*, ClinGen--the Clinical Genome Resource. *N Engl J Med* **372**, 2235-2242 (2015).
4. M. J. Landrum *et al.*, ClinVar: public archive of interpretations of clinically relevant variants. *Nucleic Acids Res* **44**, D862-868 (2016).
5. X. Liu, C. Wu, C. Li, E. Boerwinkle, dbNSFP v3.0: A One-Stop Database of Functional Predictions and Annotations for Human Nonsynonymous and Splice-Site SNVs. *Hum Mutat* **37**, 235-241 (2016).
6. P. D. Stenson *et al.*, The Human Gene Mutation Database: building a comprehensive mutation repository for clinical and molecular genetics, diagnostic testing and personalized genomic medicine. *Hum Genet* **133**, 1-9 (2014).
7. H. L. Rehm, Evolving health care through personal genomics. . *Nat Rev Genet* **18**, 259-267 (2017).
8. N. Whiffin *et al.*, Using high-resolution variant frequencies to empower clinical genome interpretation. *Genet Med* **19**, 1151-1158 (2017).
9. S. Caspar *et al.*, Clinical sequencing: from raw data to diagnosis with lifetime value. *Clinical genetics* **93**, 508-519 (2018).
10. Y. Yang *et al.*, Molecular findings among patients referred for clinical whole-exome sequencing. *Jama* **312**, 1870-1879 (2014).
11. J. A. SoRelle, D. M. Thodeson, S. Arnold, G. Gotway, J. Y. Park, Clinical Utility of Reinterpreting Previously Reported Genomic Epilepsy Test Results for Pediatric Patients. *JAMA Pediatr* **173**, e182302 (2019).
12. N. Shah *et al.*, Identification of Misclassified ClinVar Variants via Disease Population Prevalence. *Am J Hum Genet* **102**, 609-619 (2018).
13. O. Campuzano *et al.*, Reanalysis and reclassification of rare genetic variants associated with inherited arrhythmogenic syndromes. *EBioMedicine* **54**, 102732 (2020).
14. S. Richards *et al.*, Standards and guidelines for the interpretation of sequence variants: a joint consensus recommendation of the American College of Medical Genetics and Genomics and the Association for Molecular Pathology. *Genet Med* **17**, 405-424 (2015).
15. Y. E. Kim, C. S. Ki, M. A. Jang, Challenges and Considerations in Sequence Variant Interpretation for Mendelian Disorders. *Ann Lab Med* **39**, 421-429 (2019).
16. M. Slatkin, A population-genetic test of founder effects and implications for Ashkenazi Jewish diseases. *The American Journal of Human Genetics* **75**, 282-293 (2004).
17. L. Sundaram *et al.*, Predicting the clinical impact of human mutation with deep neural networks. *Nat Genet* **50**, 1161-1170 (2018).
18. C. S. A. Consortium, Initial sequence of the chimpanzee genome and comparison with the human genome. *Nature* **437**, 69-87 (2005).
19. J. Prado-Martinez *et al.*, Great ape genome diversity and population history. *Nature* **499**, 471-475 (2013).
20. Z. Fan *et al.*, Ancient hybridization and admixture in macaques (genus Macaca) inferred from whole genome sequences. *Mol Phylogenet Evol* **127**, 376-386 (2018).
21. Z. Liu *et al.*, Genomic Mechanisms of Physiological and Morphological Adaptations of Limestone Langurs to Karst Habitats. *Mol Biol Evol* **37**, 952-968 (2020).
22. L. Wang *et al.*, A high-quality genome assembly for the endangered golden snub-nosed monkey (Rhinopithecus roxellana). *Gigascience* **8**, (2019).
23. C. Zoonomia, A comparative genomics multitool for scientific discovery and conservation. *Nature* **587**, 240-245 (2020).

24. B. J. Evans *et al.*, Speciation over the edge: gene flow among non-human primate species across a formidable biogeographic barrier. *R Soc Open Sci.* **4**, 170351 (2017).
25. L. Yu *et al.*, Genomic analysis of snub-nosed monkeys (Rhinopithecus) identifies genes and processes related to high-altitude adaptation. *Nat Genet* **48**, 947-952 (2016).
26. N. Osada, K. Matsudaira, Y. Hamada, S. Malaivijitnond, Testing sex-biased admixture origin of macaque species using autosomal and X-chromosomal genomic sequences. *Genome Biol. Evol.* **13**, (2021).
27. A. B. Rylands, R. A. Mittermeier, *Primate Behavioral Ecology*. (Routledge, New York, ed. 6, 2021), pp. 407–428.
28. M. Lek *et al.*, Analysis of protein-coding genetic variation in 60,706 humans. *Nature* **536**, 285-291 (2016).
29. K. J. Karczewski *et al.*, The mutational constraint spectrum quantified from variation in 141,456 humans. *Nature* **581**, 434-443 (2020).
30. E. M. Leffler *et al.*, Revisiting an old riddle: what determines genetic diversity levels within species? *PLoS Biol* **10**, e1001388 (2012).
31. A. Estrada *et al.*, Impending extinction crisis of the world's primates: Why primates matter. *Sci Adv* **3**, e1600946 (2017).
32. T. Ohta, Slightly deleterious mutant substitutions in evolution. *Nature* **246**, 96-98 (1973).
33. D. E. Reich, E. S. Lander, On the allelic spectrum of human disease. *Trends Genet* **17**, 502-510 (2001).
34. S. A. Sawyer, D. L. Hartl, Population genetics of polymorphism and divergence. *Genetics* **132**, 1161-1176 (1992).
35. A. Eyre-Walker, P. D. Keightley, The distribution of fitness effects of new mutations. *Nature Reviews Genetics* **8**, 610-618 (2007).
36. W. Fu *et al.*, Analysis of 6,515 exomes reveals the recent origin of most human protein-coding variants. *Nature* **493**, 216-220 (2013).
37. Y. B. Simons, M. C. Turchin, J. K. Pritchard, G. Sella, The deleterious mutation load is insensitive to recent population history. *Nature genetics* **46**, 220-224 (2014).
38. R. Do *et al.*, No evidence that selection has been less effective at removing deleterious mutations in Europeans than in Africans. *Nature Genetics* **47**, 126-131 (2015).
39. P. K. Albers, G. McVean, Dating genomic variants and shared ancestry in population-scale sequencing data. *PLoS biology* **18**, e3000586 (2020).
40. I. Mathieson, G. McVean, Demography and the age of rare variants. *PLoS Genet* **10**, e1004528 (2014).
41. L. Damaj *et al.*, CACNA1A haploinsufficiency causes cognitive impairment, autism and epileptic encephalopathy with mild cerebellar symptoms. *Eur J Hum Genet* **23**, 1505-1512 (2015).
42. K. Reinson *et al.*, Biallelic CACNA1A mutations cause early onset epileptic encephalopathy with progressive cerebral, cerebellar, and optic nerve atrophy. *Am J Med Genet A* **170**, 2173-2176 (2016).
43. A. Bentivegna *et al.*, Rubinstein-Taybi Syndrome: spectrum of CREBBP mutations in Italian patients. *BMC Med Genet* **7**, 77 (2006).
44. M. Stef *et al.*, Spectrum of CREBBP gene dosage anomalies in Rubinstein-Taybi syndrome patients. *Eur J Hum Genet* **15**, 843-847 (2007).
45. A. S. Kondrashov, S. Sunyaev, F. A. Kondrashov, Dobzhansky-Muller incompatibilities in protein evolution. *Proc Natl Acad Sci U S A* **99**, 14878-14883 (2002).
46. D. M. Jordan *et al.*, Identification of cis-suppression of human disease mutations by comparative genomics. *Nature* **524**, 225-229 (2015).

47. K. E. Samocha *et al.*, A framework for the interpretation of de novo mutation in human disease. *Nat Genet* **46**, 944-950 (2014).
48. C. D. Bustamante, J. Wakeley, S. Sawyer, D. L. Hartl, Directional selection and the site-frequency spectrum. *Genetics* **159**, 1779-1788 (2001).
49. X. Huang *et al.*, Inferring genome-wide correlations of mutation fitness effects between populations. *Molecular Biology and Evolution*.
50. R. N. Gutenkunst, R. D. Hernandez, S. H. Williamson, C. D. Bustamante, Inferring the joint demographic history of multiple populations from multidimensional SNP frequency data. *PLoS Genet* **5**, e1000695 (2009).
51. J. Jouganous, W. Long, A. P. Ragsdale, S. Gravel, Inferring the Joint Demographic History of Multiple Populations: Beyond the Diffusion Approximation. *Genetics* **206**, 1549-1567 (2017).
52. D. Bates, M. Mächler, B. Bolker, S. Walker, Fitting Linear Mixed-Effects Models Using lme4. *Journal of Statistical Software,* **67**, 1-48 (2015).
53. Y. Benjamini, Y. Hochberg, Controlling the False Discovery Rate: A Practical and Powerful Approach to Multiple Testing. *Journal of the Royal Statistical Society. Series B* **57**, 289-300 (1995).
54. R. K. Rowntree, A. Harris, The phenotypic consequences of CFTR mutations. *Annals of human genetics* **67**, 471-485 (2003).
55. S. A. Wilcox *et al.*, High frequency hearing loss correlated with mutations in the GJB2 gene. *Human genetics* **106**, 399-405 (2000).
56. H. Shu *et al.*, The role of CD36 in cardiovascular disease. *Cardiovascular Research*, (2020).
57. J. L. Bobadilla, M. Macek Jr, J. P. Fine, P. M. Farrell, Cystic fibrosis: a worldwide analysis of CFTR mutations—correlation with incidence data and application to screening. *Human mutation* **19**, 575-606 (2002).
58. M. H. Chaleshtori *et al.*, High carrier frequency of the GJB2 mutation (35delG) in the north of Iran. *International journal of pediatric otorhinolaryngology* **71**, 863-867 (2007).
59. J. Liu *et al.*, Distribution of CD36 deficiency in different Chinese ethnic groups. *Human Immunology* **81**, 366-371 (2020).
60. T. J. Aitman *et al.*, Malaria susceptibility and CD36 mutation. *Nature* **405**, 1015-1016 (2000).
61. J. E. Common, W.-L. Di, D. Davies, D. P. Kelsell, Further evidence for heterozygote advantage of GJB2 deafness mutations: a link with cell survival. *Journal of medical genetics* **41**, 573-575 (2004).
62. P. D'Adamo *et al.*, Does epidermal thickening explain GJB2 high carrier frequency and heterozygote advantage? *European Journal of Human Genetics* **17**, 284-286 (2009).
63. S. A. Schroeder, D. M. Gaughan, M. Swift, Protection against bronchial asthma by CFTR ΔF508 mutation: a heterozygote advantage in cystic fibrosis. *Nature medicine* **1**, 703-705 (1995).
64. G. B. Pier *et al.*, Salmonella typhi uses CFTR to enter intestinal epithelial cells. *Nature* **393**, 79-82 (1998).
65. S. E. Bojesen *et al.*, Multiple independent variants at the TERT locus are associated with telomere length and risks of breast and ovarian cancer. *Nature genetics* **45**, 371-384 (2013).
66. B. Heidenreich, R. Kumar, TERT promoter mutations in telomere biology. *Mutation Research/Reviews in Mutation Research* **771**, 15-31 (2017).

67. J. Frazer *et al.*, Disease variant prediction with deep generative models of evolutionary data. *Nature* **599**, 91-95 (2021).
68. H. D. Chae, C. H. Jeon, Peutz-Jeghers syndrome with germline mutation of STK11. *Ann Surg Treat Res* **86**, 325-330 (2014).
69. I. Hernan *et al.*, De novo germline mutation in the serine-threonine kinase STK11/LKB1 gene associated with Peutz-Jeghers syndrome. *Clin Genet* **66**, 58-62 (2004).
70. C. Nakanishi *et al.*, Germline mutation of the LKB1/STK11 gene with loss of the normal allele in an aggressive breast cancer of Peutz-Jeghers syndrome. *Oncology* **67**, 476-479 (2004).
71. H. R. Yang, J. S. Ko, J. K. Seo, Germline mutation analysis of STK11 gene using direct sequencing and multiplex ligation-dependent probe amplification assay in Korean children with Peutz-Jeghers syndrome. *Dig Dis Sci* **55**, 3458-3465 (2010).
72. J. Jumper *et al.*, Highly accurate protein structure prediction with AlphaFold. *Nature* **596**, 583-589 (2021).
73. M. Varadi *et al.*, AlphaFold Protein Structure Database: massively expanding the structural coverage of protein-sequence space with high-accuracy models. *Nucleic Acids Research*, (2021).
74. J. Söding, A. Biegert, A. N. Lupas, The HHpred interactive server for protein homology detection and structure prediction. *Nucleic Acids Research* **33**, W244-W248 (2005).
75. M. Kallberg *et al.*, Template-based protein structure modeling using the RaptorX web server. *Nat Protoc* **7**, 1511-1522 (2012).
76. S. Wang, W. Li, S. Liu, J. Xu, RaptorX-Property: a web server for protein structure property prediction. *Nucleic Acids Res* **44**, W430-435 (2016).
77. D. J. Burgess, The TOPMed genomic resource for human health. *Nat Rev Genet* **22**, 200 (2021).
78. D. Taliun *et al.*, Sequencing of 53,831 diverse genomes from the NHLBI TOPMed Program. *Nature* **590**, 290-299 (2021).
79. C. Bycroft *et al.*, The UK Biobank resource with deep phenotyping and genomic data. *Nature* **562**, 203-209 (2018).
80. C. Sudlow *et al.*, UK biobank: an open access resource for identifying the causes of a wide range of complex diseases of middle and old age. *PLoS Med* **12**, e1001779 (2015).
81. J. Devlin, M.-W. Chang, K. Lee, K. Toutanova, BERT: Pre-training of Deep Bidirectional Transformers for Language Understanding. **1**, 4171-4186 (2019).
82. Y. You *et al.*, in *International Conference on Learning Representations*. (2020).
83. R. M. Rao *et al.*, MSA Transformer. *Proceedings of the 38th International Conference on Machine Learning* **139**, 8844–8856 (2021).
84. X. Liu, C. Li, C. Mou, Y. Dong, Y. Tu, dbNSFP v4: a comprehensive database of transcript-specific functional predictions and annotations for human nonsynonymous and splice-site SNVs. *Genome Medicine* **12**, 103 (2020).
85. Deciphering Developmental Disorders Study, Large-scale discovery of novel genetic causes of developmental disorders. *Nature* **519**, 223-228 (2015).
86. Deciphering Developmental Disorders Study, Prevalence and architecture of de novo mutations in developmental disorders. *Nature* **542**, 433-438 (2017).
87. J. Kaplanis *et al.*, Evidence for 28 genetic disorders discovered by combining healthcare and research data. *Nature* **586**, 757-762 (2020).
88. J. Y. An *et al.*, Genome-wide de novo risk score implicates promoter variation in autism spectrum disorder. *Science* **362**, (2018).

89. S. De Rubeis *et al.*, Synaptic, transcriptional and chromatin genes disrupted in autism. *Nature* **515**, 209-215 (2014).
90. I. Iossifov *et al.*, The contribution of de novo coding mutations to autism spectrum disorder. *Nature* **515**, 216-221 (2014).
91. I. Iossifov *et al.*, De novo gene disruptions in children on the autistic spectrum. *Neuron* **74**, 285-299 (2012).
92. S. J. Sanders *et al.*, Insights into Autism Spectrum Disorder Genomic Architecture and Biology from 71 Risk Loci. *Neuron* **87**, 1215-1233 (2015).
93. S. J. Sanders *et al.*, De novo mutations revealed by whole-exome sequencing are strongly associated with autism. *Nature* **485**, 237-241 (2012).
94. B. J. O'Roak *et al.*, Sporadic autism exomes reveal a highly interconnected protein network of de novo mutations. *Nature* **485**, 246-250 (2012).
95. S. C. Jin *et al.*, Contribution of rare inherited and de novo variants in 2,871 congenital heart disease probands. *Nat Genet* **49**, 1593-1601 (2017).
96. C. L. Araya *et al.*, A fundamental protein property, thermodynamic stability, revealed solely from large-scale measurements of protein function. *Proceedings of the National Academy of Sciences* **109**, 16858–16863 (2012).
97. M. A. Chiasson *et al.*, Multiplexed measurement of variant abundance and activity reveals VKOR topology, active site and human variant impact. *eLife* **9**, (2020).
98. X. Jia *et al.*, Massively parallel functional testing of MSH2 missense variants conferring Lynch syndrome risk. *American journal of human genetics* **108**, 163-175 (2021).
99. K. A. Matreyek *et al.*, Multiplex assessment of protein variant abundance by massively parallel sequencing. *Nature Genetics* **50**, 874-882 (2018).
100. T. L. Mighell, S. Evans-Dutson, B. J. O'Roak, A Saturation Mutagenesis Approach to Understanding PTEN Lipid Phosphatase Activity and Genotype-Phenotype Relationships. *American journal of human genetics* **102**, 943-955 (2018).
101. R. W. Newberry, J. T. Leong, E. D. Chow, M. Kampmann, W. F. DeGrado, Deep mutational scanning reveals the structural basis for α-synuclein activity. *Nature Chemical Biology* **16**, 653-659 (2020).
102. M. Seuma, A. J. Faure, M. Badia, B. Lehner, B. Bolognesi, The genetic landscape for amyloid beta fibril nucleation accurately discriminates familial Alzheimer’s disease mutations. *Elife* **10**, e63364 (2021).
103. A. O. Giacomelli *et al.*, Mutational processes shape the landscape of TP53 mutations in human cancer. *Nature genetics* **50**, 1381-1387 (2018).
104. L. M. Starita *et al.*, Massively Parallel Functional Analysis of BRCA1 RING Domain Variants. *Genetics* **200**, 413-422 (2015).
105. E. M. Jones *et al.*, Structural and functional characterization of G protein–coupled receptors with deep mutational scanning. *eLife* **9**, e54895 (2020).
106. C. E. G. Amorim *et al.*, The population genetics of human disease: The case of recessive, lethal mutations. *PLoS Genet* **13**, e1006915 (2017).
107. B. Quintans, A. Ordonez-Ugalde, P. Cacheiro, A. Carracedo, M. J. Sobrido, Medical genomics: The intricate path from genetic variant identification to clinical interpretation. *Appl Transl Genom* **3**, 60-67 (2014).
108. A. R. Martin *et al.*, PanelApp crowdsources expert knowledge to establish consensus diagnostic gene panels. *Nat Genet* **51**, 1560-1565 (2019).
109. A. Thormann *et al.*, Flexible and scalable diagnostic filtering of genomic variants using G2P with Ensembl VEP. *Nat Commun* **10**, 2373 (2019).

110. L. F. Kuderna *et al.*, A global catalog of whole-genome diversity from 233 primate species *Submitted*.
111. C. A. Cassa *et al.*, Estimating the selective effects of heterozygous protein-truncating variants from human exome data. *Nat Genet* **49**, 806-810 (2017).
112. C. Tyner *et al.*, The UCSC Genome Browser database: 2017 update. *Nucleic Acids Res* **45**, D626-D634 (2017).
113. W. J. Kent, C. W. Sugnet, T. S. Furey, K. M. Roskin, T. H. Pringle, A.M. Zahler, D. Haussler, The human genome browser at UCSC. *Genome Res.* **12**, 996-1006 (2002).
114. D. P. Genereux *et al.*, A comparative genomics multitool for scientific discovery and conservation. *Nature* **587**, 240-245 (2020).
115. B. E. Suzek, Y. Wang, H. Huang, P. B. McGarvey, C. H. Wu, UniRef clusters: a comprehensive and scalable alternative for improving sequence similarity searches. *Bioinformatics (Oxford, England)* **31**, 926-932 (2015).
116. A. Sali, T. L. Blundell, Comparative protein modelling by satisfaction of spatial restraints. *J Mol Biol* **234**, 779-815 (1993).
117. R. K. Pasumarthi *et al.*, TF-Ranking: Scalable TensorFlow Library for Learning-to-Rank. *Proceedings of the 25th ACM SIGKDD International Conference on Knowledge Discovery and Data Mining*, 2970--2978 (2019).
118. B. E. Suzek, H. Huang, P. McGarvey, R. Mazumder, C. H. Wu, UniRef: comprehensive and non-redundant UniProt reference clusters. *Bioinformatics* **23**, 1282-1288 (2007).
119. B. E. Suzek, Y. Wang, H. Huang, P. B. McGarvey, C. H. Wu, UniRef clusters: a comprehensive and scalable alternative for improving sequence similarity searches. *Bioinformatics* **31**, 926-932 (2015).
120. X. Jia *et al.*, Massively parallel functional testing of MSH2 missense variants conferring Lynch syndrome risk. *Am J Hum Genet* **108**, 163-175 (2021).
121. M. A. Chiasson *et al.*, Multiplexed measurement of variant abundance and activity reveals VKOR topology, active site and human variant impact. *Elife* **9**, (2020).
122. L. M. Starita *et al.*, Massively Parallel Functional Analysis of BRCA1 RING Domain Variants. *Genetics* **200**, 413-422 (2015).
123. A. O. Giacomelli *et al.*, Mutational processes shape the landscape of TP53 mutations in human cancer. *Nature Genetics* **50**, 1381-1387 (2018).
124. E. M. Jones *et al.*, Structural and functional characterization of G protein–coupled receptors with deep mutational scanning. *Elife* **9**, e54895 (2020).
125. S. Gudmundsson *et al.*, Addendum: The mutational constraint spectrum quantified from variation in 141,456 humans. *Nature* **597**, E3-E4 (2021).
126. D. Vanderpool *et al.*, Primate phylogenomics uncovers multiple rapid radiations and ancient interspecific introgression. *PLoS Biol* **18**, e3000954 (2020).
127. P. J. Cock *et al.*, Biopython: freely available Python tools for computational molecular biology and bioinformatics. *Bioinformatics* **25**, 1422-1423 (2009).
128. M. A. Eberle *et al.*, A reference data set of 5.4 million phased human variants validated by genetic inheritance from sequencing a three-generation 17-member pedigree. *Genome Res* **27**, 157-164 (2017).
129. M. de Manuel *et al.*, Chimpanzee genomic diversity reveals ancient admixture with bonobos. *Science* **354**, 477-481 (2016).
130. E. M. Leffler, Z. Gao, S. Pfeifer, L. Ségurel, A. Auton, O. Venn, R. Bowden, R. Bontrop, J.D. Wall, G. Sella, P. Donnelly, Multiple instances of ancient balancing selection shared between humans and chimpanzees. *Science* **339**, 1578-1582 (2013).

131. K. E. Eilertson, J. G. Booth, C. D. Bustamante, SnIPRE: Selection Inference Using a Poisson Random Effects Model. *PLoS Comput Biol* **8**, e1002806 (2012).
132. S. F. Altschul, W. Gish, W. Miller, E. W. Myers, D. J. Lipman, Basic local alignment search tool. *J Mol Biol* **215**, 403-410 (1990).
133. L. S. Johnson, S. R. Eddy, E. Portugaly, Hidden Markov model speed heuristic and iterative HMM search procedure. *BMC Bioinformatics* **11**, 431 (2010).
134. M. Baek *et al.*, Accurate prediction of protein structures and interactions using a three-track neural network. *Science* **373**, 871-876 (2021).
135. D. S. Marks *et al.*, Protein 3D structure computed from evolutionary sequence variation. *PLoS One* **6**, e28766 (2011).
136. D. Kingma, J. Ba, Adam: A method for stochastic optimization. *arXiv preprint arXiv:1412.6980*, (2014).
137. M. Mirdita *et al.*, Uniclust databases of clustered and deeply annotated protein sequences and alignments. *Nucleic Acids Research* **45**, D170-D176 (2017).
138. M. Steinegger *et al.*, HH-suite3 for fast remote homology detection and deep protein annotation. *BMC Bioinformatics* **20**, 473 (2019).
139. R. M. Rao *et al.,* M. Meila, T. Zhang, Eds. (PMLR, 2021), vol. 139, pp. 8844-8856.
140. J. L. Ba, J. R. Kiros, G. E. Hinton, paper presented at the Advances in NIPS 2016 Deep Learning Symposium, 2016 2016.
141. D. Hendrycks, K. Gimpel, Gaussian Error Linear Units (GELUs). *arXiv preprint arXiv:1606.08415*, (2020).
142. N. Srivastava, G. Hinton, A. Krizhevsky, I. Sutskever, R. Salakhutdinov, Dropout: A Simple Way to Prevent Neural Networks from Overfitting. *Journal of Machine Learning Research* **15**, 1929-1958 (2014).
143. P. Micikevicius *et al.*, Mixed Precision Training. *International Conference on Learning Representations*, (2018).
144. S. Rajbhandari, J. Rasley, O. Ruwase, Y. He, ZeRO: Memory Optimizations Toward Training Trillion Parameter Models. *Proceedings of the International Conference for High Performance Computing, Networking, Storage and Analysis*, 1-16 (2020).
145. P. Bandaru *et al.*, Deconstruction of the Ras switching cycle through saturation mutagenesis. *Elife* **6**, (2017).
146. J. Weile *et al.*, A framework for exhaustively mapping functional missense variants. *Mol Syst Biol* **13**, 957 (2017).
147. L. Brenan *et al.*, Phenotypic Characterization of a Comprehensive Set of MAPK1/ERK2 Missense Mutants. *Cell Rep* **17**, 1171-1183 (2016).
148. M. M. Awad *et al.*, Acquired Resistance to KRASG12C Inhibition in Cancer. *New England Journal of Medicine* **384**, 2382-2393 (2021).
149. L. Zhang *et al.*, SLCO1B1: Application and Limitations of Deep Mutational Scanning for Genomic Missense Variant Function. *Drug Metab Dispos*, DMD-AR-2020-000264 (2021).
150. V. E. Gray *et al.*, Elucidating the Molecular Determinants of Aβ Aggregation with Deep Mutational Scanning. *G3 (Bethesda)* **9**, 3683-3689 (2019).
151. I. A. Adzhubei *et al.*, A method and server for predicting damaging missense mutations. *Nature Methods* **7**, 248-249 (2010).
152. B.-J. Feng, PERCH: A Unified Framework for Disease Gene Prioritization. *Human Mutation* **38**, 243-251 (2017).

153. P. Rentzsch, M. Schubach, J. Shendure, M. Kircher, CADD-Splice-improving genome-wide variant effect prediction using deep learning-derived splice scores. *Genome Medicine* **13**, 31 (2021).
154. D. Quang, Y. Chen, X. Xie, DANN: a deep learning approach for annotating the pathogenicity of genetic variants. *Bioinformatics* **31**, 761-763 (2015).
155. D. Raimondi *et al.*, DEOGEN2: prediction and interactive visualization of single amino acid variant deleteriousness in human proteins. *Nucleic Acids Research* **45**, W201-W206 (2017).
156. N. Malhis, M. Jacobson, S. J. M. Jones, J. Gsponer, LIST-S2: taxonomy based sorting of deleterious missense mutations across species. *Nucleic Acids Research* **48**, W154-W161 (2020).
157. K. A. Jagadeesh *et al.*, M-CAP eliminates a majority of variants of uncertain significance in clinical exomes at high sensitivity. *Nature Genetics* **48**, 1581-1586 (2016).
158. R. Steinhaus *et al.*, MutationTaster2021. *Nucleic Acids Research* **49**, W446-W451 (2021).
159. Y. Choi, G. E. Sims, S. Murphy, J. R. Miller, A. P. Chan, Predicting the functional effect of amino acid substitutions and indels. *PLoS One* **7**, e46688 (2012).
160. N. M. Ioannidis *et al.*, REVEL: An Ensemble Method for Predicting the Pathogenicity of Rare Missense Variants. *Am J Hum Genet* **99**, 877-885 (2016).
161. N.-L. Sim *et al.*, SIFT web server: predicting effects of amino acid substitutions on proteins. *Nucleic Acids Research* **40**, W452-457 (2012).
162. H. Carter, C. Douville, P. D. Stenson, D. N. Cooper, R. Karchin, Identifying Mendelian disease genes with the variant effect scoring tool. *BMC Genomics* **14 Suppl 3**, S3 (2013).
163. H. A. Shihab *et al.*, An integrative approach to predicting the functional effects of non-coding and coding sequence variation. *Bioinformatics* **31**, 1536-1543 (2015).
164. J. Meier *et al.*, Language models enable zero-shot prediction of the effects of mutations on protein function. *bioRxiv*, (2021).
165. A. J. Riesselman, J. B. Ingraham, D. S. Marks, Deep generative models of genetic variation capture the effects of mutations. *Nat Methods* **15**, 816-822 (2018).
166. P. D. Stenson *et al.*, Human Gene Mutation Database: towards a comprehensive central mutation database. *J Med Genet* **45**, 124-126 (2008).
167. P. D. Stenson *et al.*, The Human Gene Mutation Database (HGMD((R))): optimizing its use in a clinical diagnostic or research setting. *Hum Genet* **139**, 1197-1207 (2020).
168. Y. Zhang, J. Skolnick, Scoring function for automated assessment of protein structure template quality. *Proteins* **57**, 702-710 (2004).
169. M. Ekeberg, C. Lövkvist, Y. Lan, M. Weigt, E. Aurell, Improved contact prediction in proteins: Using pseudolikelihoods to infer Potts models. *Physical Review E* **87**, 012707 (2013).

Acknowledgments: We would like to thank Daniel MacArthur, Yun Song, and Mark Daly for helpful discussions, and the gnomAD team at the Broad Institute for their assistance with the website.

Funding: LFKK was supported by an EMBO STF 8286 (to LFKK). MCJ was supported by (NERC) NE/T000341/1 (to RMDB, JPB, IG, DdV and MCJ). MK was supported by "la Caixa" Foundation (ID 100010434 to MK), fellowship code LCF/BQ/PR19/11700002 (to MK), and by the Vienna Science and Technology Fund (WWTF) and the City of Vienna through project VRG20-001 (to MK). JDO was supported by "la Caixa" Foundation (ID 100010434 to JDO) and the European Union's Horizon 2020 research and innovation programme under the Marie Skłodowska-Curie grant agreement No 847648 (to JDO). The fellowship code is LCF/BQ/PI20/11760004 (to JDO). FES was supported by Brazilian National Council for Scientific and Technological Development (CNPq) (Process nos.: 303286/2014-8, 303579/2014-5, 200502/2015-8, 302140/2020-4, 300365/2021-7, 301407/2021-5, 301925/2021-6 to FES), and received funding from the European Union's Horizon 2020 research and innovation programme under the Marie Skłodowska-Curie grant agreement No 801505 (to FES). Fieldwork for samples collected in the Brazilian Amazon was funded by grants from Conselho Nacional de Desenvolvimento Científico e Tecnológico (CNPq/SISBIOTA Program #563348/2010-0 to IPF), Fundação de Amparo à Pesquisa do Estado do Amazonas (FAPEAM/SISBIOTA #2317/2011 to IPF), and Coordenação de Aperfeiçoamento de Pessoal de Nível Superior (CAPES AUX # 3261/2013) to IPF. Sampling of nonhuman primates in Tanzania was funded by the German Research Foundation (KN1097/3-1 to SK and RO3055/2-1 to CR) and by the US National Science Foundation (BNS83-03506 to JPC). No animals in Tanzania were sampled purposely for this study. Details of the original study on Treponema pallidum infection can be requested from SK. Sampling of baboons in Zambia was funded by US NSF grant BCS-1029451 to JPC, CJJ and JR. The research reported in this manuscript was also funded by the Vietnamese Ministry of Science and Technology's Program 562 (grant no. ĐTĐL.CN-64/19). ANC is supported by AEI-PGC2018-101927-BI00 704 (FEDER/UE to ANC), FEDER (Fondo Europeo de Desarrollo Regional)/FSE (Fondo Social Europeo), "Unidad de Excelencia María de Maeztu", funded by the AEI (CEX2018-000792-M to ANC) and Secretaria d'Universitats i Recerca and CERCA Programme del Departament d'Economia i Coneixement de la Generalitat de Catalunya (GRC 2017 SGR 880 to ANC). ADM was supported by the National Sciences and Engineering Research Council of Canada and Canada Research Chairs program. The authors would like to thank the Veterinary and Zoology staff at Wildlife Reserves Singapore for their help in obtaining the tissue samples, as well as the Lee Kong Chian Natural History Museum for storage and provision of the tissue samples. We wish to thank H. Doddapaneni, D.M. Muzny and M.C. Gingras for their support of sequencing at the Baylor College of Medicine Human Genome Sequencing Center. We greatly appreciate the support of Richard Gibbs, Director of HGSC for this project and thank Baylor College of Medicine for internal funding. TMB is supported by funding from the European Research Council (ERC) under the European Union's Horizon 2020 research and innovation programme (grant agreement No. 864203 to TMB), BFU2017-86471-P (MINECO/FEDER, UE to TMB), "Unidad de Excelencia María de Maeztu", funded by the AEI (CEX2018-000792-M to TMB), NIH 1R01HG010898-01A1 (to TMB) and Secretaria d'Universitats i Recerca and CERCA Programme del Departament d'Economia i Coneixement de la Generalitat de Catalunya (GRC 2021 SGR 00177 to TMB), Howard Hughes International Early Career (to TMB), Obra Social "La Caixa" and internal funds from Baylor College of Medicine. HLR receives funding from Illumina, Inc to support rare disease gene discovery and diagnosis. JPB, RMDB, IG and DV were supported by a UKRI Grant NERC (NE/T000341/1). We thank Dr. Praveen Karanth (IISc), Dr. H.N. Kumara (SACON) for collecting and providing us with some of the samples from India. SMA was supported by a BINC fellowship from the Department of Biotechnology (DBT), India. We acknowledge the support provided by the Council of Scientific and Industrial Research (CSIR), India to GU for the sequencing at the Centre for Cellular and Molecular Biology (CCMB), India. Aotus azarae samples from Argentina where obtained with grant support to EFD from the Zoological Society of San Diego, Wenner-Gren Foundation, the L.S.B. Leakey Foundation, the National Geographic Society, the U.S. National Science Foundation (NSF-BCS-0621020, 1232349, 1503753, 1848954; NSF-RAPID-1219368, NSF-FAIN-1952072; NSF-DDIG-1540255; NSF-REU 0837921, 0924352, 1026991) and the U.S. National Institute on Aging (NIA- P30 AG012836-19, NICHD R24 HD-044964-11). JHS was supported in part by the NIH under award number P40OD024628 - SPF Baboon Research Resource. This research is supported by the National Research Foundation Singapore under its National Precision Medicine Programme (NPM) Phase II Funding (MOH-000588 to PT and WKL) and administered by the Singapore Ministry of Health's National Medical ResearchCouncil. JR is also a Core Scientist at the Wisconsin National Primate Research Center, Univ. of Wisconsin, Madison.

Author contributions: HG, TH, JE, JGS, JM, MSB, YY, AD, PF, LK, LS, YW, AA, YF, SC, SB, GL, RR, DB, FA, KF performed the analysis and wrote the manuscript. MCJ, MK, JDO, SM, AV, JB, MR, FES, LA, JB, MG, DdV, IG, RAH, MR, AJ, ISC, JH, CH, DJ, PF, FRdM, FB, HB, IS, IF, JVdA, MM, MNFdS, MT, RR, TH, NA, CJR, AZ, CJJ, JPC, GW, CA, JHS, EFD, SK, FS, DW, LZ, YS, GZ, JDK, SK, MDL, EL, SM, AN, TB, TN, CCK, JL, PT, WKL, ACK, DZ, IG, AM, KG, MHS, RMDB, GU, CR, JPB contributed the primate samples and sequencing data. ML, SS, AOD, HR, JX, JR, TMB, and KF supervised the work.

1. **Competing interests:** Employees of Illumina Inc are indicated in the list of author affiliations. Patents related to this work are (1) title: Deep convolutional neural networks to predict variant pathogenicity using three-dimensional (3D) protein structures, filing No.: US 17/232,056; (2) title: Transfer learning-based use of protein contact maps for variant pathogenicity prediction, filing No.: US 17/876,481; (3) title: Multi-channel protein voxelization to predict variant pathogenicity using deep convolutional neural networks, filing No.: US 17/703,935.(4) title: Transformer language model for variant pathogenicity, filing No.: US 17/975,536 and US 17/975,547.

Data and materials availability: All sequencing data have been deposited at the European Nucleotide Archive under the accession number PRJEB49549. Primate variants and PrimateAI-3D prediction scores are available with a non-commercial license upon request and are displayed on https://primad.basespace.illumina.com. The source code of PrimateAI-3D is accessible via https://github.com/Illumina/PrimateAI-3D. To reduce problems with circularity that have become a concern for the field, the authors explicitly request that the prediction scores from the method not be incorporated as a component of other classifiers, and instead ask that interested parties employ the provided source code and data to directly train and improve upon their own deep learning models.

Supplementary Materials:

Materials and Methods

Supplementary Text

Figs. S1 to S28

Tables S1 to S6

References (*125-169*)

Figures

Fig. 1. Common primate variants are largely benign in human. (**A**) Counts of missense (solid green) and synonymous (shaded grey) variants from primates compared to the gnomAD database. Missense : synonymous counts and ratios are displayed above each bar. (**B**) Fractions of all possible human synonymous (grey) and missense variants (green) observed in primates. (**C**) Counts of benign (grey) and pathogenic (red) missense variants with two-star review status or above in the overall ClinVar database (left pie chart), compared to ClinVar variants observed in gnomAD (middle), and compared to ClinVar variants observed in primates (right). Conflicting benign and pathogenic annotations and variants interpreted only with uncertain significance were excluded. (**D**) Observed gnomAD (green) or primate (blue) missense variants in each amino acid position in the *CACNA1A* gene. Red circles represent the positions of annotated ClinVar pathogenic missense variants. Bottom scatterplot shows PrimateAI-3D predicted pathogenicity scores for all possible missense substitutions along the gene. (**E**) Multiple sequence alignment showing the ClinVar pathogenic variant chr11:77181548 G>A (red arrow) creating a cryptic splice site in human sequence (extended splice motif, blue). This variant is tolerated in *Cebus Albifrons* and other species with a G>C synonymous change in the adjacent nucleotide that stops the splice motif from forming. (**F**) Pie charts showing the fraction of benign (grey) and pathogenic (red) missense variants with ClinVar two-star review status or above in great apes, old world monkeys, new world monkeys, lemurs/tarsiers, mammals, chicken, and zebrafish. (**G**) Missense : synonymous ratios (MSR) across the human allele frequency spectrum, with MSR of human variants seen in primates shown for comparison. The blue dashed line represents the expected missense : synonymous ratio of de novo variants. Colors and legend are the same as (**A**).

Fig. 2. Selective constraint of primate genes compared to human. (**A**) Scatter plot of missense : synonymous ratios between primate and human genes. Each gene is colored by its pLI score, with darker points showing haploinsufficient genes. (**B**) Observed and expected counts of synonymous (top) and missense (bottom) variants per gene in gnomAD (left) and primates (right). Genes are colored by their pLI scores. (**C**) Distributions of observed/expected ratios of synonymous (dashed lines) and missense (solid lines) variants for all genes. Results for primate genes (orange) and gnomAD genes (blue) are shown. (**D**) Scatter plot of missense : synonymous ratios between primate and human genes. Highlighted points are genes that are under significantly stronger (blue) or weaker (red) constraint in humans compared to non-human primates under both methods (Benjamini-Hochberg FDR < 0.05), while grey points show non-significant genes. The top 10 genes with the largest effect sizes in either direction are labeled.

Fig. 3. PrimateAI-3D architecture and variant classification performance. (**A**) PrimateAI-3D workflow. Human protein structures and multiple sequence alignments are voxelized (left) as input to a 3D convolutional neural network that predicts pathogenicity of all possible point mutations of a target residue (middle). The network is trained using a loss function with three components (right): common human and primate variants; fill-in-the-blank of a protein structure; score ranks from language models. (**B**) Protein structure of the *STK11* gene, colored by PrimateAI-3D pathogenicity prediction scores (blue: benign; red: pathogenic). Spheres indicate residues with common human and primate variants (left) or residues with pathogenic mutations

from ClinVar (right). For spheres, the color corresponds to the pathogenicity score of only the variant. For other residues, pathogenicity scores are averaged over all variants at that site. (**C**) Scatterplot shows performance of methods that predict missense variant pathogenicity in two clinical benchmarks (DDD and UKBB). Datasets are a subset of variants for which all methods have predictions. (D) Six barplots show method performance for six testing datasets (DMS assays, UKBB, ClinVar, DDD, ASD, and CHD).

Fig. 4. Impact of training dataset size on classification accuracy. (**A**) Improved performance of PrimateAI-3D with increasing number of common human and primate variants in the training dataset (x-axis). Performance of each dataset (y-axis) was divided by the maximum performance observed across all training dataset sizes. (**B**) Cumulative fractions of all possible human synonymous (grey) and missense (green) variants observed as common variants in 234 primate species, including human (allele frequency > 0.1%). Each point shows the average of ten permutations, calculated with a different random ordering of the list of primate species each time.

Fig. 5. Enrichment of de novo mutations in the neurodevelopmental disorder cohort over expectation. (**A**) Enrichment of DNMs from Kaplanis *et al. (87)* across all genes. Enrichment ratios are given for synonymous, all missense, and protein-truncating variants (PTV), along with missense split by PrimateAI-3D score into benign (<0.821) and pathogenic (>0.821). (**B**) Enrichment of benign and pathogenic missense above expectation at varying PrimateAI-3D thresholds for classifying pathogenic missense.

		Missense		*P* value	
HGNC symbol	Protein-truncating variants	PrimateAI-3D score ≥ 0.821	All missense	PrimateAI-3D score ≥ 0.821	All missense
AP1G1	2	4	5	4.1×10^{-7}	5.9×10^{-5}
ATP2B2	1	9	11	$2.1\times10\text{-}^{7}$	1.4×10^{-3}
CELF2	2	4	4	1.2×10^{-7}	6.7×10^{-5}
MAP4K4	2	6	7	3.9×10^{-7}	5.0×10^{-4}
MED13	3	6	9	6.6×10^{-8}	3.5×10^{-5}
MFN2	0	6	8	3.4×10^{-7}	1.0×10^{-5}
NR4A2	2	4	5	3.7×10^{-7}	3.3×10^{-5}
PIP5K1C	0	8	9	2.8×10^{-8}	4.9×10^{-4}
RAB5C	2	4	5	8.6×10^{-8}	1.5×10^{-5}
SPOP	1	4	6	4.1×10^{-7}	1.7×10^{-6}
SPTBN2	1	10	16	3.9×10^{-7}	4.5×10^{-3}
XPO1	1	7	7	5.0×10^{-7}	7.2×10^{-4}
EIF4A2	2	4	4	1.7×10^{-7}	2.1×10^{-4}
LMBRD2	0	3	4	6.0×10^{-7}	1.3×10^{-4}
MARK2	4	3	5	2.3×10^{-7}	3.8×10^{-5}
NOTCH1	4	6	17	4.1×10^{-7}	1.3×10^{-6}

Table 1. Additional genes discovered in intellectual disability. Genes achieving the genome-wide significance ($p < 6.4x10^{-7}$) are shown when considering only missense de novo mutations (DNMs) with PrimateAI-3D scores ≥0.821. Counts of protein truncating and missense DNMs are provided. *P* values for gene enrichment are shown when the statistical test was run only with missense mutations with PrimateAI-3D score ≥ 0.821, and when it was repeated for all missense mutations.

Science
AAAS

Supplementary Materials for

The landscape of tolerated genetic variation in humans and primates

Hong Gao[1]†, Tobias Hamp[1]†, Jeffrey Ede[1], Joshua G. Schraiber[1], Jeremy McRae[1], Moriel Singer-Berk[2], Yanshen Yang[1], Anastasia Dietrich[1], Petko Fiziev[1], Lukas Kuderna[1,3], Laksshman Sundaram[1], Yibing Wu[1], Aashish Adhikari[1], Yair Field[1], Chen Chen[1], Serafim Batzoglou[1], Francois Aguet[1], Gabrielle Lemire[2,4], Rebecca Reimers[4], Daniel Balick[5], Mareike C. Janiak[6], Martin Kuhlwilm[3,7,8], Joseph D. Orkin[3,9], Shivakumara Manu[10,11], Alejandro Valenzuela[3], Juraj Bergman[12,13], Marjolaine Rouselle[12], Felipe Ennes Silva[14,15], Lidia Agueda[16], Julie Blanc[16], Marta Gut[16], Dorien de Vries[6], Ian Goodhead[6], R. Alan Harris[17], Muthuswamy Raveendran[17], Axel Jensen[18], Idriss S. Chuma[19], Julie Horvath[20,21,22,23,24], Christina Hvilsom[25], David Juan[3], Peter Frandsen[25], Fabiano R. de Melo[26], Fabricio Bertuol[27], Hazel Byrne[28], Iracilda Sampaio[29], Izeni Farias[27], João Valsecchi do Amaral[30,31,32], Malu Messias[33], Maria N. F. da Silva[34], Mihir Trivedi[11], Rogerio Rossi[35], Tomas Hrbek[27,36], Nicole Andriaholinirina[37], Clément J. Rabarivola[37], Alphonse Zaramody[37], Clifford J. Jolly[38], Jane Phillips-Conroy[39], Gregory Wilkerson[40], Christian Abee[40], Joe H. Simmons[40], Eduardo Fernandez-Duque[41], Sree Kanthaswamy[42], Fekadu Shiferaw[43], Dongdong Wu[44], Long Zhou[45], Yong Shao[44], Guojie Zhang[45,46,47,48,49], Julius D. Keyyu[50], Sascha Knauf[51], Minh D. Le[52], Esther Lizano[3,53], Stefan Merker[54], Arcadi Navarro[3,55,56,57], Thomas Batallion[12], Tilo Nadler[58], Chiea Chuen Khor[59], Jessica Lee[60], Patrick Tan[59,61,62], Weng Khong Lim[61,62,63], Andrew C. Kitchener[64,65], Dietmar Zinner[66,67,68], Ivo Gut[16], Amanda Melin[69,70], Katerina Guschanski[18,71], Mikkel Heide Schierup[12], Robin M. D. Beck[6], Govindhaswamy Umapathy[10,11], Christian Roos[72], Jean P. Boubli[6], Monkol Lek[73], Shamil Sunyaev[74,5], Anne O'Donnell[2,4,75], Heidi Rehm[2,75], Jinbo Xu[1,76], Jeffrey Rogers[17]*, Tomas Marques-Bonet[3,16,53,55]*, Kyle Kai-How Farh[1]*

Correspondence to: tomas.marques@upf.edu, jr13@bcm.edu, kfarh@illumina.com

This PDF file includes:

Materials and Methods
Supplementary Text
Figs. S1 to S28
Captions for Tables S1 to S6
References *(125-169)*

Materials and Methods

Data generation

Generation of canonical gene set

All coordinates used in the paper refer to human genome build UCSC hg38 / GRCh38, including the coordinates for variants in other species. Protein-coding DNA sequences and multiple sequence alignments of 99 vertebrate genomes with human were downloaded from the UCSC genome browser for the hg38 build. (http://hgdownload.soe.ucsc.edu/goldenPath/hg38/multiz100way/alignments/knownCanonical.exonNuc.fa.gz) (*112, 113*). For genes with multiple canonical gene annotations, the coding transcript with the highest conservation score across the MSA was selected. In total, 19,158 transcripts were selected to represent the canonical gene sets used for all the analyses in this paper.

Human polymorphism data

We downloaded human polymorphism data from genome Aggregation Database v2.1.1, which collected the whole-exome sequencing data of 125,748 individuals (gnomad.exomes.r2.1.1.sites.vcf.bgz file) and the whole-genome sequencing of 71,702 individuals from gnomAD v3.0 (http://gnomad.broadinstitute.org/) (*28, 29, 125*). For the subsequent analyses using gnomAD dataset, we used a merged variant set between gnomAD WES and WGS. We also collected variants from 65K TOPMed WGS (*77, 78*) and 200K UK Biobank WGS (*79, 80*) and merged those with gnomAD (after removing 2,404 TOPMed samples from gnomAD). We excluded variants that failed the default quality control filters as annotated in VCF files or fell outside canonical coding regions. To avoid effects due to balancing selection, we also excluded variants from the extended MHC region (chr6: 28,510,120 – 33,480,577) for the subsequent analyses. In total, we obtained 126,873 unique common missense variants (allele frequency > 0.1%) and 7,306,297 unique rare missenses (allele frequency < 0.1%), which were included in the benign set for training of primateAI-3D. We also performed mutation rate correction on gnomAD variants following our previous paper (*17*) for missense : synonymous ratio analyses.

Primate sequencing data

We sequenced and aggregated the whole genomes of 809 primate samples across 233 primate species, which included samples from Great Ape Genome project (*19*) and other previous studies (*20-26, 126*). Among these, 783 samples passed quality evaluation and 26 samples failed QC. The major challenge of variant calling of these samples is that fewer than 60 primate species have genome builds available and the majority of samples are lack of reference genomes. Therefore, variant calling is performed using reference genomes from the closest species of primate samples. We aligned the sequencing data to 32 high-quality genome references (*110*), most of which are derived from long-read sequencing technologies. We adopted multiple hard filtering steps to remove low quality variants (*110*). As variants that are identity-by-state with human are of primary interest, we derived lift-over chain files between hg38 and each primate reference species from the multiple species alignment of 50 primate species and 8 mammal species (*110*) and lifted over the variants of primate samples to hg38. We examined the quality of coding variants by evaluating several QC metrics, including the number of stop-gained variants called per sample, the missense : synonymous ratios and the number of indels per sample.

Machine learning classifiers of variants

Due to the lack of reference genomes for the majority of primate species, we conducted a synthetic experiment to evaluate the impact of mapping to reference genomes of closely-related species on variant calling. We took a gorilla sample and mapped it to both hg38 and the gorilla genome (*110*). Mapping to gorilla and lifting-over to hg38 produced 6.6M variants after hard-filtering; while mapping to hg38 resulted in 45.4M variants. After hard filtering of low-quality variants and removing 38M fixed substitutions between hg38 and the gorilla genome, we observed 4.9M variants were shared between the two sets and 801.3K variants were called against hg38 but not called against gorilla. These variants are mostly false positives due to sequencing reads that were mapped to an incorrect region of the human genome or to regions of the human genome that are duplicated compared to the gorilla genome. It is essential to reduce these false positive variants substantially.

We developed machine learning classifiers to distinguish these false positive variants from the high quality variants for each primate sample. To train the classifiers, we used multiple sequence features per variant: GC content, GC skewness and local composition complexity within +/-100bp of variants (*127*). In addition, we extracted variant features directly from VCF files, such as allelic count, mapping quality, the p-value of Fisher's exact test to detect strand bias, variant quality by depth, the symmetric odds ratio to detect strand bias, and genotype quality. We included the read depth (DP) of the variant normalized by the mean coverage of the primate sample and the fraction of alternative allele read depth out of the variant coverage. We observed that existence of indels nearby substantially influences the quality of variants called, thus we indicated indels within +/- 5bp and 10bp of variants. We also considered variant context features, including the mean coverage of the flanking regions around the variant normalized by the mean coverage of the primate sample, e.g., within +/- 100bp or +/- 500bp of the variant. Additionally, we observed that false positive variants often reside in poorly-mapped regions, which tend to accumulate overcalled variants. We counted the number of heterozygote SNPs within the flanking regions of variants (within +/- 100bp or +/- 500bp), which are normalized by the median counts of variants within the same length regions of the sample. Likewise, we included the normalized counts of alternative homozygote variants within the flanking regions of variants.

We labelled the 801.3K false positives as poor-quality variants and the remaining 44.6M variants as good-quality, including the 38M fixed substitutions. We randomly sampled 80% of the variant set for training and the rest 20% for testing. Various classification methods were evaluated, including random forest (RF), logistic regression, and multi-layer perceptron network. Random forest classifiers outperformed other methods with higher area under receiver operating characteristic (ROC) curve. We then independently trained six random forest classifiers using six gorilla samples by repeating the steps above and generated predicted scores for each variant using the six classifiers. The averaged predicted scores are denoted as the RF score of the variant. We chose a stringent cut-off of <0.05 for RF scores to minimize the effect of poor-quality variant calling on the ClinVar and other analyses.

We next evaluated the impact of applying the trained RF classifiers to other gorilla samples, which also showed comparable area under ROC curve. We then assessed whether the trained RF classifiers can be applied to other species pairs. Because reference genomes are unavailable for the majority of our species, we cannot directly assess the number of false positives when mapping to the close species. Instead, we designed several experiments to evaluate the accuracy of the gorilla-trained classifier that make use of the reference genomes we had in hand. First, we mapped a gorilla sample to the chimpanzee genome and applied the classifiers previously trained between gorilla and human. Second, we chose another pair of primates, rhesus macaque and baboon, to test the performance of the same classifiers. Last, we took human samples from an independent data set, Platinum Genomes project (*128*) and mapped those to chimpanzee and gorilla genomes. We also trained a second random forest classifier using the human and chimpanzee pairs and tested the performance of trained classifiers on human and gorilla pairs. All the results show the classifiers trained on one pair of closely-related species are generally applicable to another pair of closely-related species with comparable area under ROC.

Cascaded variant filtering

In addition to random forest filtering, we performed extra variant filtering steps. First, because we are interested in learning about pathogenicity of coding variants in humans, we removed variants that fell in codons where neither the reference nor the alternative allele resulted in a codon that matched the human codon at that position. Interestingly, this codon-match indicator also naturally reflects the clustering of these primate reference species into four major groups, great apes, Old World monkeys, New World monkeys and lemurs / tarsiers, as shown in the heatmap of Fig. S1A. Requiring codon match between primate and human genomes eliminated more than 50% of stop-gained variants in our primate dataset.

Next, we applied a series of gene-specific filtering steps to reduce the poor-quality primate variants in samples of each primate reference species. We excluded variants falling in primate transcripts carrying annotation errors compared with human transcripts, such as those with incorrect start codons or splicing donor and acceptor sites, which implies that transferring the human annotation directly to primates may have been problematic for these transcripts. We also removed variants in primate transcripts carrying in the middle of the sequence stop-gained variants that were not observed in the list of gnomAD protein-truncating variants.

We compared the distribution of variant random forest scores of a gene with the exome-wide distribution of variant RF scores and removed all variants in genes with a skewed distribution (Wilcoxon rank sum test p-value < 1e-20). We also merged the variants from all the samples mapped to a specific reference species and performed the Hardy-Weinberg equilibrium test for variants in primate reference species with at least seven samples. We then removed variants in the genes that carry any variants with excessive heterozygosity which also deviate from the Hardy-Weinberg proportions with p-value < 0.05.

In order to identify and exclude duplicated regions in primate genomes, we developed a unique mapping filter. First, we removed low quality sequencing reads of primate samples by filtering out reads with mapping quality < 20 from sample BAM files; then, we mapped the remaining reads to both hg38 and the relevant primate reference genome. We divided all reference genomes into 1kb bins and identified the best-mapped region in primate genomes as where the largest fraction of reads from one hg38 1kb bin are mapped (if reads from one hg38 1kb bin are mapped to two consecutive primate 1kb bins, the two bins are merged into one region). The fraction of reads from the hg38 bin that fall into the best-mapped region of the primate genome is the unique mapping score for that bin for each sample. By averaging the unique mapping scores across all the samples mapped to a specific reference species, we generated the unique-mapper (UM) score which applies to all the variants of the reference species that fall in the specific 1kb hg38 bin. For

ClinVar analyses, we chose a stringent cut-off of >90% for this score to ensure the one-to-one mapping between human and primate genomes.

These variant filters effectively reduced the number of stop-gained variants per primate sample to be close to the average number of stop-gained variants of human samples from Platinum Genomes project (*128*) (shown in Fig. S1B). The missense : synonymous ratios (MSR) gradually decreased after applying each of these filtering steps (Fig. S1C). In contrast, the missense : synonymous ratios of those excluded variants tend to be well above 1.0, implying they are either potentially deleterious or unreliably called. In addition, low-quality indels have also been substantially reduced (Fig. S1D).

Mammal polymorphisms

For mammal polymorphisms, we inherited the dbSNP variants of orangutan, rhesus, marmoset, cow, pig, mouse, goat, chicken and zebrafish from our previous paper (*17*) and lifted those over to hg38. We then excluded variants that failed codon-match requirement between hg38 and other species genomes. 109,732 unique missenses among the good quality variants of orangutan, rhesus, and marmoset were included in the training data set of PrimateAI-3D.

For each of primate, mammal and other vertebrate species, we computed a depletion metric following our previous paper (*17*), which measures the decrease of MSR of gnomAD common variants which are identical-by-state with other species, compared to the MSR of orthologous rare variants (Fig. S5).

Evaluation of fraction of common variants in primate polymorphisms

Due to that the averaged sample size per primate species is 2.5, we investigated the impact of small sample size on the fraction of common variants (allele frequency > 0.1% in each primate species) in the primate polymorphisms.

We then used the gnomAD allele frequencies of human common variants to simulate allele frequency spectra of primates at various sample sizes. For each primate species, we sampled genotypes according to gnomAD allele frequencies assuming the sample size is identical to that of the primate species. The fraction of gnomAD common variants discovered was averaged across 100 simulations for that specific sample size. We pooled the variants across the 233 simulated primate species and estimated the fractions of common variants for missense and synonymous variants separately, which are shown as allele frequency spectra in Fig. S2. According to this simulation, it is estimated that 95.1% of observed variants (>95.1%) are common variants (>0.1%), ~ 3% of synonymous variants in primates are rare (allele frequency < 0.1%) while ~ 94% of primate missense variants are common. Since the human allele frequency spectrum would be expected to have a larger fraction of rare variants than most other primate species due to the recent exponential expansion of human population size, the actual proportion of primate variants that are common (>0.1%) may be substantially higher than the 95.1% we estimated from simulations with gnomAD data.

From this simulation, we also obtained the average numbers of common synonymous variants at various sample size levels, which are used in the saturation analysis.

Generation of training variant set for PrimateAI-3D

For the benign variant set, we first included 126,873 unique common missense variants from human population data. To generate the primate polymorphism benign set, we relaxed our filtering criteria as deep learning algorithms naturally tolerate noise and benefit more from larger amounts of training data. We still removed variants falling in poor-quality genes or genes with poor annotations. However, we relaxed the unique mapper score cut-off to > 60% and the random forest score to < 0.17 and obtained 4,315,321 unique missense variants from primate sequencing. After merging human and primate missenses with missenses from dbSNP primates and variants from study on chimpanzee and bonobos (*129*), we obtained 4,514,581 unique missenses for the benign set in total.

All possible missense variants were generated from each base position of canonical coding regions by substituting the nucleotide at the position to the other three nucleotides. We excluded variants falling in start or stop codons, resulting in 71,166,190 all possible missense variants. After removing 4,514,581 benign variants and 6,207,640 human rare variants, 60,443,969 variants with unknown significance were left.

ClinVar analysis of polymorphism data for human, primates, mammals, and other vertebrates

To examine the clinical impact of variants that are identical-by-state with primate species, we downloaded the release variant summary for the ClinVar database (ftp://ftp.ncbi.nlm.nih.gov/pub/clinvar/vcf_GRCh38/variant_20210328.vcf.gz released on 28-March-2021) (*4*). The database contained 872,942 variants on the hg38 genome build, of which 753,511 were single nucleotide variants. Synonymous and stop-gained variants in the ClinVar database were excluded. Next, we required variants to have two-star review status or above, which includes “criteria provided, multiple submitters, no conflicts” and “reviewed by expert panel”. We then removed those with unknown significance or conflicting interpretations of pathogenicity. We merged variants with Benign or Likely Benign annotations into a single category, as well merging variants with Pathogenic or Likely Pathogenic annotations. After these filtering steps, there were a total of 7,017 variants in the pathogenic category and 12,229 variants in the benign category (Fig. 1C).

We analyzed ClinVar variants that were identical-by-state with variation in primates, mammals and other vertebrates and compared to those present in human population, such as gnomAD database. A summary of the numbers of benign and pathogenic ClinVar variants that were present in great apes, Old World monkeys, New World monkeys, lemurs and tarsiers, more distant mammals, birds and fish is shown in Fig. 1F.

Saturation of all possible human synonymous mutations with increasing number of primate populations sequenced

We performed simulations to investigate the expected saturation of all ~22M possible human synonymous mutations by sampling common variants present in the 521 extant primate species. We considered various sample sizes for primates, including 10, 20, 50, 100, 200, 500 and 1000. In the previous section, we estimated the numbers of common synonymous variants observed in different sample sizes of humans via simulation.

For each primate species with each sample size, we simulated two times the number of common synonymous variants observed in human (allele frequency > 0.1%), because humans appear to have roughly half the number of variants per individual as other primate species (*130*). We assigned simulated variants based on the observed distribution of human common synonymous variants in the 192 trinucleotide contexts. For example, if 2% of human common synonymous variants were from the TAG>TCG trinucleotide context, we would require that 2% of the simulated variants were randomly sampled TAG>TCG mutations. This has the effect of controlling for the effects of mutational rate, genetic drift, and gene conversion bias, using trinucleotide context. The curves in Fig. S21 show the effects of varying the number of species, and the number of individuals per species on the saturation of the ~22 all possible human synonymous variants in the genome. With a small sample size of 10, more than 50% of human synonymous variants will be present in the 521 primate species. As the sample size per primate species increases to 1000, about 80% of human synonymous mutations will be covered if we can sequence all the extant primate species. With 521 primate species, all CpG transitions (100.0%) and non-CpG transitions (96.6%) would be observed, but only 62.3% of transversions would be covered, due to their much lower mutation rates. We note that this analysis assumes each species is a homogeneous population, which would underestimate the amount of variation due to subpopulation and subspecies structure; hence, saturating all transversions may still be likely within the 521 extant primate species.

Derivation of primate mutation rates and observed/expected ratios per gene

We estimated primate mutation rates using intronic sequences 50-200bp away from exons, where the impact of selection and other factors is minimal. We slid a window of 3 nucleotides along the intronic sequence in steps of one nucleotide and for each primate reference genome counted the number of each of the 64 possible trinucleotides. Next, we counted the number of variants with each of the 192 trinucleotide mutation contexts that were observed in all samples mapped to that reference genome. The ratio of the observed occurrences of each trinucleotide mutation context to the number of possible trinucleotides across the reference genome served as our estimate of the mutation rate.

Using these mutation rates, we computed the expected number of synonymous variants per gene for each primate reference species. We normalized our mutation rates to ensure that we expect the same total number of synonymous variants as are observed across the genome, although they may be distributed in different genes than are observed. To do this, we summed up the intronic mutation rates across the 192 trinucleotide contexts along the sequence of each gene and normalized this value by the total mutation rate of the whole exome. Multiplying the normalized mutation rate per gene with the total number of observed synonymous variants in that same gene, we generated the expected number of synonymous variants per gene. We then assessed the quality of primate mutation rates by computing the Spearman correlation between the observed and expected numbers of synonymous variants. The Spearman correlations vary from 0.295 to 0.925 among primate reference species due to the numbers of samples mapped to reference species range from 1 to 169.

Next, we evaluated multiple approaches to aggregating those mutation rates across primate reference species. First, we took the median of mutation rates across all the 31 non-human primate reference species. Second, as the mutation rate of one species is in practice interpreted as the probability of observing one mutation at a base position with one specific trinucleotide context, we computed the probability of observing at least one mutation across 31 reference species via a Binomial model for a specific base position with a trinucleotide context. Third, we calculated the same probability as the second approach except that at the base position that failed codon-match requirement, the mutation rate was assigned to zero. Last, we selected nine primate reference species with more than 20 samples and the Spearman correlation between the observed and expected numbers of synonymous variants > 0.75, including *Aotus nancymaae, Ateles fusciceps, Cebus albifrons, Cercopithecus mitis, Lemur catta, Macaca mulatta, Pithecia pithecia, Rhinopithecus roxellana,* and *Papio anubis*. We took the median of mutation rates generated from these nine species to represent the primate mutation rates.

For each set of aggregated mutation rates, we generated the expected numbers of synonymous variants per gene across all the primate samples and took the ratio between the observed and expected numbers of synonymous variants to produce the observed/expected (O/E) ratio of synonymous for each gene. We multiplied each type of aggregated primate mutation rates with their specific O/E ratios of synonymous variants of genes to produce a new set of mutational probabilities of variants. Next, we evaluated the four sets of aggregated mutation rates and these four sets of adjusted mutational probabilities using the Spearman correlation between the mutational probability of a variant and the indicator of its presence in primate variants or not across all possible synonymous variants in the exome. The median mutation rates of nine primate species adjusted by the O/E ratios of genes achieved the highest Spearman correlation of 0.414. These adjusted primate mutation rates also outperform directly applying gnomAD mutation rates

(*29, 47*) with the Spearman correlation of 0.367, implying that primates have different mutational preference from humans.

Likewise, we computed the expected number of missense variants per gene across all primate species using this optimal set of primate mutation rates, which was normalized using the identical correction factor of synonymous variants (Fig. 2B). We computed the O/E ratios for missenses per gene (Fig. 2C). We then multiplied this best set of primate mutation rates by the O/E ratios of synonymous to generate mutational probabilities for each of all possible missense variants, which are used to select the matched set of variants with unknown significance for the PrimateAI-3D training.

In comparison with human data, we adopted the gnomAD mutation rates (*29, 47*) and variants, and computed the observed and expected numbers of synonymous and missense variants using the similar approach, as well as the O/E ratios of genes for synonymous and missense variants, respectively, shown in Fig. 2B and 2C.

Identifying differential selection between humans and primates

We sought to develop a model to 1) quantify the broad-scale similarity of natural selection between humans and primates and 2) identify genes evolving subject to significantly different selective pressure in humans compared to primates. Because our strategy of mapping to divergent reference genomes means that some observed variants within a primate species are actually fixed differences between that species and the reference to which it was mapped, we based our estimates of selection on the number of segregating missense variants in each gene per primate species (i.e., we excluded variants that were carried on all chromosomes sampled from a given species). This ensures that we do not underestimate selection in the primate samples, because fixed variants are more neutral than segregating variants. Nonetheless, the number of segregating missense variants is shaped in complex ways by both sampling and demographic forces, we took a two-pronged approach to tackling this question. First, we built an explicit population genetic model to model selection across primates. Second, we developed a Poisson Generalized Linear Model to robustly detect genes that are differentially selected between humans and primates.

Explicit population genetic model of selection

Our explicit population genetic model proceeds through two phases: first, we model the counts of synonymous segregating sites to learn a neutral background distribution of mutation rates per gene per species. Then, we apply that neutral background distribution to estimate the average selection per gene across species.

General modelling framework

We first established a neutral baseline for each species by fitting a model to the segregating synonymous variants in each species. We employed the Poisson Random Field model, under which the observed number of segregating sites is a Poisson random variable, with the mean determined by mutation, demography, selection, and sample size (*34*). For simplicity, we assumed an equilibrium (i.e. constant) demography for all species besides human; for human, we used Moments (*51*) to find a best fitting demographic history based on the folded site frequency spectrum of synonymous sites.

With a best fitting demographic model in hand, we let X_{igk} be the number of mutations of type k ($k = 0$ is synonymous, $k = 1$ is missense) in gene g of species i, $\theta_{ig} = 4N_i\mu_g$ be the per site population scaled mutation rate, and L_{gk} be the number of sites of type k in gene g. We then use dadi (*50*) to compute $p_i(\gamma_{ig})$ which can be interpreted by noting that $\theta_{ig}p_i(\gamma)$ is approximately the probability that a site in gene g with population scaled selection coefficient $\gamma_{ig} = 2N_i s_g$ is segregating in a sample from species i.

Then, the distribution of X_{ijk} is Poisson with mean $\theta_{ig}L_{gk}p_i(\gamma_{ig})$, i.e.

$$P\left(X_{igk} = x \middle| \theta_{ig}\right) = \frac{\left(\theta_{ig}L_{gk}p_i(\gamma_{ig})\right)^x}{x!} e^{-\theta_{ig}L_{gk}p_i(\gamma_{ig})}.$$

Background neutral model to estimate per gene mutation rates

We anticipated that due to a combination of true variation in mutation rate and data quality across the genome, different genes would have a different effective per base-pair mutation rate. Although we could have used the estimated mutation rates from earlier work, we wanted to create a robust estimate with very few parameters per species. To accommodate this, we adopted a Gamma distributed prior on θ_{ig}, and applied it to synonymous sites (i.e., $k = 0, \gamma_{ig} = 0$) and integrated over it to result in a scaled negative-binomial distribution.

$$P\left(X_{ig0} = x_0\right) = \int_0^\infty \left(\frac{\left(\theta_{ig} L_{g0} p_i(0)\right)^{x_0}}{x_0!} e^{-\theta_{ig} L_{g0} p_i(0)} \right) \left(\frac{\beta^\alpha}{\Gamma(\alpha)} {\theta_{ig}}^{\alpha-1} e^{-\beta\theta_{ig}} \right) d\theta_{ig}$$

$$= \frac{L_{g0} p_i(0)}{x_0!} \frac{\beta^\alpha}{\Gamma(\alpha)} \frac{\Gamma(\alpha + x)}{\left(\beta + L_{g0} p_i(0)\right)^{\alpha+x_0}}$$

To account for the impact of GC content on mutation rate, we parameterized the gamma distribution mean as a log-linear function of GC content,

$$log\left(\mu_g\right) = m_0 + m_{GC} GC_g,$$

$$log(\sigma) = sd_0.$$

from which we can compute gene-specific α and β parameters,

$$\alpha_g = \frac{\mu_g^2}{\sigma^2}$$

$$\beta_g = \frac{\mu_g}{\sigma^2}.$$

We then optimized the parameters m_0, m_{GC}, and sd_0 by maximum likelihood in each species to learn the background distribution of mutation rates.

Given our optimized parameters, we can compute a posterior distribution on the mutation rate per gene,

$$P\left(\theta_{ig} \middle| X_{ig0} = x_0\right) = \frac{\left(\beta_g + L_{g0} p_i(0)\right)^{\alpha_g + x_0}}{\Gamma(\alpha + x_0)} \theta_{ig}^{\alpha_g + x_0 - 1} e^{-\left(\beta_g + L_{g0} p_i(0)\right)\theta_{ig}}$$

which is simply a gamma distribution with parameters ${\alpha_g}' = \alpha_g + x_0$ and ${\beta_g}' = \beta_g + L_{g0} p_{i(0)}$.

Fig. S7A shows a histogram of the average population scaled mutation rate across species.

Modelling selection across species

With the parameters m_0, m_{GC}, and sd_0 in hand, we can parameterize the distribution of the number of segregating nonsynonymous sites given a selection coefficient. To generate the expected number of segregating sites given a selection coefficient, we used dadi (*50*) to generate $p_i(\gamma)$ across a grid of population scaled selection coefficients, from 2Ns = 0 to 2Ns = 10000. We assumed further that every nonsynonymous mutation in a gene shares the same population scaled selection coefficient, γ_{ig}.

We then took the posterior distribution of θ_{ig} estimated from the synonymous sites as the distribution of mutation rates for nonsynonymous sites to obtain

$$
\begin{aligned}
&\mathrm{P}\left(\mathrm{X}_{\mathrm{ig1}} = \mathrm{x}_1 \middle| \gamma_{ig}\right) \\
&= \int_0^\infty \left(\frac{\left(\theta_{ig} L_{g1} p_i\left(\gamma_{ig}\right)\right)^{x_1}}{x_1!} e^{-\theta_{ig} L_{g1} p_i\left(\gamma_{ig}\right)} \right) \left(\frac{\left(\beta_g + L_{g0} p_i(0)\right)^{\alpha_g + x_0}}{\Gamma(\alpha + x_0)} \theta_{ig}^{\alpha_g + x_0 - 1} e^{-\left(\beta_g + L_{g0} p_i(0)\right)\theta_{ig}} \right) d\theta_{ig} \\
&= \frac{L_{g1} p_i\left(\gamma_{ig}\right)}{x_1!} \frac{\left(\beta_g + L_{g1} p_i(0)\right)^{\alpha + x_0}}{\Gamma(\alpha + x_0)} \frac{\Gamma\left(\alpha_g + x_0 + x_1\right)}{\left(\beta_g + L_{g0} p_i(0) + L_{g1} p_i\left(\gamma_{ig}\right)\right)^{\alpha_g + x_0 + x_1}}.
\end{aligned}
$$

Finding average selection coefficients via an EM-like procedure

Noting that from population genomic data, the only thing that can be explicitly determined is the population-scaled selection coefficient, $\gamma_{\mathrm{ig}} = 2N_i s_{ig}$, we devised a two-step procedure to control for demographic differences across species (i.e., differences in N_i). In principle γ_{ig} can be different across species due to differences in either N_i or s_{ig}, but we assumed that for the majority of genes, $s_{ig} \equiv s_g$ is identical across species, and the differences in γ_{ig} are driven primarily by differences in N_i . Our procedure can then be thought of as analogous to an EM algorithm, in which first we estimate γ_{ig} separately for each species and gene, followed by estimating N_i by assuming that s_{ig} is identical across species, and finally using our estimated N_i to produce estimates of s_g.

First, we inferred γ_{ig} for each gene and species separately. This resulted in some information loss, because in species with small sample sizes, there may be many genes with 0 segregating missense variants, and hence result in an inference of an MLE $\gamma_{\mathrm{ig}} = -\infty$. Nonetheless, for each species we obtained thousands of genes with an estimate of γ_{ig}. To control for some variation in estimated γ across species, we additionally restricted to genes with γ_{ig} between 10 and 1000.

We then assumed that for almost all remaining genes (1000-10000 depending on the species), the difference in estimated $\gamma_{\mathrm{ig}} = 2N_i s_{ig}$ between species is due to the N_i being different, and that $s_{ig} \equiv s_g$ is identical across species for gene g. For each gene, we averaged estimated γ_{ig} across species to obtain $\overline{\gamma_g} \approx 2\overline{N} s_g$, the average population scaled selection coefficient for gene g. Then, we computed $R_{ig} = \gamma_{ig}/\overline{\gamma_g}$, which is an estimator of $N_i/\overline{N}$ because $\gamma_{ig}/\overline{\gamma_g} \approx 2N_i s_g/2\overline{N} s_g = N_i/\overline{N}$. To account for noise among the outliers and the fact that s_g is not truly identical across species, we estimated a single R_i value per species by taking the median of R_{ig} across all genes in species i.

Finally, we grouped species together to re-estimate $\overline{\gamma}_{\mathrm{g}}$ by substituting $\gamma_{\mathrm{ig}} \rightarrow R_i \overline{\gamma}_{\mathrm{g}}$, which provides an approximation of γ_{ig} from $\overline{\gamma_g}$ via $R_i \overline{\gamma}_{\mathrm{g}} \approx \mathrm{N_i}/\overline{\mathrm{N}} 2\overline{\mathrm{N}} \mathrm{s_g} = 2\mathrm{N_i s_g}$. Then, we maximized the likelihood

$$L\left(\overline{\gamma}_{\mathrm{g}}\right) = \prod_{\mathrm{i} \in \mathrm{I}} \mathrm{P}\left(\mathrm{X}_{\mathrm{ig1}} \middle| \mathrm{R_i} \overline{\gamma}_{\mathrm{g}}\right)$$

to find the maximum likelihood estimate of $\overline{\gamma_g}$ across a group of species I. In the following, we take I to be either the set P of all non-human primates, or I to be the singleton set H containing just humans.

Fig. S7B shows our estimated $\overline{\gamma_g}$ as a function of the pooled missense : synonymous ratio among primates. The strong negative correlation is expected, as genes with higher missense : synonymous ratios have smaller estimated selection. To convert our estimates of $\overline{\gamma_g}$ to estimates of the selection coefficient, s, we divided by 2*10,000, which we take to be a typical effective population size among primates.

Comparing human and primate selection

Next, we compared human and primate constraint using this modelling approach. First, we computed a distribution of fitness effects (DFE) across genes in humans and primates by plotting a histogram of selection coefficients per gene in both our grouping of primates and our human data (Fig. S7C). We note that the much larger sample size of the human data compared to the primate data results in fewer outliers of strong selection, because almost every gene has missense variants in the human data, whereas in the primate data there are many genes observed with few to no primate missense variants.

To identify genes where human constraint is different from non-human primate selection, we developed a likelihood ratio test to test whether s is significantly different between human and other primates by testing if $\overline{\gamma_g}$ is different between human and primate. Under the null model, $\gamma_{gh} = \overline{\gamma_g}$, so the likelihood is

$$\mathrm{L}_1(\overline{\gamma}_\mathrm{g}) = \left(\prod_{i\in P} P(X_{ig1}; R_i\overline{\gamma}_\mathrm{g})\right) \times P(X_h g1; R_h\overline{\gamma}_\mathrm{g})$$

where P is the set of non-human primates and the subscript h indicates human data. Under the alternative hypothesis, $\gamma_{hg} \neq \overline{\gamma_g}$ so the likelihood is

$$\mathrm{L}_2(\overline{\gamma}_\mathrm{g}, \gamma_{hg}) = \left(\prod_{i\in P} P(X_i; R_i\overline{\gamma}_\mathrm{g})\right) \times P(X_h; R_h\gamma_\mathrm{hg}).$$

This then forms the likelihood ratio test statistic,

$$\Lambda = 2(\log L_2 - \log L_1).$$

Note that under the null hypothesis $\gamma_{hg} = \overline{\gamma_g}$ we have that $L_1 = L_2$ and hence this represents a nested hypothesis test. Thus, under the null hypothesis that $\gamma_h = \overline{\gamma}$, the test statistic follows a χ^2 distribution with one degree of freedom, $\Lambda \sim \chi^2(df = 1)$, by standard likelihood ratio theory.

Intuitively, this test determines whether s_{hg} is significantly different from s_g, because we already corrected for the effective population size of humans using R_h. Specifically, $R_h\gamma_{hg} \approx N_h/\overline{N}2\overline{N}s_{hg} = 2N_h s_{hg}$ while $R_h\overline{\gamma_g} \approx N_h/\overline{N}2\overline{N}s_g = 2N_h s_g$, so that if $\gamma_{hg} \neq \overline{\gamma_g}$, then $s_{hg} \neq s_g$.

Fig. S7D shows the relationship between $\overline{\gamma_g}$ and γ_{hg}, showing that there is a strong correlation. Colored points indicate genes that are significant according to the combined significance test described in the main text and subsequently.

Comparison with alternative approaches

We next assessed whether our population genetic modeling improved the correlation of selection estimates of our primate data with previous gene-constraint metrics in humans, including pLI (*28*) and s_het (*111*). We found that explicitly modeling the selection coefficient improves the correlation with these constraint metrics over the raw missense : synonymous ratio when using either primate data or human data (Fig. S8).

Testing the model via simulation

To verify the performance of our model, we performed population genetic simulations.

We generated data in line with our human and primate data by simulating data for 15000 genes. We used the number of synonymous and nonsynonymous mutations possible given the human reference genome for each gene, to create a realistic distribution of polymorphism in our simulations. For each gene, we drew the selection coefficient from a gamma distribution with mean 0.01 and standard deviation 0.01. We also drew the mutation rate per basepair for each gene from a gamma distribution with mean $5\text{x}10^{-8}$ and standard deviation $1\text{x}10^{-8}$. We then sampled from 213 species, with sample sizes matching those in our real primate data. For each species, we drew an effective population size from a gamma distribution with mean 10,000 and standard deviation 5,000.

To generate data for each species, we sampled from the Poisson random field model. Specifically, given an effective population size, mutation rate, sample size, and selection coefficient, the counts of sites from each gene in each species are sampled from a Poisson distribution as in the previous section. We then ran the inference pipeline inference on the simulated data, and Fig S9A shows that our inferred selection coefficients are very strongly correlated with the simulated selection coefficients, although they are somewhat upwardly biased for very weak selection of roughly $s \sim 1/10000$, which is expected based on the fact that the population scaled selection coefficient would be less than 1 on average, and thus have only minimal effects on segregating polymorphism. This shows that our model infers selection precisely from genome-scale data.

We then tested the power and calibration of the likelihood ratio test by simulating 2000 of the 15000 genes as having a different selection coefficient in humans compared to the rest of primates. To simulate the change in selection coefficient, we drew a random factor with a log-uniform distribution between 0.01 and 100 and multiplied the primate selection coefficient by that factor for each of the 2000 genes. We then performed the inference pipeline followed by the likelihood ratio test, with p-values corrected for multiple testing by the Benjamini-Hochberg procedure, as in the main text. Fig S9B shows that we obtain good control of the false discovery rate for genes with no change in selection between humans and primates, while obtaining greater power for larger shifts between human and primate.

Poisson generalized linear mixed model

Our population genetic model successfully modelled the similarity of selection between primates and humans, which we wanted to confirm with a less explicit model. To do so, we used a Poisson generalized linear mixed model (GLMM), inspired by the model used in SnIPRE (*131*). We pooled polymorphic synonymous and missense mutations across all primates, and compared the pooled MSR to the MSR of human variants. Because these two quantities are related in a non-linear way, we used a two-step process. First, we fit a Poisson GLMM to the pooled primate data to estimate the depletion of missense variation at each gene. Then, we fit a second Poisson GLMM to the human data, controlling for the primate depletion estimates. This allowed us to estimate how much more or less depleted for missense variation each human gene is compared to what is expected based on primate genes. To control for noisily estimated missense : synonymous ratios, we only fit the Poisson GLMM to genes that had an average unique mapper score > 0.9 across all primate species and for which we had at least 100 synonymous variants pooled across primates.

Primate GLMM

To model primate variation, we set up a simple model in which there is a background mutation rate and the impact of GC content as fixed effects, and random effects accounting for gene-specific mutation rates and the depletion of nonsynonymous variation. Recalling from the population genetic model that X_{igk} is the number of mutations of type k ($k = 0$ is synonymous, $k = 1$ is missense) in gene g of species i, we summed over all non-human primates to get the total number of variants of type k in gene g across non-human primates,

$$X_{gk}^{(P)} = \sum_{i \in P} X_{igk}$$

where P is the set of non-human primates, and the superscript (P) indicates that the value is over non-human primates and is not an exponent. Then, we modeled $X_{gk}^{(P)}$ as a Poisson GLMM,

$$X_{gk}^{(P)} \sim Poisson\left(\mu_{gk}^{(P)}\right)$$

where

$$log\left(\mu_{gk}\right) = \beta_0^{(P)} + \beta_1^{(\mathrm{P})}\mathrm{GC_g} + \delta_g^{(P)} + \epsilon_g \mathrm{k} + log\left(L_{gk}\right)$$

with $\beta_0^{(P)}$ being a fixed effect corresponding to background mutation rate, $\beta_1^{(P)}$ being a fixed effect that corresponds to the impact of GC content, $\delta_g^{(P)}$ a random effect corresponding to the discrepancy between the mutation rate of gene g and the genome-wide background, ϵ_g a random effect corresponding to the deficit of missense variation, *k* is an indicator of mutation type, and L_{gk} the number of sites of type k in gene g. Note that k here serves as an indicator of whether a site is a synonymous or a missense mutation.

We fit this model using the R package glmer (*52*).

Human GLMM

With the estimates of ϵ_g in hand, we built a model for the human data $X_{gk}^{(H)} \equiv X_{hgk}$, with

$$X_{gk}^{(H)} \sim Poisson\left(\mu_{gk}^{(H)}\right)$$

Where

$$log\left(\mu_{gk}^{(H)}\right) = \beta_0^{(H)} + \beta_1^{(H)} GC_g + \beta_2 \epsilon_g k + \beta_3 \epsilon_g^2 k + \beta_4 \epsilon_g^3 k + \delta_g^{(H)} + \eta_g k + log\left(L_{gk}\right)$$

Here, $\beta_1^{(H)}$, $\beta_2^{(H)}$, $\delta_g^{(H)}$, and L_{gk} have the same interpretation as the primate model, just applied to human data. However, we now have additional fixed effects β_2, β_3, and β_4 that model a nonlinear relationship between the missense depletion in primates and the missense depletion in humans. Thus, our remaining random effect, η_g can be thought of as the deviation of the observed depletion of missense variants in humans compared to what would be expected based on the primate depletion. In particular, $\eta_g < 0$ indicates that a gene has even fewer missense variants than would be expected based on primates, and is thus suggestive of stronger constraint in humans than in primates, while $\eta_g > 0$ indicates an excess of missense variants compared to expected based on primates, implying relaxed constraint in humans compared to primates.

To see if the model is able to capture the nonlinear relationship of human and primate MSR, Fig. S10 shows the log-scaled MSRs of both human and primate, along with the function $\beta_2 x + \beta_3 x^2 + \beta_4 x^3$ which models the relationship of primate MSR to human MSR. It is able to capture the nonlinearity near the edges of the MSR distribution much better than a linear fit.

GLMM p-values

To determine which η_g values were significantly different from 0, and hence indicative of human having less or more constraint than non-human primates, we developed an approach to controlling for gene length by binning genes by gene length and creating Z-scores based on the η_g within each bin. Intuitively, shorter genes are likely to have a large magnitude of η_g by chance. Moreover, because we don't actually expect that selection is identical between humans and primates, we anticipate identifying genes for which η_g significantly deviates from a background distribution.

Our procedure was to first bin genes into quantiles by the number of amino acids in the human reference genome, each bin consisting of 100 genes. We then computed a Z-score by bin by computing the mean and standard deviation of η_g within each bin and standardizing each η_g by bin-wise mean and standard deviation. We then computed p-values assuming that the Z-score follows the standard normal distribution $Z \sim N(0,1)$.

PrimateAI-3D Model

We developed a comprehensive deep learning algorithm called "PrimateAI-3D". It takes as input protein structures and fixed-species multiple sequence alignments. A method called voxelization captures the protein structure surrounding a target variant and the conservation of its amino acids across evolution. A 3D convolutional neural network takes this voxelized structure as input and converts it into predictions of pathogenicity. PrimateAI-3D is trained to integrate three diverse objectives: distinction between human and primate common variants and unknown human variants; prediction of acceptable alternative amino acids at a protein site after removing all atoms of the original amino acid ("fill-in-the-blank in 3D"); ranking of scores that follows the ranking produced by the PrimateAI language model and the variational autoencoder from EVE.

Training data preparation

Protein structures

We downloaded predicted human protein structures from the AlphaFold DB (June 2021) (*73*). 16,568 protein sequences in that database matched exactly to one of our 19,158 hg38 proteins. For the rest, we performed homology modelling: we created a BLAST (*132*) database from the sequences in AlphaFold DB and searched against it with the remaining 2,590 proteins. For 2,167 proteins, we found a sequence match with >80% sequence identity, >80% target sequence coverage and <75 residues not covered (for 1,073 of those 2,590 proteins, both sequence identity and target coverage were >99%). We applied homology modelling software Modeller (*116*) using the AlphaFold structures as templates to calculate structures that exactly matched the sequences of our target proteins. For the remaining 423 proteins with more than 75 residues not covered by an AlphaFold DB structure, we used HHpred (*74*) to predict a structure for the entire protein. Then we used both the AlphaFold DB and HHpred structures as templates in Modeller. This procedure covered another 384 proteins with structure, leaving 39 proteins that failed in HHpred or Modeller. All these 39 proteins were several thousand amino acids long and were excluded from our training dataset.

Multiple sequence alignments

PrimateAI-3D took in the multiz100 alignment from the UCSC database (*112, 113*) to calculate the evolutionary conservation of each human protein residue in a set of 100 vertebrate species, similar to PrimateAI (*17*). In addition, we also included the protein sequences derived from the recently released Zoonomia study which consists of whole-genome alignments of 241 mammalian species (*114*). Finally, we obtained alignments of 251 species that covered at least 75% of all human proteins in the human Jackhmmer alignments (*133*) that we generated to replicate EVE (*67*); section "Model evaluation"). We aligned the amino acid sequences of the three sets of species to produce an alignment of human proteome across 592 species by filling any missing parts with gaps.

Protein voxelization and voxel features generation

Protein voxelization is the process of converting sets of protein atomic coordinates into tensors that have the same shape for all sets of coordinates and that can then be used in a traditional machine learning device. A regular sized 3D grid of cubes ("voxels") is centered at the Cα atom of the residue with the target variant (Fig. S11) and each voxel captures its atomic and evolutionary environment. We evaluated different combinations of grid sizes of voxels and voxel sizes and selected a grid size of 7x7x7 voxels with a voxel size 2Åx2Åx2Å, which achieves the best performance.

For each voxel, we computed a vector composed of diverse features, which is explained in detail below.

Atomic distance profile

For each voxel, we recorded the shortest distance between the Cα of one type of residuals (e.g., Alanine residue in Fig. S11) and the center of the voxel. We repeated this procedure for other amino acids and obtained the shortest distance of the voxel center to each of 21 amino acid types (20 standard amino acids plus one amino acid representing all non-standard amino acids). We then recorded the shortest distance for Cβ instead of Cα atoms, resulting in 2*21=42 distance values for each voxel (Fig. S11), which is referred to as the atomic distance profile of a variant. Detailed procedure is explained in Supplementary Text section 1.

Structure quality features

Several features measure the confidence of the structure around each voxel, including an indicator whether the protein structure is present in AlphaFold DB as-is (i.e., with a perfect sequence match to one of our protein sequences) and an indicator whether we used Modeller with AlphaFold DB structures as templates (in case the match was not perfect). We also included residue-specific quality features such as the pLDDT from AlphaFold DB (Fig. S12).

Species-differentiable evolutionary profiles

In PrimateAI (*17*), the evolutionary profile of a target residue is the frequency of each amino acid in the multiz100 alignment. This implies that all species have the same contribution to the amino acid frequency profile, regardless of the genetic distance of a species to human or to other species, thus it is an unrealistic scenario. Therefore, in PrimateAI-3D, we assigned a different weight to each species of the 592-way whole proteome alignments. We initialized each weight to be 1/592 at the beginning of training, but let each weight be differentiable. This means PrimateAI-3D learns by itself how important each of the 592 species in the MSA is in terms of contribution to human pathogenicity. In Supplementary Text section 3, we implemented this procedure in a convolutional layer $Conv_f$ that, for any target residue, takes a fixed-species multiple sequence alignment as input and outputs an evolutionary profile with 210 features. In order to merge this evolutionary profile with voxels, we obtained a mapping from each voxel to the sequence position of the residue that is closest to the voxel center across all protein atoms in the structure (the nearest neighbor; function defined in Supplementary Text; Fig. S12).

Other protein-specific features

We included the reference amino acid in every voxel as a 1-hot encoded vector with 21 features (Fig. S12). The reference amino acid is the amino acid at the target site in the human reference proteome. Furthermore, we added two binary indicators to every voxel that signal whether the atoms of the target residue had been removed before voxelization or not (section "Model training"; Supplementary Text for details).

Model Architecture

The first layer of the network performs unpadded 3D convolutions in the voxel feature dimension with a kernel size of 1x1x1 and 128 filters, followed by ReLU activation and batch normalization. This creates an output tensor of shape 7x7x7x128. We then repeatedly applied 3D convolutions with a kernel size of 3x3x3, valid padding, and 64 filters until the output tensor's shape becomes 1x1x1x64, again each time followed by ReLU activation and batch normalization. In each such layer, the first three dimensions of the output are reduced by 2 (because of the valid padding). Then we flattened the tensor and added a final hidden dense layer with 64 hidden units (ReLU activation, batch normalization). The output layer consists of 20 units (one for each standard amino acid) and uses a sigmoid activation function.

Model training

PrimateAI-3D was trained to perform multiple tasks simultaneously (multi-task learning), which are described in detail below. Each task captures an alternative and unique aspect of pathogenicity. We experimented with multiple combination techniques, including transfer learning, but found that simultaneous optimization gives the best generalization performance, which is in line with the current trend in structure prediction models (e.g., AlphaFold2 (*72*) and RoseTTAFold (*134*) to combine various evolutionary and physical aspects of predicted structures in their loss functions).

Human and primate variants

We obtained 4.5 million benign missense variants from human and primate data. We sampled a matched set randomly from the genome, requiring the distribution of mutational probabilities of unknown variants to be identical to that of benign variants. Another difference from PrimateAI (*17*) was that we used a single label vector to represent all the variants at the same amino acid site. This means we predicted the pathogenicity of all alternative amino acids at a site in one forward pass, instead of only a single variant. Note that a single nucleotide substitution cannot generate all 20 amino acids and that the label vector for a residue always contains missing values. We therefore masked missing labels during loss calculations so that they never directly contribut to the gradient. Benign variants have a label value 0 and pathogenic variants have a value 1. We used mean squared error as the loss function for non-missing labels.

Variants from fill-in-the-blank in 3D

The generation of this variant set was inspired by the typical training procedure of language models (*81*). During voxelization, the voxel grid is centered on the Cα atom of a target residue and the distance profile is calculated using all atoms within the scanning radius of a voxel center. For fill-in-the-blank in 3D, we performed the same procedure, except that we removed all atoms of the target residue before calculating the distance profile or nearest neighbor mapping. In effect, all features specific to the target residue were removed from the input tensor to the network. Then we trained the network to pick the amino acid which may be acceptable at the target site. These acceptable / unacceptable amino acids from the multiple sequence alignments formed a second training set. Any amino acid that occurs in the MSA at the target site was considered acceptable (label 0), all others unacceptable (label 1).

Variant ranks from language models

Language models, such as EVE and PrimateAI language model, perform competitively on data sets evaluated on a per-gene basis, such as saturation mutagenesis assays. However, directly using prediction scores from these models as additional features to PrimateAI-3D failed to improve performance. This is due to that the major fraction of the variance in variant pathogenicity across the human proteome can be attributed to the variation of proteins or protein domains. For example, in the human and primate variant set, the ratios between the numbers of common and unknown variants are lower for more pathogenic genes. Similarly, in fill-in-the-blank training, we observed fewer species tend to carry mutations in more pathogenic genes, assuming a fixed set of species across the proteome. Language model scores, however, have not been calibrated well for this inter-protein (or protein domain) variation, thus are ignored by gradients from the previous two datasets with dominant effect on variance. Instead, we hypothesized that using language model scores as an additional target output could be helpful: first, neither of the two datasets capture epistatic patterns (unknown human variants can contain both pathogenic and benign variants; fill-in-the-blank labels are taken only from single protein positions in limited species without considering sequence context). Secondly, voxelized structures may be expressive enough to capture epistatic patterns by themselves. For example, epistatic interactions usually indicate residue-residue interactions in structure (*135*).

We used a rank loss function to incorporate language model scores as a third training dataset, and only computed it on variants from the same protein. More specifically, we first converted the scores from language models to ranks, separately for each protein. This means the ranks for each protein are within range (1,…,N), where N is the length of the protein. These ranks are the truth ranks, i.e. PrimateAI-3D is trained to produce scores that have the same ranks. The pairwise logistic loss from Pasumarthi *et al.*(*117*) measures the distance between two sets of ranks and produces a gradient that ultimately updates the model to predict scores that better match the truth ranks.

Training procedure

The dataset of human and primate variants covers 5.6M of 10.8M possible amino acid positions in human proteome. For each of the other two datasets (fill-in-the-blank in 3D and language model ranks), we sampled equally as many amino acid positions. This is primarily due to practical reasons. First, this allows each batch to have the same number of samples from each dataset (~33 with a batch size of 100), leading to more stable training in each dataset individually. Second, it controls the influence of each dataset solely via the sample weight in the loss function, instead of training sample size as an additional free parameter. Third, it keeps training and epoch times at reasonable levels. Last, there was no obvious performance benefit from allowing more samples.

For the language model ranks dataset, we additionally required that all 33 samples in a batch come from the same protein. This allows calculating rank losses not only for the same protein position, but across all samples from the same batch. The number of times that a protein was chosen for a batch was proportional to the length of the protein. In order to make our model robust against protein orientations, we randomly rotated the protein atomic coordinates in 3D before voxelizing a variant.

Model optimization was performed using Adam (*136*) from Keras 2.2.0 with default parameters and a learning rate of 0.001. From each of the three datasets, we sampled 20,000 hold-out protein positions for model validation. For each alternative model and epoch, we predicted these hold-out validation datasets, together with variants from *BRCA1* and *TP53* assays. This produced two area under ROC (AUC) metrics (human and primate variants and fill-in-the-blank in 3D variants) and three Spearman rank correlation values (language model ranks and *BRCA1* and *TP53* assay ranks) for each epoch in each alternative model. We calculated the rank of each metric across all alternative models, e.g., we converted human and primate AUC values from 9 alternative models in a range (0.6, …, 1.0) to ranks (1, …, 9). Then, for each model, we averaged the ranks of the 5 datasets, and only kept the model with the highest average rank. Furthermore, we used this procedure to optimize the weights of each dataset in the loss function (0.5 for fill-in-the-blank in 3D, 1.0 for language model ranks, 2.0 for human and primate variants).

Ensemble training and inference

Once we found the optimal model and model parameters, we repeated this training procedure 40 times, each time with a different initial seed value. This generated 40 different models. In order to predict a variant, we calculated its pathogenicity score using all 40 models 10 times, each time with a different protein orientation. The average of these 400 scores was the final pathogenicity score for the variant.

PrimateAI Language Model

PrimateAI language model (PrimateAI LM) is a multi-sequence alignment (MSA) transformer (*83*) for fill-in-the-blank residue classification, which was trained end-to-end on MSAs of UniRef-50 proteins (*118, 119*) to minimize an unsupervised masked language modelling (MLM) objective (*81*). It outputs classification scores for alternative and reference residues, which serve as inputs to the PrimateAI-3D rank loss.

Traditionally, fill-in-the-blank MSA transformers simultaneously classify multiple masked locations in MSAs during training. Higher numbers of mask locations can add more MLM gradients that inform optimization, thereby enabling a higher learning rate and faster training. However, fill-in-the-blank pathogenicity prediction is fundamentally different from traditional MLM as classification at a mask location depends on predicted values of residues at other mask locations. The classification scores may often be the averages of conditional predictions over all possible combinations of residues at other mask locations. PrimateAI LM avoids this averaging by revealing tokens at other mask locations before making predictions. Our model achieves state-of-the-art clinical performance and denoising accuracy whilst requiring 50x less computation for training than previous MSA transformers.

Preparation of MSA datasets

We created an MSA for each sequence in a UniRef-50 database (March 2018 version) (*115, 118*) by searching a UniClust30 (*137*) database (October 2017 version). Then an MSA dataset containing 26 million MSAs was created using the protein homology detection software HHblits version 3.1.0 (*138*). Default settings were used for HHblits except that we set the number of search iterations (-n) to 3. This replicates the approach to generating MSAs to train MSA transformer (*139*). In addition, we generated a set of MSAs for 19,071 human proteins using HHblits following the procedure above.

Next, we excluded UniRef-50 MSAs whose query sequences carry rare amino acids, retaining those containing the 20 most abundant residues only. To further simplify our data pipeline, we filtered non-query sequences in the MSA to those that only contain the 20 most common residues and gaps, which represent deletions relative to the query sequence. As input MSAs to PrimateAI LM have a fixed size of 1024 sequences, we randomly sampled up to 1023 non-query sequences from the filtered sequences if MSA depth is larger than 1024. If MSA depth is below 1024, we padded the MSA with zeros to fill the input.

We then applied a periodic mask pattern with a stride of 16, which covers an amino acid position of interest in the query sequence, to MSAs. Using a fixed mask pattern ensures consistent computational requirements for mask revelation discussed below. The position of interest was randomly sampled from all positions in the query sequence during training or chosen by a user during inference. To maximize information about the position of interest, we tried to select a cropping window with a size of 256 residues where the position of interest is at the center. However, the cropping window may be shifted if the position of interest is near the edge of an MSA to avoid padding zeros and increase information about the position of interest. If the query sequence is shorter than the PrimateAI LM cropping window, zeros were padded to fill the window size. Illustration of cropping, masking, and padding of MSAs input to PrimateAI LM is shown in Fig. S23.

We followed AlphaFold 2 (*72*) to assign a smaller probability, p_{sample}, to an MSA being sampled during training if the protein length, L, is shorter,

$$p_{\text{sample}} \propto \frac{\max(\min(L, 512), 64)}{512},$$

to rebalance the distribution of lengths for UniRef-50 proteins used for training and human proteins, and to avoid computation being wasted on padding. We also adjusted the probability of sampling non-query sequences to be included in the first 32 sequences of an MSA, where the fixed mask pattern is applied, to penalize the occurrences of gaps in those sequences. The probability, p_{mask}, of a non-query sequence being masked decreases with increasing number of gap tokens, N_{gap},

$$p_{\text{mask}} \propto \frac{\left(L - N_{\text{gap}}\right)^2}{L^2}.$$

Down sampling of sequences with lots of gaps reduces the fraction of missing data in MSAs.

Model Architecture

MSA Embedding

We first embedded MSA input for PrimateAI LM, shown in Fig. S24, and applied a fixed mask pattern to the first 32 sequences of MSAs. The MSA tokens were encoded by learned 96-channel embeddings, which were summed with learned 96-channel position embeddings for residue columns before layer normalization (*140*). To reduce computational requirements, embeddings for the 1024 sequences in MSAs were split into 32 chunks, each containing 32 sequences, at periodic intervals along the sequence axis. These chunks were then concatenated in the channel dimension and mixed by linear projection.

MSA Transformer

Embedded MSAs were propagated through 12 axial attention blocks shown in Fig. S13. Each axial attention block consists of residuals that add tied row-wise gated self-attention, column-wise gated self-attention, and a transition layer, shown in Fig. S13. The self-attention layer has 12 heads, each with 64 channels, totaling 768 channels, and transition layers project up to 3,072 channels for GELU activation (*141*). The adoption of axial gated self-attention was inspired by AlphaFold 2's Evoformer (*72*). The main change is that we used tied attention (*139*) in PrimateAI LM axial attention layer, instead of triangle attention in AlphaFold 2. Tied attention is the sum of dot-product affinities, between keys and values, across non-padding rows, followed by division by the square root of the number of non-padding rows, which reduces computational burden substantially.

Mask Revelation

Mask revelation, shown in Fig. S26, reveals unknown values at other mask locations after the first 12 axial attention blocks. It combines the updated 768-channel MSA representation with 96-channel target token embeddings at locations indicated by a Boolean mask which labels positions of mask tokens. The Boolean mask, which is a fixed mask pattern with stride 16, is applied row-wise to gather features from the MSA representation and target token embedding at mask token locations. Feature gathering reduces row length from 256 to 16, which drastically decreases the computational cost of attention blocks that follow mask revelation in Fig. S26. For each location in each row of the gathered MSA representation, we concatenated the row with a corresponding row from the gathered target token embedding where that location is also masked in the target token embedding. The MSA representation and partially revealed target embedding are concatenated in the channel dimension and mixed by linear projection.

After mask revelation, the now-informed MSA representation is propagated though residual row-wise gated self-attention and transition layers shown in Fig. S13. The attention is only applied to features at mask locations as residues are known for other positions from the MSA input to PrimateAI LM. Thus, attention only needs to be applied at mask locations where there is new information from mask revelation. After interpretation of the mask revelations by self-attention, a masked gather operation collects features from the resulting MSA representation at positions where target token embeddings remained masked. The gathered MSA representation is translated to predictions for 21 candidates in the amino acid and gap token vocabulary by an output head shown in Fig. S27.

Model Training

Loss Function

PrimateAI LM was trained end-to-end on MSAs for UniRef-50 proteins to minimize a weighted masked language modelling loss,

$$L_{MLM} = -w_{\text{length}} w_{\text{mask}} \sum_{i,j \in M} \log(\mathrm{p}_{ij})$$

where M is the set of positions where MSA input tokens are masked, and probabilities, p_{ij}, are computed from PrimateAI LM outputs by softmax normalization, $p_{ij} = s\text{oftmax}(l_{ij})$, of logits, l_{ij}, output by PrimateAI LM. Softmax normalization over the amino acid vocabulary is applied independently per position, j, in each sequence, i. Since query sequences do not contain gap tokens, query sequence gap token logit values are changed to -10^5. Loss weights are higher for longer proteins, thus we designed this weight,

$$w_{\text{length}} = \min\left(L^{\frac{1}{2}}, 64\right),$$

to adjust for the effect of a small portion of longer proteins when taking a single fixed-sized crop from their MSAs. Weights are also higher for MSAs with a lower number of masked positions, N_{mask},

$$w_{\text{mask}} = N_{\text{mask}}^{-\frac{1}{2}},$$

to rebalance contributions from MSAs with various depths and padding.

Optimizer

PrimateAI LM was trained for four days on four A100 graphical processing units (GPUs). Optimizer steps are for a batch size of 80 MSAs, which is split over four gradient aggregations to fit batches into 40 GB of A100 memory. PrimateAI LM was trained with the LAMB optimizer (*82*) using the following parameters: $\beta_1 = 0.9$, $\beta_2 = 0.999$, $\epsilon = 10^{-6}$, and weight decay of 0.01. Gradients are pre-normalized by division by their global L2 norm before applying the LAMB optimizer. Training was regularized by dropout (*142*) with probability 0.1, which was applied after activation and before residual connections, as shown in Fig. S25. Axial dropout (*72*) was applied in self-attention before residual connections: post-softmax spatial gating in column-wise attention is followed by column-wise dropout, and post-softmax spatial gating in row-wise attention is followed by row-wise dropout.

PrimateAI LM was trained for 100,000 parameter updates. The learning rate is linearly increased over the first 5,000 steps from $\eta = 5 \times 10^{-6}$ to a peak value of $\eta = 5 \times 10^{-4}$, and then linearly decayed to $\eta = 10^{-4}$. We applied automatic mixed precision (AMP) to cast suitable operations from 32-bit to 16-bit precision during training and inference (*143*), which increases throughput and reduces memory consumption without affecting performance. In addition, we used a Zero Redundancy Optimizer to reduce memory usage by distributing optimizer states across multiple GPUs (*144*).

Ensemble

An ensemble of six PrimateAI LM networks was trained with different random seeds for training data sampling and model parameter initialization. Their top-1 accuracies during training are shown in Fig. S28 for mask locations in the query sequence and all sequences in UniRef-50 MSAs. Top-1 accuracy for the query sequence is much lower than for all sequences as the query sequence does not contain gap tokens, which are easier to predict than residues as they often form long and contiguous segments in MSAs created with HHblits. PrimateAI LM accuracy on query sequences was steadily improving at the end of training. However, PrimateAI LM was trained for no more than 10^5 iterations due to computational cost.

Inference and pathogenicity score

PrimateAI LM fill-in-the-blank predictions are provided for locations of interest at every site in 19,071 human proteins, totaling predictions for 2,057,437,040 variants at 108,286,160 positions. Each prediction is made by our ensemble of six models, with each model contributing at least four inferences with different random seeds for sampling and ordering of sequences in human MSAs. Inferences logits were averaged by taking means of predictions grouped by random seed, and then taking the mean of the means. Each inference for 19,071 human proteins takes nearly 7 days on an A100 and, in total, inference by the ensemble takes nearly 200 A100 days.

Pathogenicity prediction of a variant is traditionally evaluated according to the relative logit of the variant residue compared to the one of the reference amino acid, i.e., $\log(p_{alt}) - \log(p_{ref})$, where p_{ref} and p_{alt} are the reference (ref) and alternative (alt) probabilities obtained from the ensembled logits. The probabilities are normalized over all possible residues disregarding the gap token, such that $\sum_r p_r = 1$ with probability p_r of the r^th^ residue obtained from the ensembled logits. The log difference captures how unlikely the variant amino acid is compared to the reference amino acid. However, the score does not consider the prediction of the other 18 possible amino acids, which contain information about the language models internal estimate of protein site conservation as well as convergence of the language model. We used the entropy evaluated over amino acid predictions $S = -\sum_r p_r \log(p_r)$ with probability p_r of the r^th^ residue to capture a variant agnostic site-dependent contribution to the pathogenicity score. Specifically, a score, s_{alt}, for residue alt at a given site is given by the usual log difference of the alt and reference ref logit at that site minus the entropy over amino acids at the given site, i.e.

$$s_{alt} = \log(p_{alt}) - \log(p_{ref}) - S.$$

The entropy term is small whenever the probability over all amino acids is dominated by a single term and large whenever the model is uncertain about the residues and assigns multiple residues high values. Physically, in this case the site is associated with little conservation and likely to mutate. This should lead to less pathogenic signal. Adjusting the scores by entropy incorporates a model internal estimate of amino acid conservation. A given log difference between residue and reference will be considered as more pathogenic whenever it is associated with a highly conserved site. The score adjustment additionally incorporates the lack of convergence associated with a heavily undertrained model.

Model Evaluation

Evaluation datasets

Saturation mutagenesis assays

We compared model performance using deep mutational scanning assays for the following 9 genes: amyloid-beta (*102*), *YAP1 (96), MSH2 (120), SYUA (101), VKOR1 (121), PTEN (99, 100), BRCA1 (122), TP53 (123),* and *ADRB2* (*124*). We excluded from the evaluation analysis a few assays of the genes for which the predication scores of some classifiers are unavailable, including *TPMT (99), RASH (145), CALM1 (146), UBE2I (146), SUMO1 (146), TPK1 (146),* and *MAPK1* (*147*). We also excluded assays of *KRAS* (*148*) (due to different transcript sequence), *SLCO1B1* (*149*) (only 137 variants), and amyloid-beta (*150*) (duplicate of (*102*)). We evaluated model performance by computing the absolute Spearman rank correlation between model prediction scores and assay scores individually for each assay and then taking the mean across all assays. See Table S6 for per-assay rank correlations for each method.

UK Biobank

The UK Biobank dataset (*79, 80*) contains 61 phenotypes across 100 genes. Evaluating on common variants of all methods reduces the number to 41 phenotypes across 42 genes. We calculated the absolute Spearman rank correlation between the predicted pathogenicity scores and the quantitative phenotype scores for each pair of gene/phenotype. Only gene/phenotype pairs with at least 10 variants were included in the evaluation (14 phenotypes across 16 genes). We also confirmed that our evaluation is robust to this choice of threshold.

ClinVar

We benchmarked model performance in classifying clinical labels of ClinVar (downloaded from https://ftp.ncbi.nlm.nih.gov/pub/clinvar/tab_delimited/variant_summary.txt.gz on September 19, 2021) missense variants (*4*) as benign or pathogenic. Both “benign” and “likely benign” labelled variants were considered benign, the same for “pathogenic” and “likely pathogenic” labelled variants (both considered pathogenic). To ensure high-quality labels, we followed (*67*) and only included ClinVar variants with 1-star review status or above (including “criteria provided, single submitter”, "criteria provided, multiple submitters, no conflicts", "reviewed by expert panel", "practice guideline"). This reduced the number of variants from 36,705 to 22,165 for the pathogenic and from 41,986 to 39,560 for the benign class. Following EVE (*67*), we calculated the area under the receiver operating characteristic curve for each gene and then report the mean AUC across all genes.

DDD / ASD / CHD de novo missense variants

To evaluate the performance of the deep learning network in clinical settings, we obtained de novo mutations from published studies for intellectual disorders, including autism spectrum disorder (*88-94*) and developmental disorders (*85-87*). ASD contained 2,127 patients with at least one de novo missense mutation. Taken together, there were a total of 3,135 DNM mutations. This reduced to 517 patients with at least one DNM variant and a total of 808 DNM variants after requiring all methods had predictions for those variants. In DDD, 17,952 patients had at least one de novo missense variant (26,880 variants in total), reducing to 6,648 variants after requiring availability of predictions of all methods. We also obtained a set of DNM variants from patients with congenital heart disorders (*95*), consisting of 1,839 de novo missense variants from 1,342 patients (reducing to 564 variants after requiring availability of predictions of all methods). For all the three datasets of de novo variants from affected patients, we used a shared set of DNM variants from healthy controls, which contains 1,823 DNM variants from 1,215 healthy controls with at least one DNM variant and collected from multiple studies (*88-93*). It was reduced to 250 variants (235 patients) after requiring availability of variant prediction scores of all methods. For each disease set of DNMs, we applied Mann-Whitney U test to evaluate how well each classifier can distinguish the DNM set of patients from that of controls.

Methods for comparison

Predictions from other methods were evaluated using rank scores downloaded from the database for functional prediction dbNSFP4.2a (*84*). To avoid dramatic reductions in the number of common variants, we removed methods with incomplete sets of scores (methods with less than 67 out of 71 million possible missense variants in hg38), except Polyphen2 (*151*) due to its widespread adoption. We included the following methods (method abbreviation) for comparison: BayesDel_noAF (BayesDel) (*152*), CADD_raw (CADD) (*153*), DANN (*154*), DEOGEN2 (*155*), LIST-S2 (*156*), M-CAP (*157*), MutationTaster_converted (MutationTaster) (*158*), PROVEAN_converted (PROVEAN) (*159*), Polyphen2_HVAR (Polyphen2; due to better performance then Polyphen2 HDIV) (*151*), PrimateAI (*17*), Revel (REVEL) (*160*), SIFT_converted (SIFT) (*161*), VEST4 (*162*), fathmm-MKL_coding (fathmm-MKL; highest performance among the fathmm models for given benchmarks) (*163*).

ESM1v model (*164*) was not released as part of dbNSFP4.2a (*84*). Due to unavailability of full mutation effect predictions of the human proteome for this model, we used the pre-trained ESM1v weights downloaded from GitHub (https://github.com/facebookresearch/esm) and evaluated on all human protein sequences using the published code without any modifications.

Applying EVE to more proteins

In the original publication, EVE (*67*) is only applied to a small set of disease-associated genes in ClinVar. To generate our language model-based training data set, it is essential to expand the predictions of EVE to as many proteins as possible. Due to unavailability of EVE source code, we therefore applied a similar method DeepSequence (*165*) and converted DeepSequence scores into EVE scores by fitting Gaussian mixture models. We used an up-to-date version of UniRef100 (*115*), but otherwise followed the alignment depth and sequence coverage filtering steps described in (*67*). We achieved at least 1 prediction in 18,920 proteins and a total of 50.2M predicted variants out of 71.2M possible missense variants. To validate our replication, we evaluated the replicated EVE models using published variants from (*67*). We found that scores from the replicated EVE model results in comparable performance to the published EVE software on all benchmarking datasets, e.g., both methods achieve 0.41 mean absolute correlation on Assays and 0.22 mean absolute correlation for UKBB.

Benchmarking PrimateAI LM against other sequence-only models for pathogenicity predictions

PrimateAI LM falls into a class of methods only trained to model proteins sequences but performing surprisingly well as pathogenicity predictors. Despite not achieving the overall best performance by themselves, they make crucial features or components in classifiers incorporating more diverse data. Fig. S14 summarizes the evaluation performance of the PrimateAI LM against other such sequence-only methods for pathogenicity prediction: ESM1v (*164*), EVE (*67*), LIST-S2 (*42)*, and SIFT (*48)*. Our language model outperforms another language model ESM1v on all the testing datasets except assays using only 1/50th of the training time. This is particularly striking as PrimateAI LM does not rely on any fine-tuning on assays.

Combining PrimateAI LM with EVE

Language models are trained to model the entire universe of proteins. EVE (*67*) trains a separate model for each human protein and all similar sequences. This and the differences in model architecture and training algorithms suggest that the models extract distinct features from their input. Therefore, we expected that the scores from EVE and our language model to be complementary and that combining scores may result in improved performance. We found that simply taking the mean of their pathogenicity scores already performs better than any of the two methods alone. More elaborate combinations, e.g., using ridge regression, did not lead to any further improvements. The resulting performance is shown in Fig. S14, where the combined score leads to a performance gain of 6.6% (or 6.8%) in mean correlation on assays compared to the PrimateAI LM (or compared to replicated EVE), 1.4% (or 1.7%) improvement mean AUC on ClinVar and increases in P-value by 11% (29%) for DDD, 3% (26%) for ASD and 17% (23%) for CHD.

Evaluations of PrimateAI-3D

PrimateAI-3D performance is benchmarked against both supervised and unsupervised variant pathogenicity classifiers. We found that PrimateAI-3D consistently outperforms other classifiers on all evaluation datasets (Fig. 3D). Summary statistics of model performance across all the six evaluation datasets are provided in Fig. S15 and Table S3. When the results are averaged across benchmarks, PrimateAI-3D is far ahead of any competing classifier (Fig. S15). It appears the reason why other classifiers come close to PrimateAI-3D in individual benchmarks is because we evaluated nearly 30 other algorithms; akin to multiple hypothesis testing, by statistical chance the performance of an algorithm may be an outlier on one particular benchmark, but their lack of consistency in the other five benchmarks indicates regression back to the mean. As we show in Fig. 3D, the second-place algorithm is different in each of the six benchmarks. A detailed breakdown of the performance of PrimateAI-3D for each of the 42 genes in UKBB is provided in Table S4. A detailed summary of performance of PrimateAI-3D and other benchmark classifiers on the 9 assays considered is given in Table S6.

PrimateAI-3D sensitivity and specificity on ClinVar

The ClinVar mean per-gene AUC metric (Fig. 3; also used in EVE (*67*)) implicitly corrects for different biases in ClinVar and enables a fairer comparison to methods directly trained on clinical annotations. A complication of directly measuring sensitivity and specificity in the ClinVar database is that human expert annotations are concentrated in a handful of disease genes that have been most heavily studied, with 50% of the total pathogenic missense variants in ClinVar coming from only 1.8% of the protein-coding genes in the genome (Fig. S16). This bias in annotation results in some genes having severe imbalance in their number of benign and pathogenic mutations, with >90% of labeled variants in the gene being either pathogenic or benign. Other machine learning classifiers that have been trained on human annotation databases have inadvertently learned the bias in annotation and take advantage of this property to assign higher scores to variants in genes with a high fraction of pathogenic variants in ClinVar (Fig. S17). To measure each classifier's sensitivity and specificity without the influence of annotation bias, we rank-normalized classifier scores for variants within each gene, and excluded genes with >90% of variants being pathogenic or benign in ClinVar. PrimateAI-3D achieved a sensitivity of 84.7% and specificity of 84.1% (percentile threshold: 57.7), and its AUC of 0.919

was the best performance among all classifiers (Fig. S18), which was notable given that the other classifiers (with the exception of EVE, PROVEAN, SIFT, LIST-S2) had been trained either on ClinVar or highly overlapping annotation databases such as HGMD (*166, 167*).

Using PrimateAI-3D to improve ClinVar

To assess the utility of PrimateAI-3D for revising ClinVar annotations, we compared a snapshot of the ClinVar database from September 2017 with the current database, and asked whether PrimateAI-3D scores were predictive of variants whose annotations had been revised in the interim. We defined the most confident *X*% PrimateAI-3D predictions as the *X*/2% variants with the highest predicted pathogenicity merged together with the *X*/2% variants with the lowest predicted pathogenicity. This implicitly converts the continuous PrimateAI-3D score into a binary benign/pathogenic classification. We downloaded ClinVar September 2017, reduced it to benign or pathogenic missense variants and only kept variants from genes with at least 20 variant annotations (30,295 variants). Then we looked up the annotations of those variants in ClinVar 2021. We found that 4,850 of the 30,295 variants (16%) had changed or lost their clinical annotation by 2021. Filtering the 30,295 variants to those that are also in the top 10% most confident PrimateAI-3D predictions, 2,905 variants remain. For 55/2,905 (2%) variants, ClinVar and PrimateAI-3D disagree. 29/55 (53%) variants changed ClinVar labels between 2017 and 2021. This is a 5 times higher fraction than for variants that agree between PrimateAI-3D and ClinVar (273/2755, 10%; Fisher's test P-value=10^{-24}) and indicates that at least half of all annotations that disagree between high-confidence PrimateAI-3D and ClinVar will change annotation in ClinVar over time. We repeated this analysis with different confidence thresholds for PrimateAI-3D (Fig. S19). Among the variants that were annotated as pathogenic in 2017, the top 10% with the lowest (most benign) PrimateAI-3D scores were 4-fold more likely to have had their ClinVar annotation consequence changed in the interim ($P < 10^{-3}$). Conversely, among the variants annotated as benign in 2017, the top 10% with the highest (most pathogenic) PrimateAI-3D scores were 6-fold more likely to have had their annotation changed ($P < 10^{-18}$) (Fig. S19). Even using the top 75% of all PrimateAI-3D predictions, there remains a 2-fold increase of ClinVar label changes among variants that disagree between ClinVar and PrimateAI-3D. In summary, discordance between PrimateAI-3D and ClinVar indicates a significantly elevated chance of annotation error in ClinVar and can be used to increase confidence in ClinVar annotations.

Candidate gene discovery

We tested enrichment of de novo mutations in genes by comparing the observed number of DNMs to the number expected under a null mutation model (*47*). We tested the de novo enrichment using twenty different missense pathogenicity predictors (see Methods for comparison section). We report genes that are identified as enriched when only counting missense DNMs with a PrimateAI-3D score ≥0.821. Some missense classifiers predicted scores in limited sets of genes, and we compensated for this by scaling the null mutation rates by the fraction of all missense sites with a pathogenicity score. For each missense predictor we estimated the excess missense DNMs without any missense classifier, and identified the pathogenicity threshold at which we captured that number of missense DNMs above that threshold. For two classifiers (DANN, LIST-S2) we found missense DNMs from healthy controls had skewed score distributions compared to the distribution of all scores genome-wide. We calculated per-threshold inflation factors via the ratio of the quantile from control DNMs to the quantile from all sites, at the same threshold. We identified an adjusted threshold as the highest threshold at which the excess corrected for the corresponding inflation factor exceeded the original excess. For example, for PrimateAI-3D the threshold was 0.821. We adjusted the genome-wide expectation for damaging missense DNMs by the fraction of missense variants that meet the threshold (roughly one-sixth of all possible missense mutations genome-wide). Each gene required four tests, one testing protein truncating enrichment and one testing enrichment of protein-altering DNMs, and both tested for just the DDD cohort and one where we excluded individuals with a protein-altering DNM in a gene previously identified with monoallelic or hemizygous inheritance for intellectual disability (ID). The genes with known links to ID were obtained from Genomics England PanelApp ID gene panels with confidence level of 3 (*108*), or found in Gene2Phenotype DDG2P subset where confidence was "definitive" (*109*). The enrichment of protein-altering DNMs was combined by Fisher's method with a test of the clustering of missense DNMs within the coding sequence. The P value for each gene was taken from the minimum of the four tests, and genome-wide significance was determined as $P < 6.41 \times 10^{-7}$ ($\alpha = 0.05$; 19,500 genes with four tests). We also excluded two genes, *BMPR2* and *RYR1* as borderline significant genes that already had well-annotated non-neurological phenotypes.

Fig. S22 shows the number of candidate genes discovered for each classifier, and while PrimateAI-3D is among the best performing algorithms. Because the number of candidate disease genes discovered in DDD (< 300) is a very small number compared to the number of variants evaluated in the six clinical benchmarks (which typically contain on the order of tens of thousands of variants), it is too noisy to be used as a meaningful metric for evaluating classifier performance, as the differences between the algorithms are not statistically significant.

Supplementary Text

1 Protein voxelization

Protein voxelization is the process of converting sets of protein atomic coordinates into tensors that have the same shape for all sets of coordinates. We explain our voxelization method first using two-dimensional atomic coordinates, followed by a straightforward extension to three dimensions.

To voxelize a variant, we first obtained the protein structure in which the variant occurs and determine the atomic coordinates of the Cα atom of the variant (Fig. S11A: blue point). Note that the protein structure either has the reference amino acid or no amino acid at all at the site of mutation (fill-in-the-blank in 3D; section "Model training"), but never an alternative amino acid. Next, we reduced the atoms of the protein to Cα atoms of alanine residues (Fig. S11A: red points). Then we defined a square of a certain size (Fig. S11B; imagine e.g. 6x6 Angstrom (Å)). We subdivided this square into smaller regular-sized squares called “voxels”, in this case 3x3 voxels of size 2Åx2Å. We identified each voxel by its row and column index. For example, the voxel in the top right is referred to as $V_{(1,1)}$. Then we moved the center of the central voxel in the voxel grid (Fig. S11: $V_{(2,2)}$, in the middle of the grid) onto the Cα coordinate of the residue with the mutation so that both points have the same coordinates (Fig. S11C: blue point from Fig. S11A has the same coordinates as the center of voxel $V_{(2,2)}$ in Fig. S11B). Now we looped through all voxel centers in the grid, starting with $V_{(1,1)}$. We determined the Cα atom that is closest to the center of $V_{(1,1)}$ (i.e. the “nearest neighbour”; Fig. S11C: point *NN*) and still within the scan radius r (Fig. S11C: red circle; typically 5Å). We calculated the Euclidean distance d between the two points (Fig. S11C). The closeness c between $V_{(1,1)}$ and *NN* is then defined as

Equation 1

$$c\left(V_{(1,1)}, A, C\alpha\right) = 1 - d/r$$

Finally, we repeated this procedure for all 21 amino acids (20 standard amino acids and one additional amino acid representing all non-standard amino acids), starting with the reduction to the Cα atoms of all cysteine residues, instead of alanine. This is followed by a repeat of the previous 21 iterations, but with Cβ atoms, instead of Cα (however, the Cα is kept for the variant with the mutation, i.e. the coordinates of the voxel grid center stay the same; Fig S11D). In the end, each voxel is associated with 42 closeness values, one for each amino acid and atom type combination (Figs. S11E-F). We refer to this set of values as the atomic distance profile of a variant. We also experimented with including more atom types, but only found diminishing returns.

The atomic distance profile is the first of two outputs of the voxelization procedure. The second output is calculated with the following differences: we did not reduce to certain amino acids or atom types. The *NN* therefore becomes simply the closest atom to a voxel center, across all amino acid atoms in the protein. Then we looked up the position of the residue from which atom *NN* comes in the sequence of the target protein. Instead of calculating closeness c, we only defined a function s that maps each voxel to the sequence position of this closest residue. For example, given a target variant at sequence position 11 in protein *BRCA1*, the atom closest to $V_{(1,1)}$ may come from a glycine residue at sequence position 32. Hence, $s(V_{(1,1)}) = 32$.

Moving the algorithm above from two to three dimensions, we only needed to increase the dimensionality of the voxel grid by one dimension. For example, the first voxel $V_{(1,1)}$ becomes $V_{(1,1,1)}$. Given a 3x3x3 voxel grid, the central voxel $V_{(2,2)}$ becomes $V_{(2,2,2)}$.

Evaluating different voxel grid sizes (from 3x3x3 to 19x19x19) and voxel sizes (from 1Åx1ÅxÅ to 3Åx3Åx3Å), we found that grid sizes above 7x7x7 and voxel sizes below 2Åx2Åx2Å failed improve performance. Therefore, we chose a grid size 7x7x7 with 2Åx2Åx2Å voxels. Note that an atom does not actually need to be inside the voxel grid to contribute to both voxelization outputs c and s. It suffices if the atom is within the scan radius r of a voxel. Conversely, even if an atom is within a scan radius, it does not automatically imply that the atom will contribute to c and s. With our chosen parameters, on average the atoms of 41 (minimum 1, maximum 205) different residues are within the scan radius of a voxel in the grid. Of those, an average of 21 different residues (minimum 1, maximum 67) are mapped to by s.

2 Details of structure quality features

We included several features indicating the confidence in the structure surrounding each voxel. First, we defined four binary indicators: whether the protein structure is present in AlphaFold DB as-is (i.e., with a perfect sequence match to one of our protein sequences), whether we used Modeller with AlphaFold DB structures as templates (in case the match was not perfect), whether we used HHpred and AlphaFold DB structures as templates in Modeller (when large parts of a protein were missing in AlphaFold DB), or whether we used HHpred exclusively (in case there was no similar match in the AlphaFold DB). For the structures that involved HHpred, we added three features corresponding to the minimum, mean and maximum predicted TMscore (*168*) of the templates found by HHpred. We also included B-factors from both AlphaFold DB and Modeller (where available) using the mapping function, which maps each voxel center to the sequence position of the residue with the closest atom to that center. For example, if $s\left(V_{(1,1,1)}\right) = 31$, then we looked up the AlphaFold DB B-factor of residue 31 and added it to the feature vector of voxel $V_{(1,1,1)}$. HHpred output contains a sequence alignment of up to 6 template proteins with known structure. For each residue in the target protein, we counted how often the other sequences in the alignment have non-gap amino acids at that position. This value indicates how many templates could be used at each position when a structure needs to be predicted with HHpred. We added this value to the feature vector of each voxel in the same way as for B-factors. In total, there are 10 features describing the quality of the protein structure around a voxel (Fig. S12B).

3 Species-differentiable evolutionary profiles

Let $\Sigma = \{\mathrm{A}, \ldots, \mathrm{W}, -\}$ be the set of all 20 amino acids A, … , W plus a gap token denoted as "$-$". M is a $|S|$-way multiple sequence alignment S ($|S| = 592$) and M_i^s is the amino acid at protein position i in alignment $s \in S$. The evolutionary profile of amino acid A at protein position i is defined as $f_i^A = \sum_s w[M_i^s = A]$, where [] is the Iverson bracket and $w = \frac{1}{|S|}$ is a normalization constant. f calculated only from the multiz100 alignments ($|S| = 100$) is part of the input features for PrimateAI (*17*). We interpreted f as a signal for human pathogenicity. A constant w implies that variants from all species and alignments are equally important contributors. For example, a variant in chimp (closely related to human) increases the frequency of an amino acid by the same amount as the same variant in zebrafish (distant from human). We argue that this should not be the case. For PrimateAI-3D, we therefore allowed each of the 592 whole proteome alignments to have a different weight. More precisely, we defined a new evolutionary profile $f'^A_i = \sum_s w_s[M_i^s = A]$, where w_s is the weight of each alignment.

For example, assume that $i = 31$, $S = \{S_1, S_2, S_3\}$ and $\Sigma = \{L, P\}$ and that the two amino acids in the alignments at position 31 are L for alignment S_1 and P for alignments S_2 and S_3 respectively. Assume further that $w_{S_1} = 0.1$, $w_{S_2} = 0.05$ and $w_{S_3} = 0.2$. The one-hot encodings of the amino acids at position 31 are $< 1,0 >$ (for S_1), $< 0,1 >$ (for S_2) and $< 0,1 >$ (for S_3). It follows that $f'^L_{31} = w_{S_1} = 0.1$ and $f'^P_{31} = w_{S_2} + w_{S_3} = 0.05 + 0.2 = 0.25$.

Instead of calculating each w_s from the alignments themselves (e.g. via similarity to other sequences, as often performed for Potts models of MSAs (*169*)), we initialized each w_s to $\frac{1}{|S|}$ before training, and let the parameters be differentiable during training. This means PrimateAI-3D learns itself how important each of the 592 species is as contributors to the pathogenicity signal of f'^A_i.

4 Evolutionary profile features

The evolutionary profile function f'_i is equivalent to a 1D-convolutional layer without bias if we interpret the 21 amino acids (20 standard amino acids plus a gap token) as input samples and the number of alignments ($|S|$) as features (considering only one amino acid, the 1-hot encoding of an amino acid is only a single value that is either 0 or 1). Denote this convolutional layer $Conv_{f'}$. To make use of the typical parameters associated with a convolutional layer, we introduced a bias term, increased the number of filters to 10 and activated each output via the ReLU activation function (the latter enables modelling non-linear relationships between species). In the end, the input to $Conv_{f'}$ are the $|S|$ 1-hot encoded amino acids at a sequence position i and the output is an evolutionary profile with 10*21=210 elements. In order to merge this evolutionary profile with voxels (above), we again make use of function s. For example, given $s\left(V_{(1,1,1)}\right) = 31$, we extracted the $|S|$ amino acids at sequence position 31 from the alignments of the target protein and 1-hot encode and convolved them using $Conv_{f'}$. The output is concatenated with the feature vector of $V_{(1,1,1)}$, extending it by 210 elements (Fig. S12C). Note that unlike for the other features, the gradient does not stop at these 210 elements, but is backpropagated and used to update the weight w_s of each alignment.

Supplemental Figures

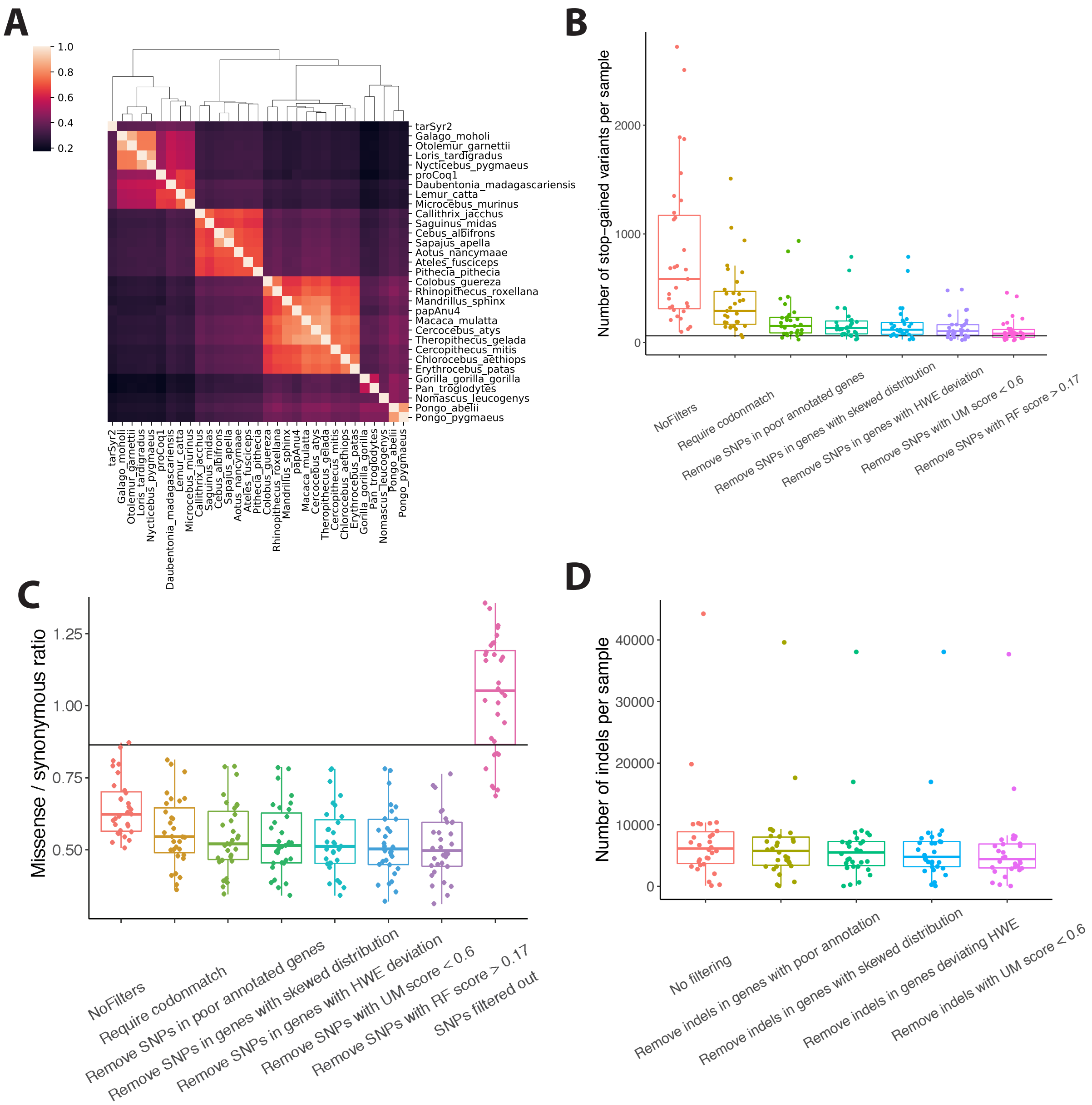

Fig. S1. Variant filtering steps improve variant quality. (**A**) Heatmap of Spearman correlation of codon-match metrics among 31 primate reference species naturally clustering primates into four major groups, including great apes, Old World monkeys, New World monkeys, and lemurs / tarsiers. Codon-match indicates a specific codon of primate reference species matches human. Lighter colors represent higher correlation between two species. (**B**) Boxplots showing that the average number of stop-gained variants per sample of each primate reference species was gradually reduced to close to human level after a series of variant filtering steps, including requiring codon-match, removing SNPs in poorly-annotated genes or in genes with skewed random forest score distribution or deviating from Hardy Weinberg equilibrium (HWE), and removing SNPs with unique-mapper (UM) score <0.6 or RF score >0.17. Each dot represents the average number of stop-gained variants of each primate reference species. The black line shows the average number of stop-gained variants of human samples from Platinum genome project. (**C**) Boxplots showing that missense / synonymous ratios (MSR) decreased after variant filtering steps. The pink box shows the MSR of variants that were filtered out. Each dot represents the MSR of each primate reference species. The black line represents MSR of human samples. (**D**) The average number of indels per sample of each primate reference species diminished after filtering steps. For all the boxplots, box lengths represent the interquartile of data points and the whiskers extend to 1.5 times the interquartile range from the box.

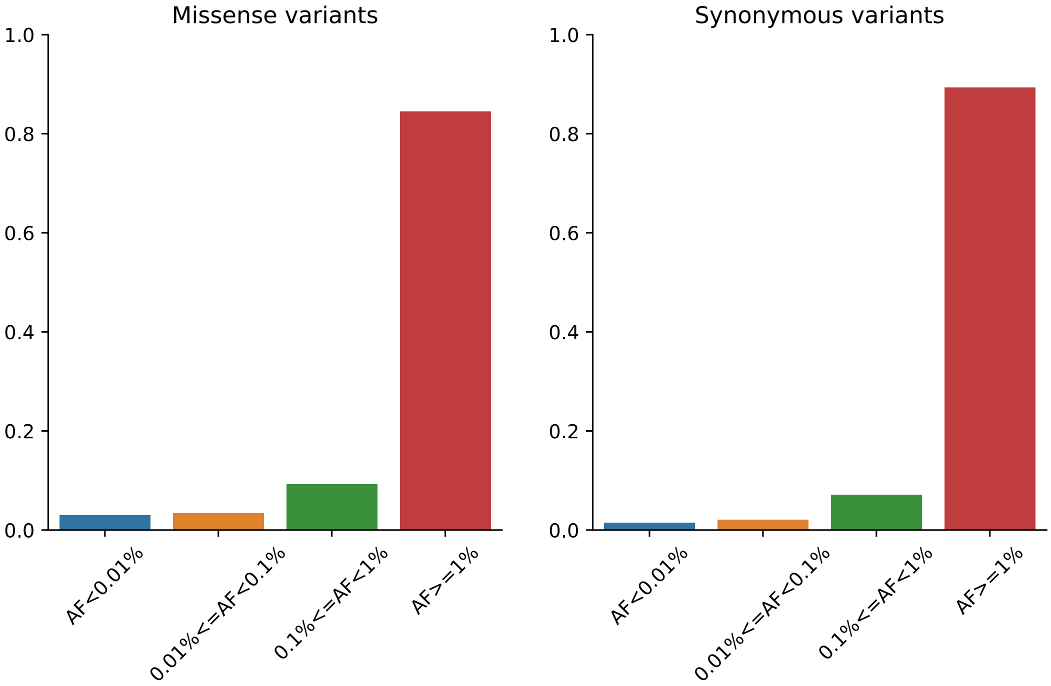

Fig. S2. Allele frequency spectra for simulated primate variants. Barplots show the fraction of primate missense (left panel) and synonymous (right panel) variants falling in each of the four allele frequency bins. The simulated primate variants were sampled according to the gnomAD allele frequencies, mimicking the sample sizes of primate species.

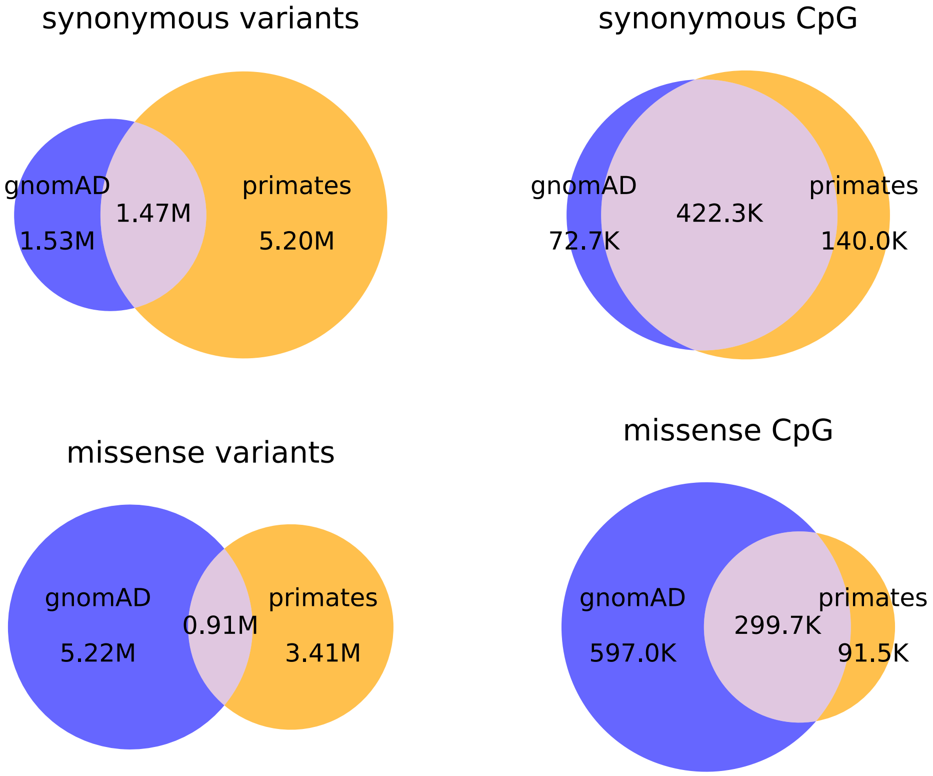

5 **Fig. S3. Venn diagrams show small overlap between gnomAD (blue) and primates (orange) for both synonymous and missense variants.** Large fractions of the transition variants occurring at CpG sites are shared between gnomAD and primates, particularly the synonymous variants.

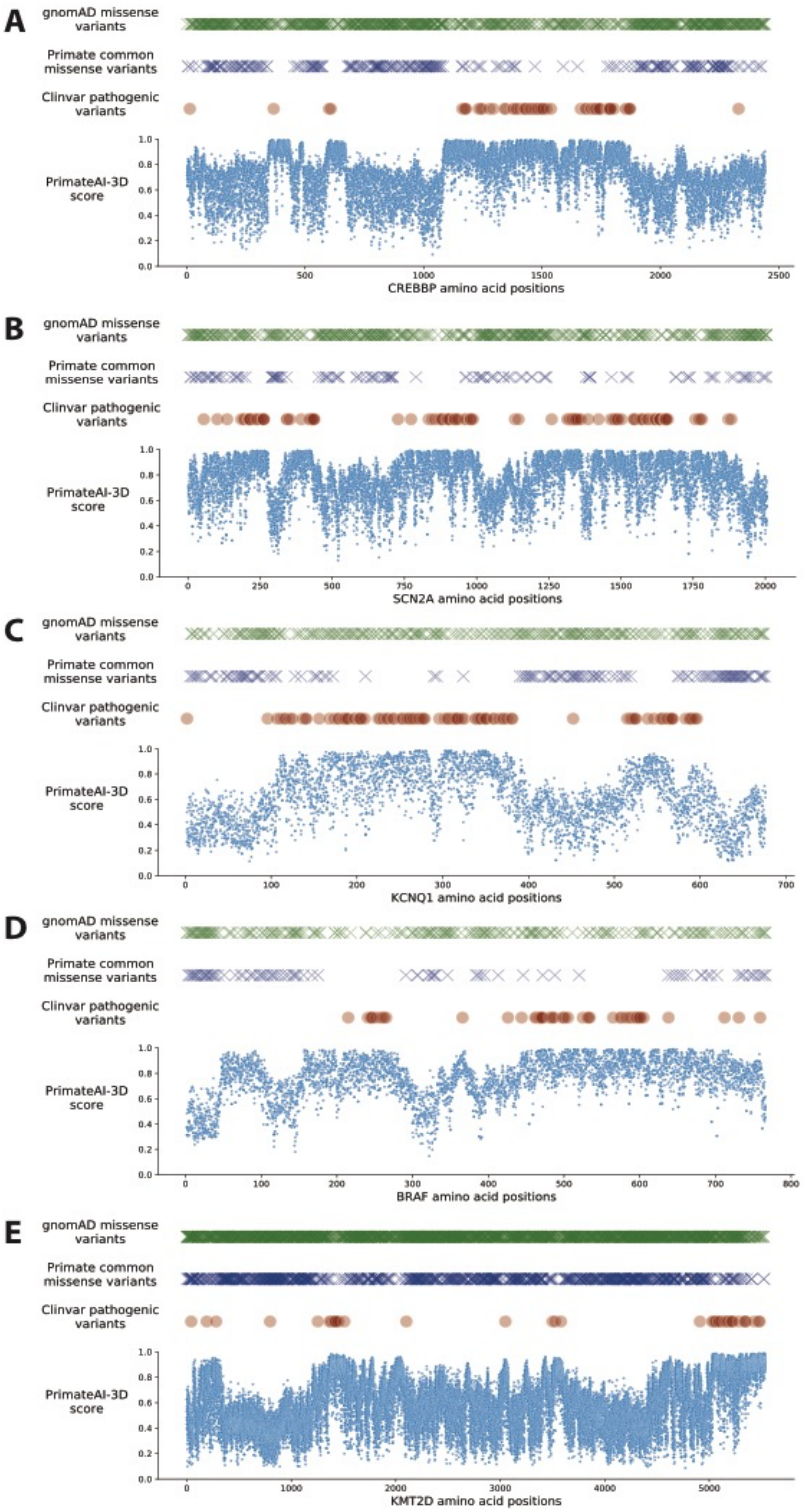

Fig. S4. Observed gnomAD (green) or primate (purple) missense variants at each amino acid position in genes. (A-D) The distribution of gnomAD missense variants (green crosses) along the genes *CREBBP* **(A)**, *SCN2A* **(B)**, *KCNQ1* **(C)**, *BRAF* **(D)**, and *KMT2D* **(E).** Blue crosses represent observed primate missense variants along the genes. Dark red circles represent observed ClinVar pathogenic missense variants along the genes. Blue dots of the bottom scatterplots show the predicted pathogenicity scores of all possible missense substitutions, which are the PrimateAI-3D scores at each amino acid position.

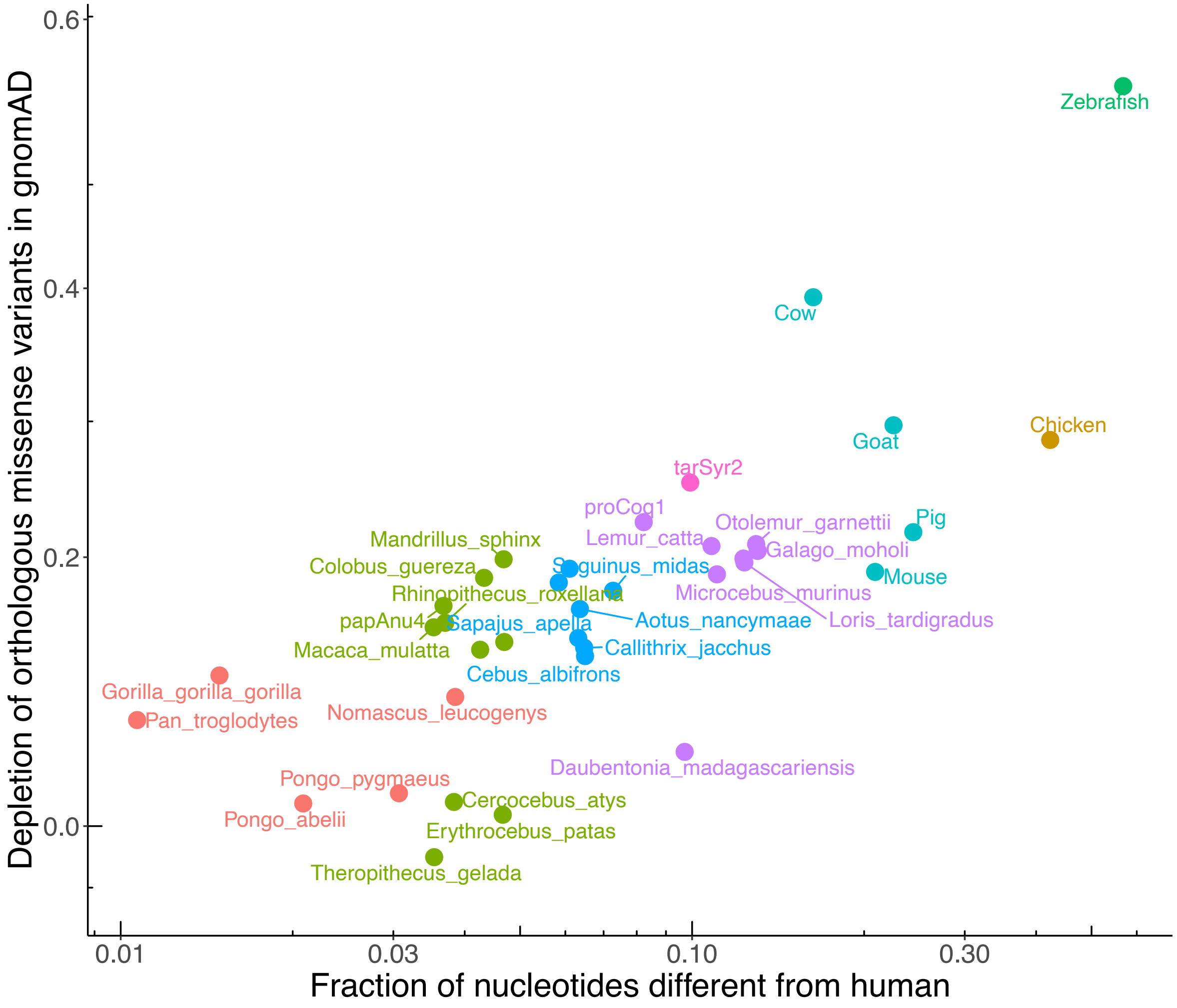

Fig. S5. Scatter plot showing that natural selection purifies potentially deleterious missense variants across species. The x-axis shows the depletion of orthologous missense variants observed in primates, mammals, chicken and zebrafish at common human allele frequencies (>0.1%) from gnomAD. The y-axis shows the species' genetic distance from human, measured by the fraction of nucleotides different from human.

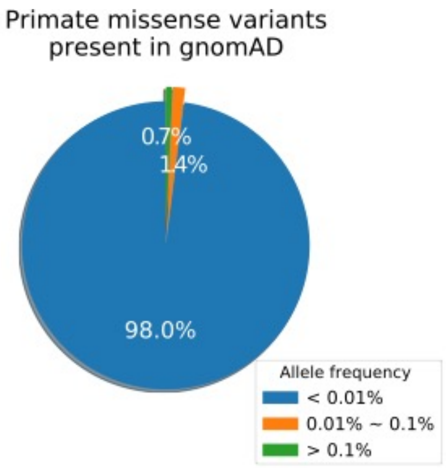

Fig. S6. Pie chart showing fractions of primate missense variants observed at different allele frequencies (AF) in gnomAD databases. Blue represents variants either not observed in gnomAD or with rare allele frequencies (< 0.01%). Orange and green show the fraction of primate variants with 0.01% <AF < 0.1% or common allele frequencies (>0.1%), respectively.

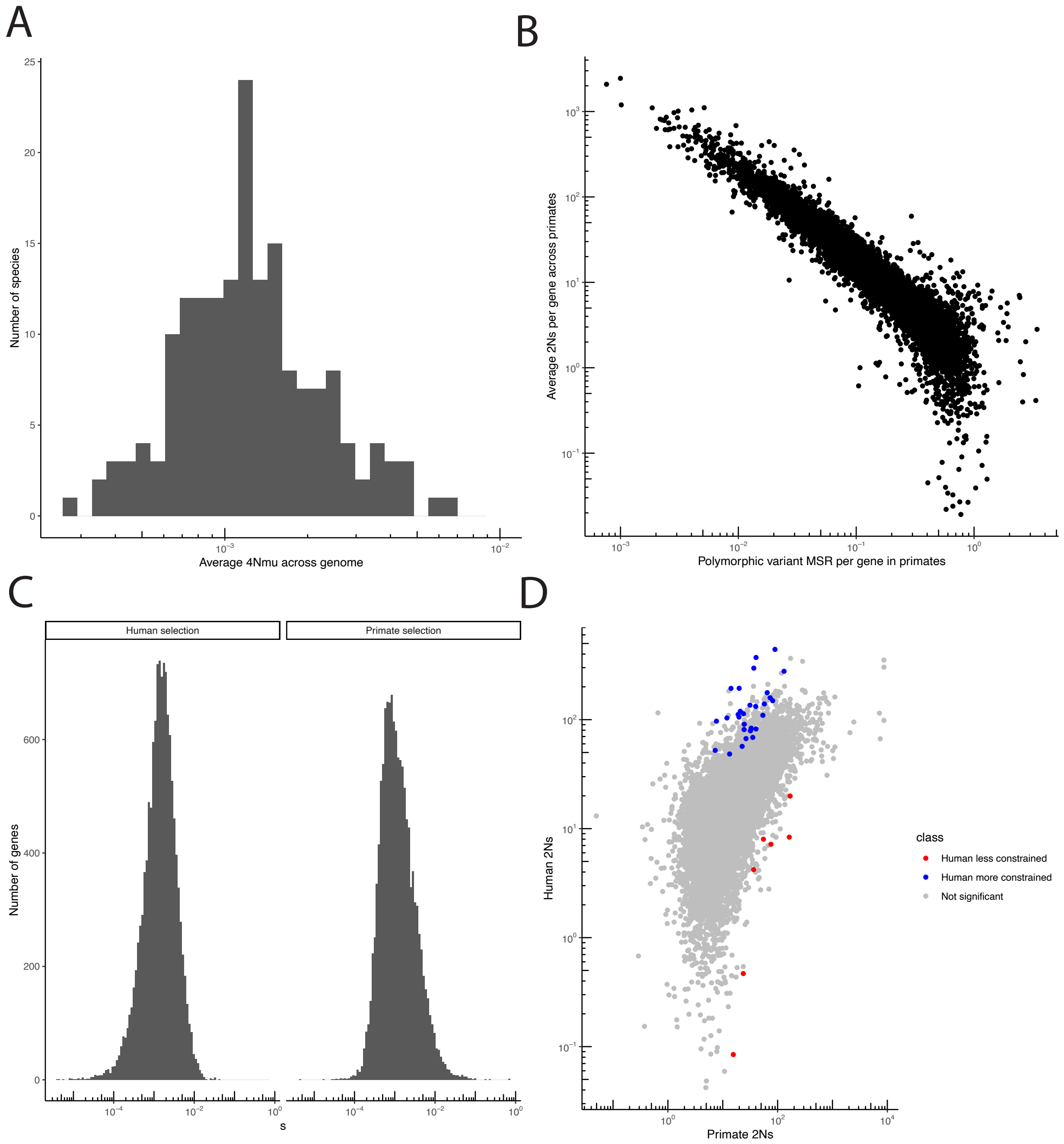

Fig. S7. Population genetic model fitting to human and primate data. **(A)** The distribution of population-scaled mutation rates across all species. **(B)** The correlation between pooled primate missense: synonymous ratio and inferred selection. The x-axis shows the missense : synonymous ratio for each gene when pooled across all non-human primates. The y-axis shows the inferred 2Ns for each gene. **(C)** The distribution of fitness effects across genes in humans and non-human primates. Histogram is over all genes that pass the filters to be used in the analysis. **(D)** The correlation between human selection and primate selection. The x-axis shows the strength of selection in humans, and y-axis shows the strength of selection in primates. Highlighted points are significant according to point the population genetic model and the MSR regression.

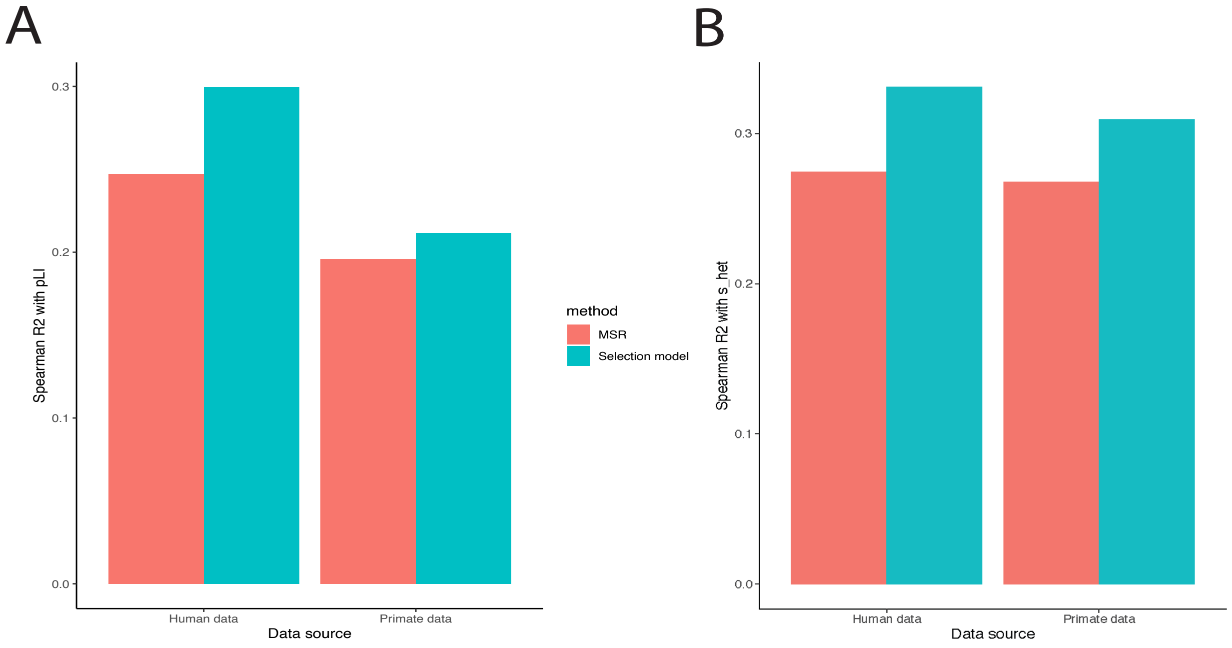

Fig. S8. Correlation of missense : synonymous ratios and selection coefficient estimates in humans and primates. (A-B) Barplots show the Spearman correlation of those two metrics with pLI (**A**) and s_het (**B**). Red bars represent correlation of missense : synonymous ratio of polymorphic variants with pLI or s_het. Blue bars show correlation of estimated selection coefficients. Bars are grouped by whether they are based on human data or pooled primate data.

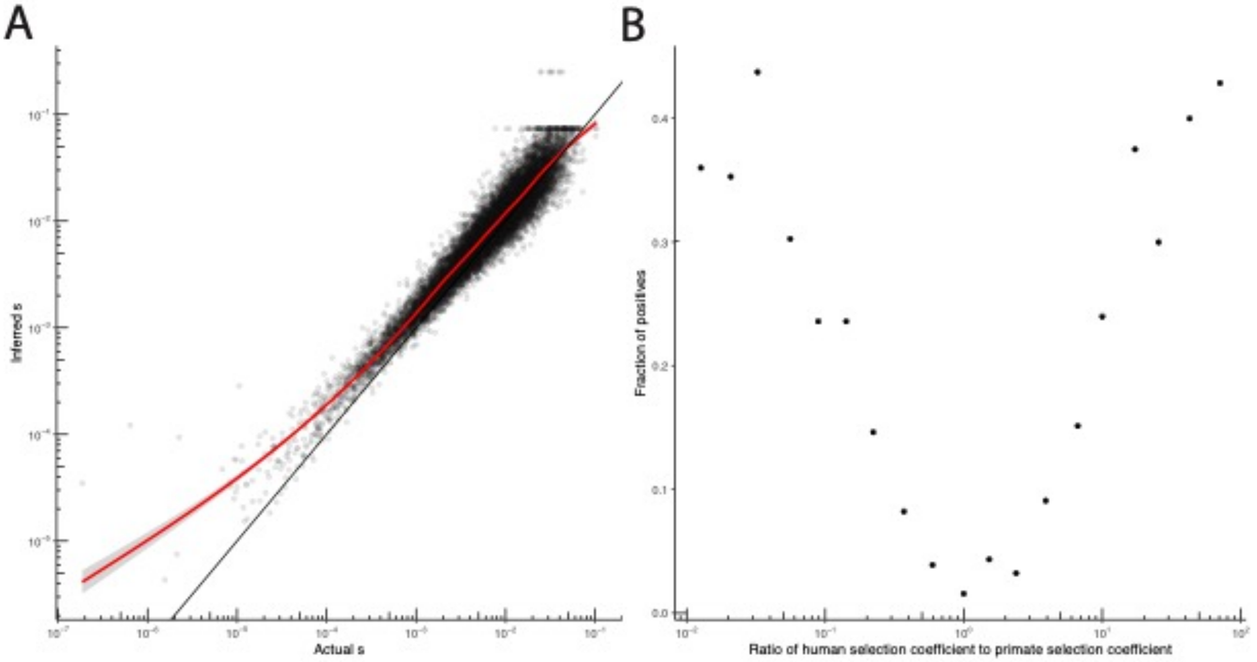

Fig S9. Performance of Poisson random field model in simulations. (A) Inference of simulated selection coefficients is highly accurate. The x-axis shows the selection coefficient simulated, as described in the text, while the y-axis shows the inferred selection coefficient using the method described in the text. The solid black line indicates the line y = x, while the red line is a moving average. **(B)** The likelihood ratio test is well powered and has a low false positive rate. The x-axis shows the ratio between the simulated human selection coefficient and the simulated primate selection coefficient. The y-axis shows the number of positives at an FDR of 5% following the Benjamini-Hochberg procedure. Note that the middle point, $10^0 = 1$ indicates no difference between human and primate selection.

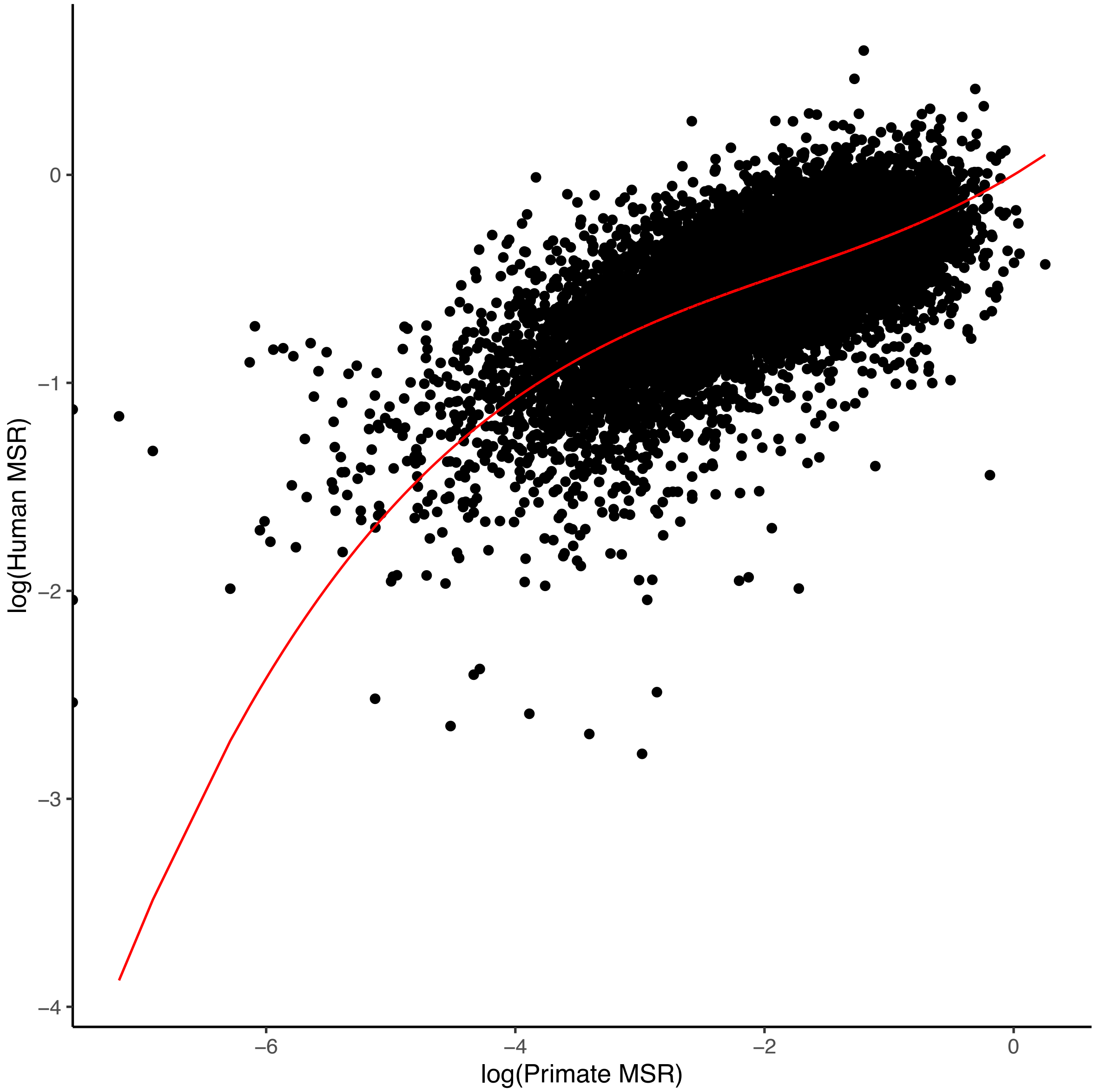

Fig. S10: Relationship of human and primate missense : synonymous ratio based on Poisson generalized linear mixed modeling. The x-axis shows the log-scaled missense : synonymous ratio among polymorphic variants in primates compared. The y-axis shows the log-scaled missense : synonymous ratio among polymorphic variants in humans. The red line represents the best-fit relationship as inferred by the model. 5

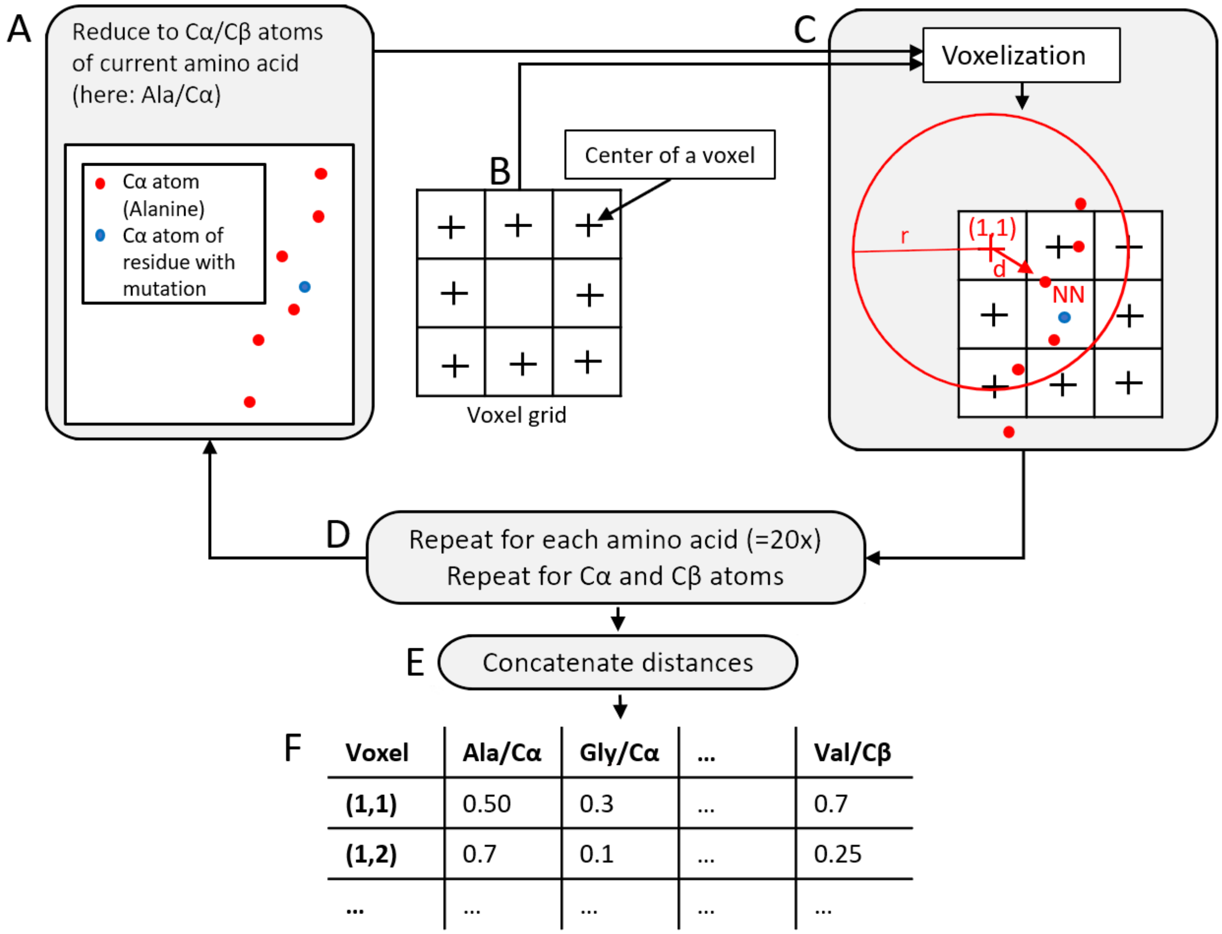

Voxel	**Ala/Cα**	**Gly/Cα**	**…**	**Val/Cβ**
(1,1)	0.50	0.3	…	0.7
(1,2)	0.7	0.1	…	0.25
…	…	…	…	…

Fig. S11. Illustration of voxelization procedure in 2D projection. (A) Given a target site, the corresponding structure is reduced to **Cα** atoms of a particular amino acid type (here: alanine; red), plus the target **Cα** atom (blue). A voxel grid (**B**) is centred on the target **Cα** (**C**). The **Cα** atom (NN) closest to the first voxel (1,1) is determined. Their Euclidean distance *d* is divided by maximum scan radius *r* to obtain a relative distance. Subtracting that ratio from 1 turns the relative distance into a relative closeness. This procedure is repeated on various levels: for each voxel in the grid; for each amino acid type; for **Cβ** atoms instead of **Cα** atoms.

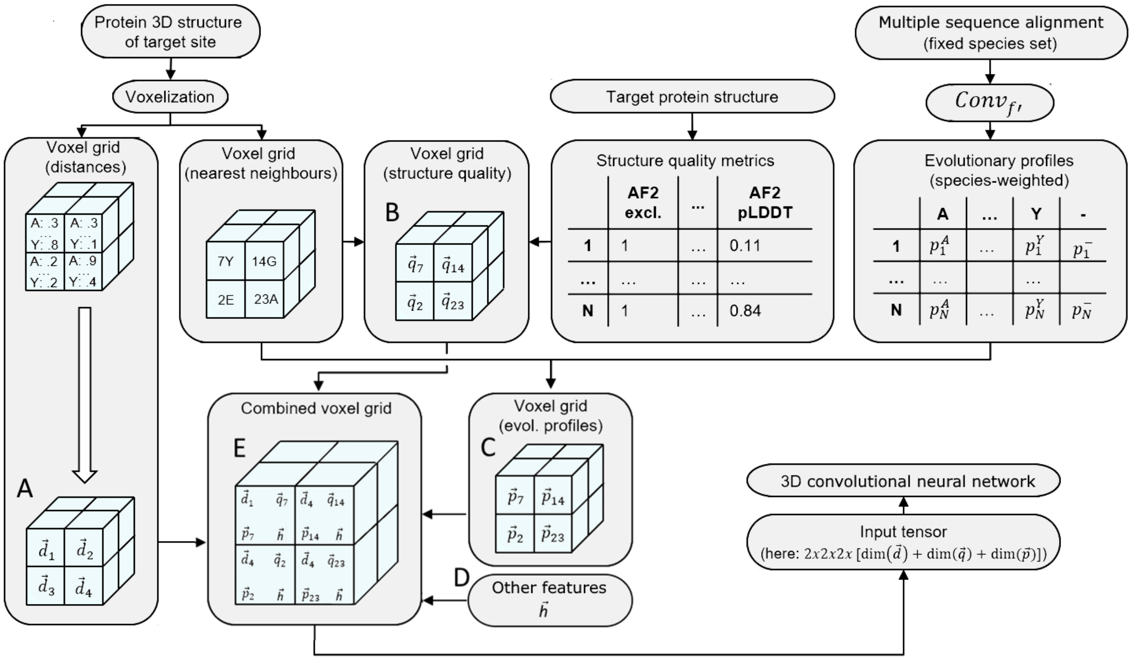

Fig. S12. Associating voxels with features. (**A**) Each voxel is associated with its amino acid distance profile *d*. (**B**) The mapping of each voxel center to the closest residue is used to look up structure quality metrics *q*. (**C**) Similarly, the mapping is used to associate each voxel with its evolutionary profile *p* of the closest residue. (**D**) Other features that are associated with each voxel include the 1-hot encoding of the target amino acid before mutation and indicators whether the central residue has been removed (fill-in-the-blank in 3D; section "Model training") or not. (**E**) Feature vectors *d, q, p* and *h* are concatenated and used as input to a 3D convolutional neural network.

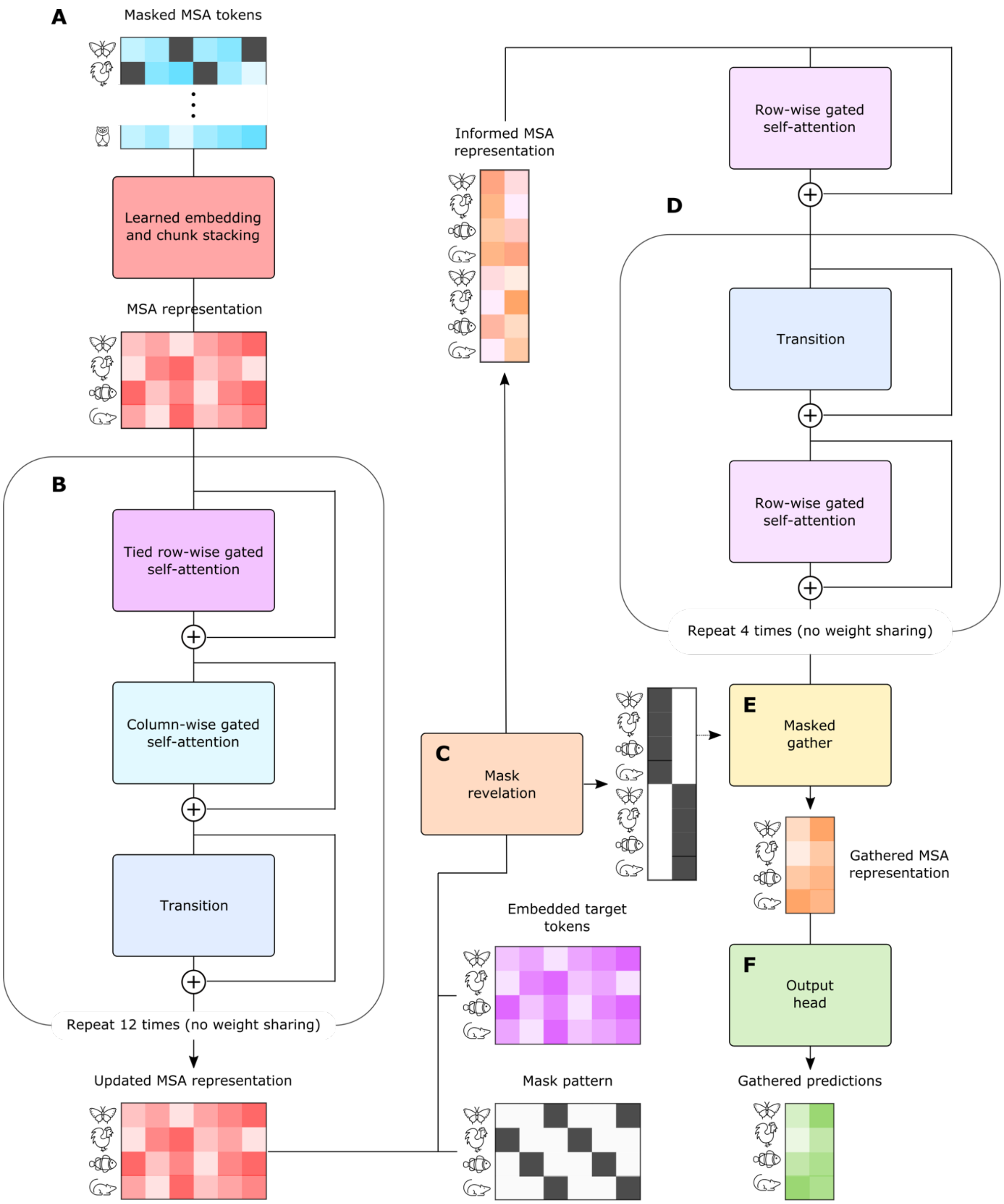

Fig. S13: PrimateAI language model architecture. (**A**) An initial MSA representation is created by learned embedding and stacking of MSA sequences. (**B**) Axial attention blocks develop the MSA representation. (**C**) Mask revelation gathers features aligned with mask sites. For each masked residue in a row, it reveals embedded target tokens at other masked locations in that row. (**D**) Attention is applied to gathered rows to interpret mask revelations. (**E**) MSA features are gathered from locations where target embeddings remained masked. (**F**) An output head, consisting of a transition and perceptron, maps the gathered MSA representation to predictions.

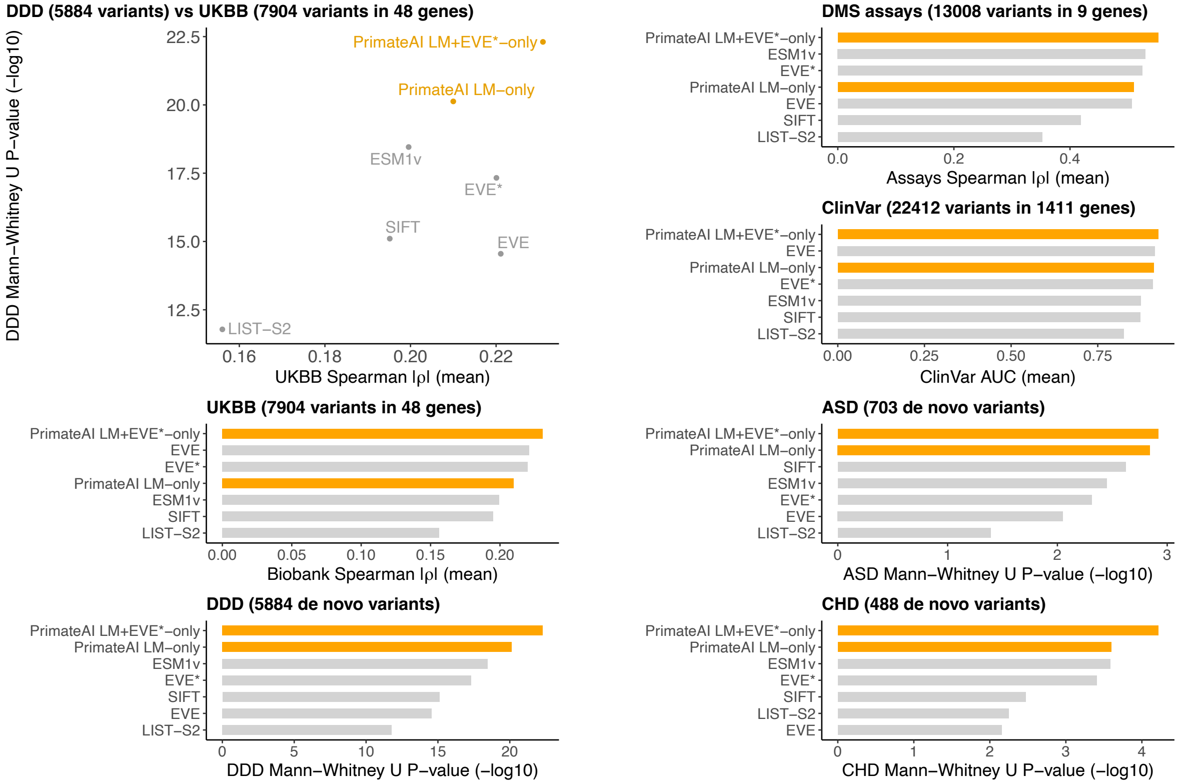

Fig. S14. Evaluation performance of the language modelling part of PrimateAI-3D (PrimateAI LM-only). The performance of PrimateAI LM-only is compared to the replicated VAE part of EVE (labelled "EVE*") model and their combined score (labelled "PrimateAI LM+EVE*-only"). It is further compared to a selection of competitive unsupervised methods (ESM1v, SIFT, LIST-S2). In clockwise direction starting from the top left, the individual panels correspond to evaluation on DDD vs UKBB, DMS assays, ClinVar, ASD, CHD, DDD and UKBB. For DMS assays and UKBB, the summary statistics are given in terms of absolute value (|corr|) of correlation between score and an experimental measure of pathogenicity, i.e., mean phenotype (UKBB) or assays score (DMS assays). For DDD/ASD/CHD, we calculated the P-value of Mann-Whitney U test for control and case distributions over all datasets. For ClinVar, we measured the AUC averaged over all genes.

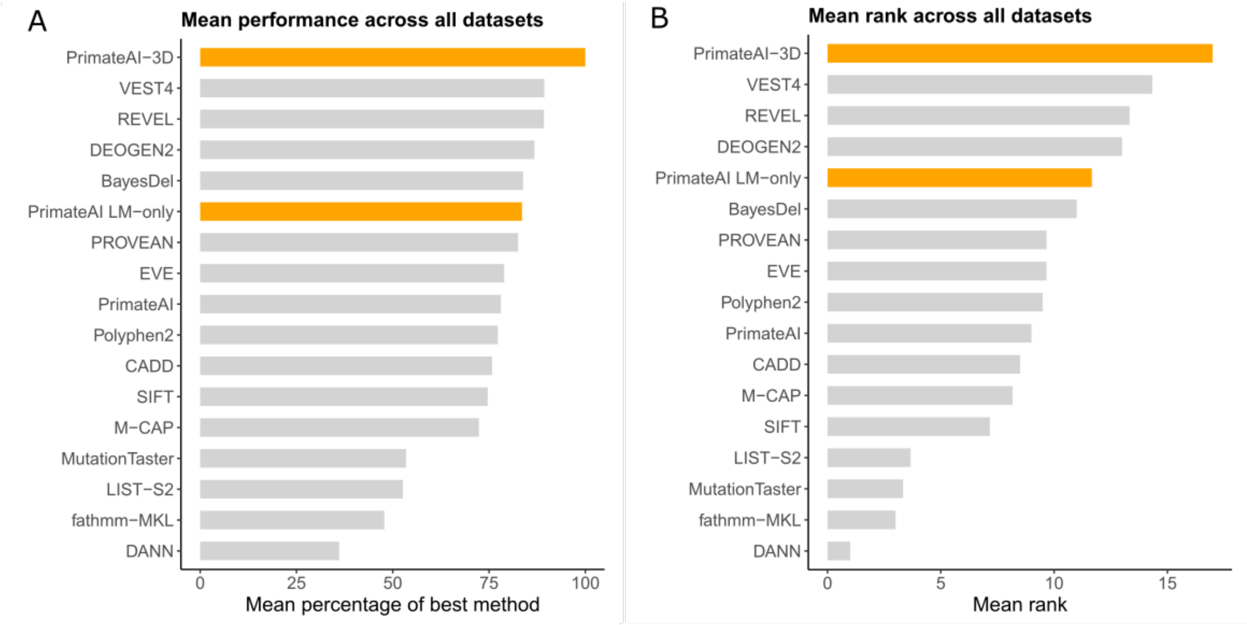

Fig. S15. Combining performance metrics from all evaluation datasets. (A) For each of the six evaluation datasets, the performance metric of each method was divided by the maximum performance achieved across all methods. The average of that percentage across datasets is the "Mean percentage of best method" for each method. **(B)** The rank of the performance metric of each method is determined separately for each dataset and then averaged to create one mean rank value for each method.

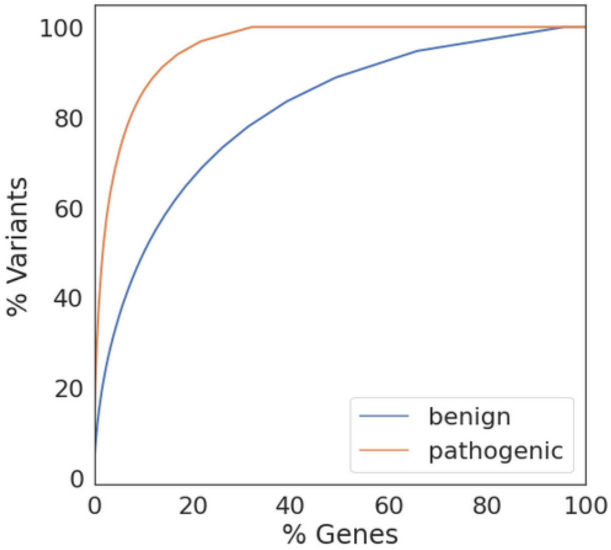

Fig. S16. Fractions of ClinVar variants covered by genes in ClinVar. The x-axis is the percentage of genes in ClinVar with at least one 1-star variant annotation. The y-axis is the percentage of ClinVar 1-star variants covered by genes in ClinVar. Each point in a line indicates the minimum percentage of genes required (x-axis) to cover a certain percentage of ClinVar variants (y-axis). For example, 50% of all pathogenic variants in ClinVar come from 1.8% of ClinVar genes.

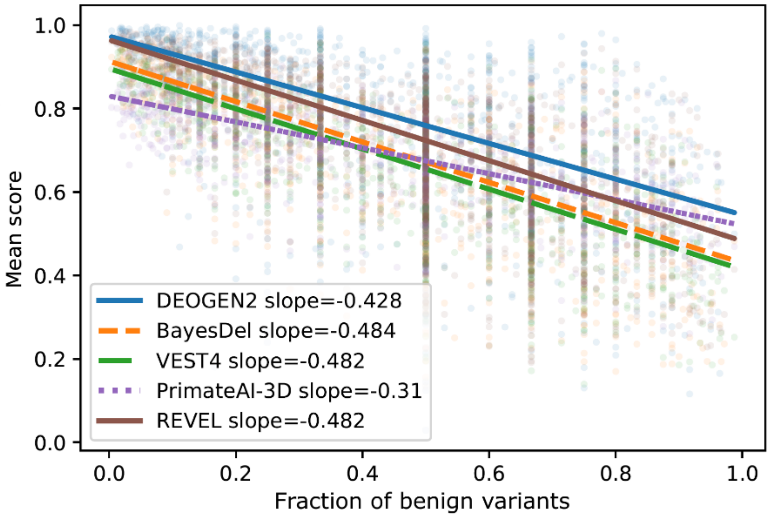

Fig. S17. Dependency of pathogenicity scores on the per-gene ratio of benign to pathogenic variants in ClinVar. We calculated the ratios "#benign/(#benign+#pathogenic)" for ClinVar genes with at least one benign and pathogenic variant (x-axis). For each prediction method, we then calculated the mean score for each gene (y-axis). Fitting a separate regression line for each method, the slope of PrimateAI-3D (-0.31) is below the slopes of other methods (-0.428 to -0.484), indicating that other classifiers' performance on ClinVar are affected by fitting to the per-gene ratio of benign to pathogenic variants in ClinVar, likely because they were trained directly on ClinVar or highly overlapping databases such as HGMD.

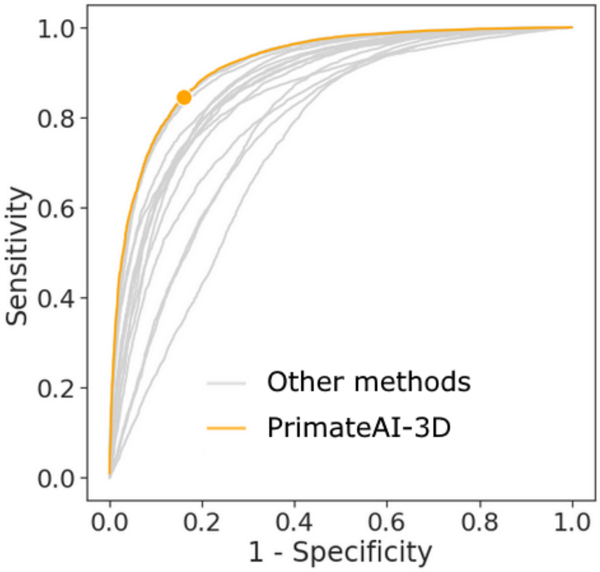

Fig. S18. Global ClinVar ROC curves. Other methods represent those classifiers used in Fig. 3. For PrimateAI-3D, the point that maximizes sensitivity+specificity is highlighted (sensitivity: 84.7%; specificity: 84.1%; percentile threshold: 57.7). This sensitivity+specificity is also the maximum among all other methods.

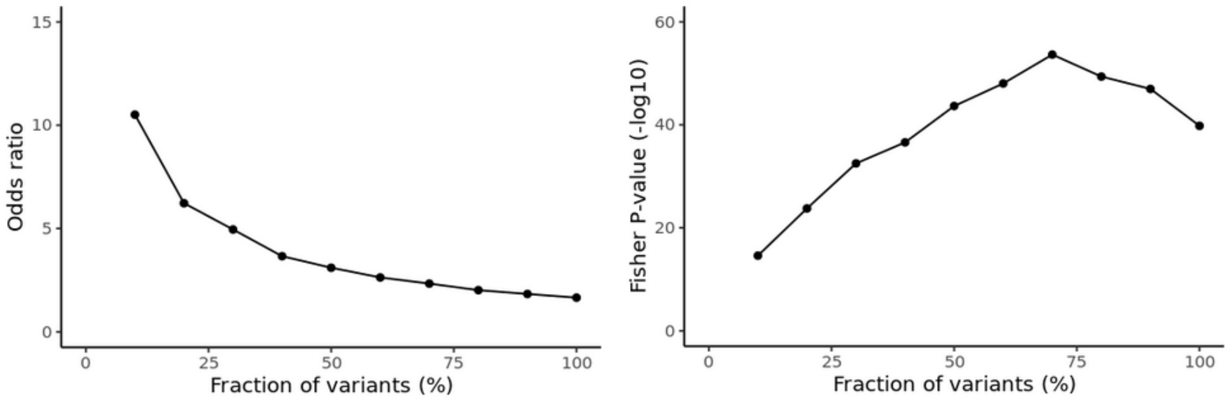

Fig. S19. PrimateAI-3D detects low-confidence ClinVar annotations. We took different percentages of the most confident PrimateAI-3D predictions and measured their agreement with benign and pathogenic annotated missense variants found in the September 2017 version of ClinVar. We also distinguished between ClinVar variants whose annotations were changed or unchanged between September 2017 and September 2021. We determine the odds of annotation change in variants that agree between PrimateAI-3D and ClinVar (left panel). We do the same for variants that disagree. The y-axis is the conditional maximum likelihood estimate of the ratio of the two odds. The x-axis indicates the fraction of top PrimateAI-3D variants. For example, a 20% fraction of variants means that we used the 10% most pathogenic and 10% most benign predicted variants. The x-axis of the right panel is the same as in the left panel and the y-axis indicates the Fisher's exact test P-value of the corresponding odds ratio shown in the left panel.

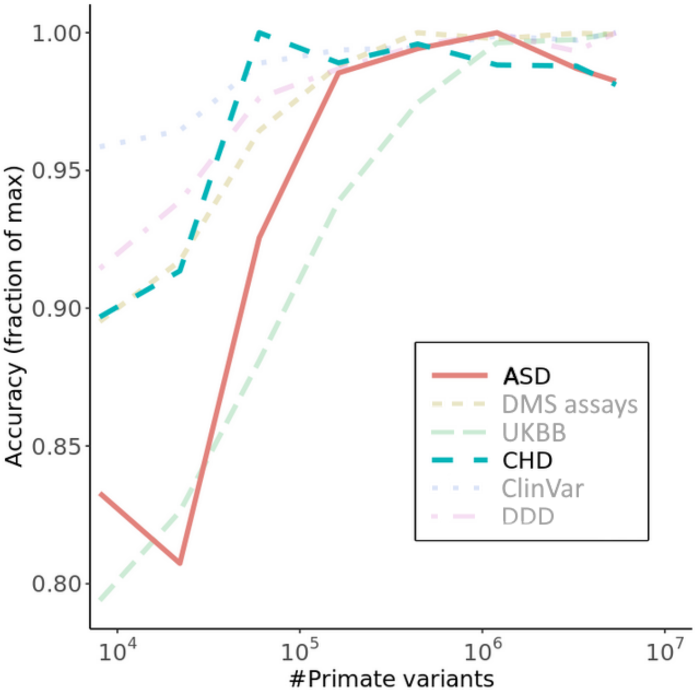

Fig. S20. Impact of training dataset size on classification accuracy (extended). Performance of PrimateAI-3D increases with the number of common human and primate variants in the training dataset (x-axis). Performance of each dataset (y-axis) was divided by the maximum performance observed across all training dataset sizes. ASD and CHD are highlighted because they were excluded in Fig. 5A.

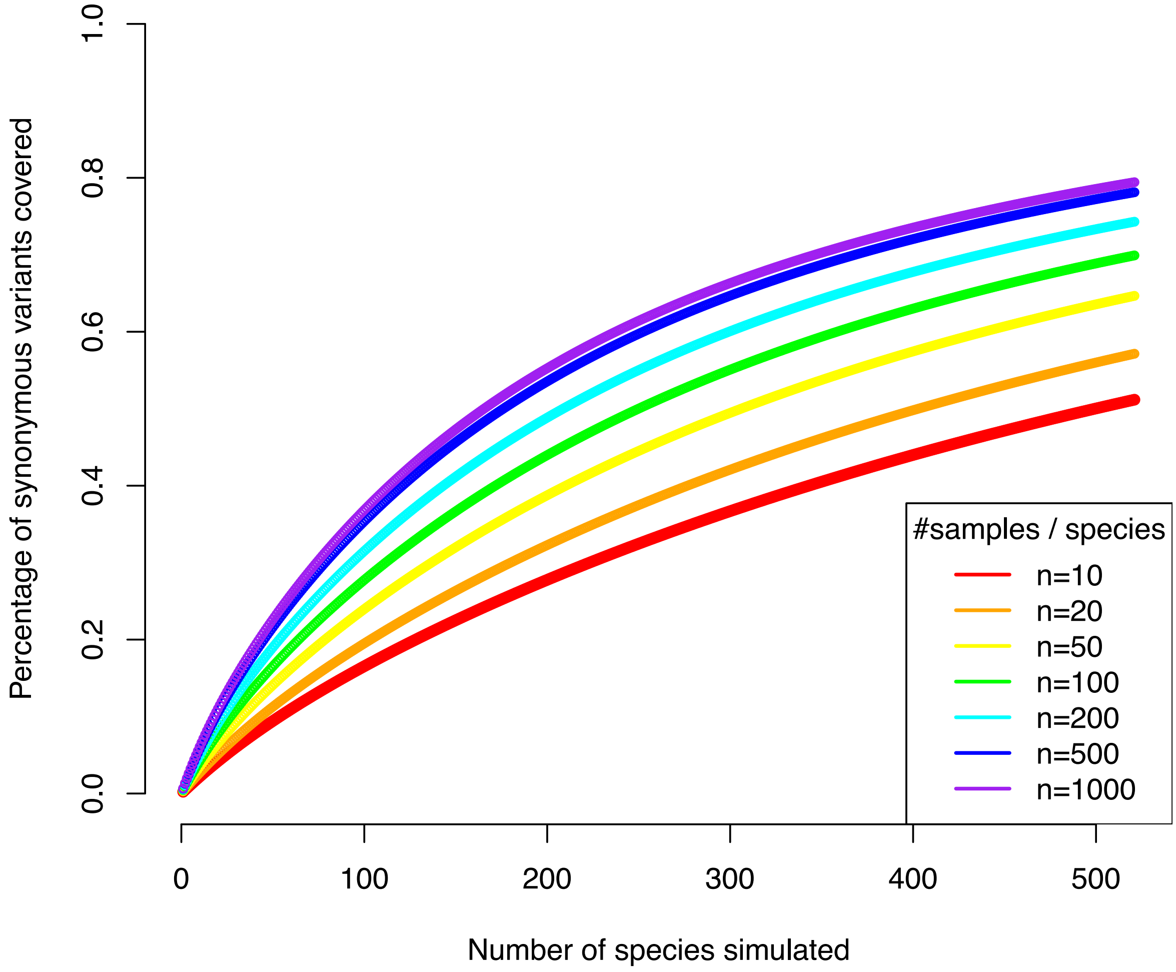

5 **Fig. S21. Saturation of human synonymous variants by sampling common variants present in the 521 extant primate species.** The line colors represent various sample sizes for the simulated primate species, including 10, 20, 50, 100, 200, 500 and 1000.

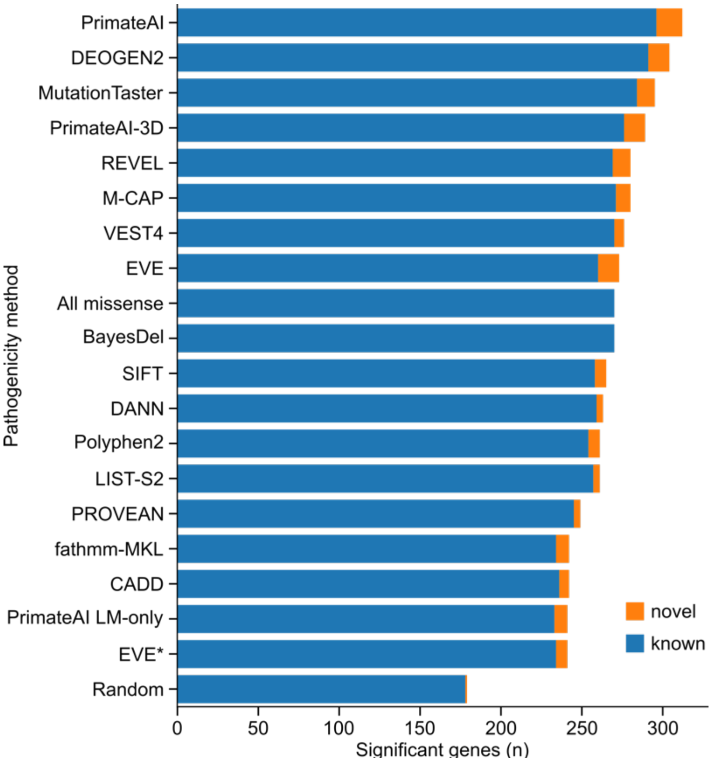

Fig. S22. Number of genome-wide significant genes by missense pathogenicity prediction methods, identified through enrichment of de novo mutations over expectation. Note that due to the small number of genes discovered (< 300) the differences between the algorithms are not significant. 5

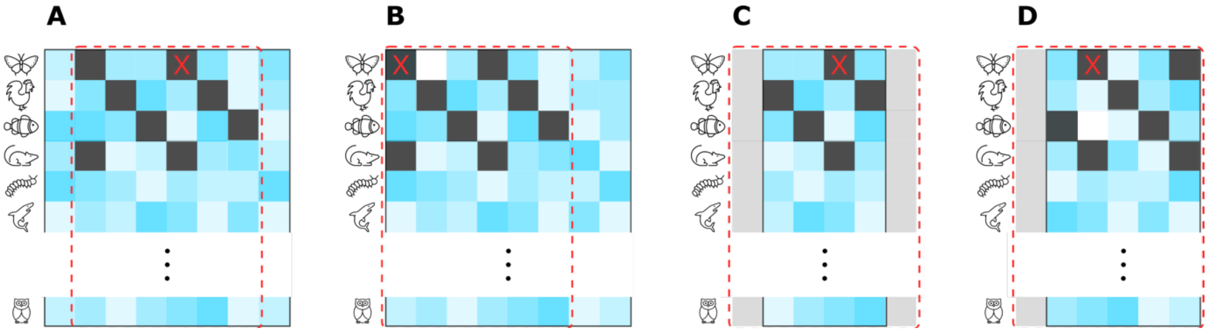

Fig. S23: Cropping, padding, and masking of MSAs for PrimateAI LM. A location of interest in the query sequence is indicated by an X, mask locations are black, padding is gray, and crop regions are indicated by a dashed line. In these examples, mask stride is 3 and cropping window width is 6 residues. (**A**) Away from MSA edges, a position of interest is at the right side of the center of the crop region. (**B**) A crop region is shifted to the right of the location of interest to avoid going over an MSA edge. (**C**) An MSA for a short protein is padded to fill a crop region. (**D**) A crop region is shifted to the right of a location of interest to minimize padding and the MSA is padded to fill the crop region.

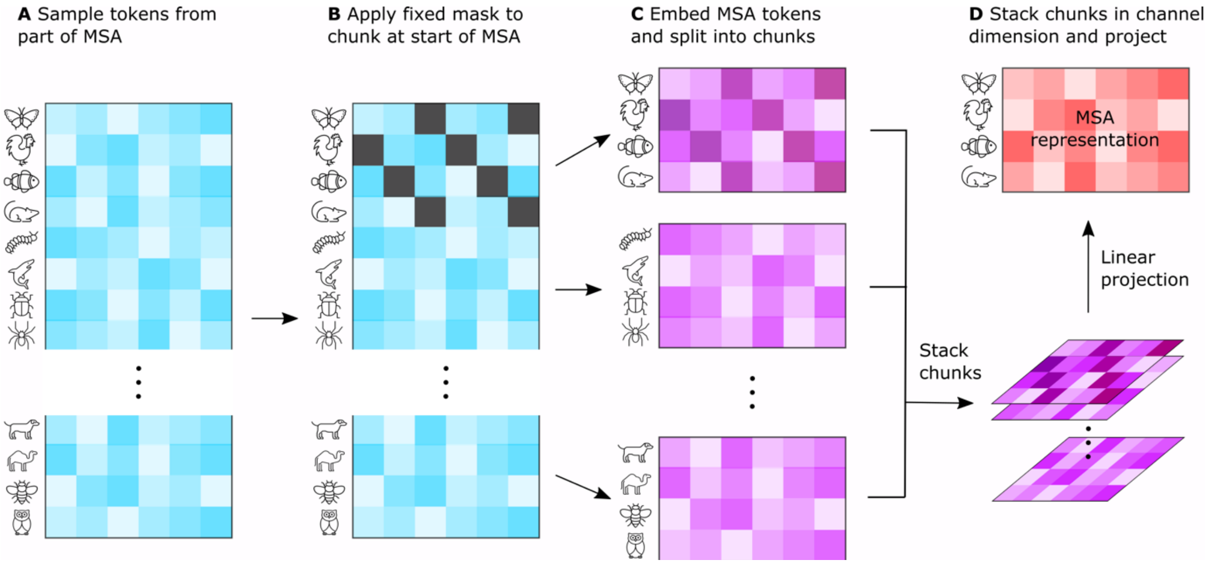

Fig. S24. MSA masking, learned embedding, and chunk stacking. (**A**) Part of an MSA with a contiguous set of residues and a random set of non-query protein sequences is sampled. (**B**) A fixed mask pattern is applied to a chunk of sequences at the start of the MSA. In this example, the mask pattern is applied to the first 4 sequences and has a stride of 3. (**C**) Tokens are replaced with learned embeddings, which are summed with learned position embeddings for residue columns before layer normalization. The embedded tokens are divided into chunks, which (**D**) are concatenated in the channel dimension and then linearly projected to form an initial MSA representation.

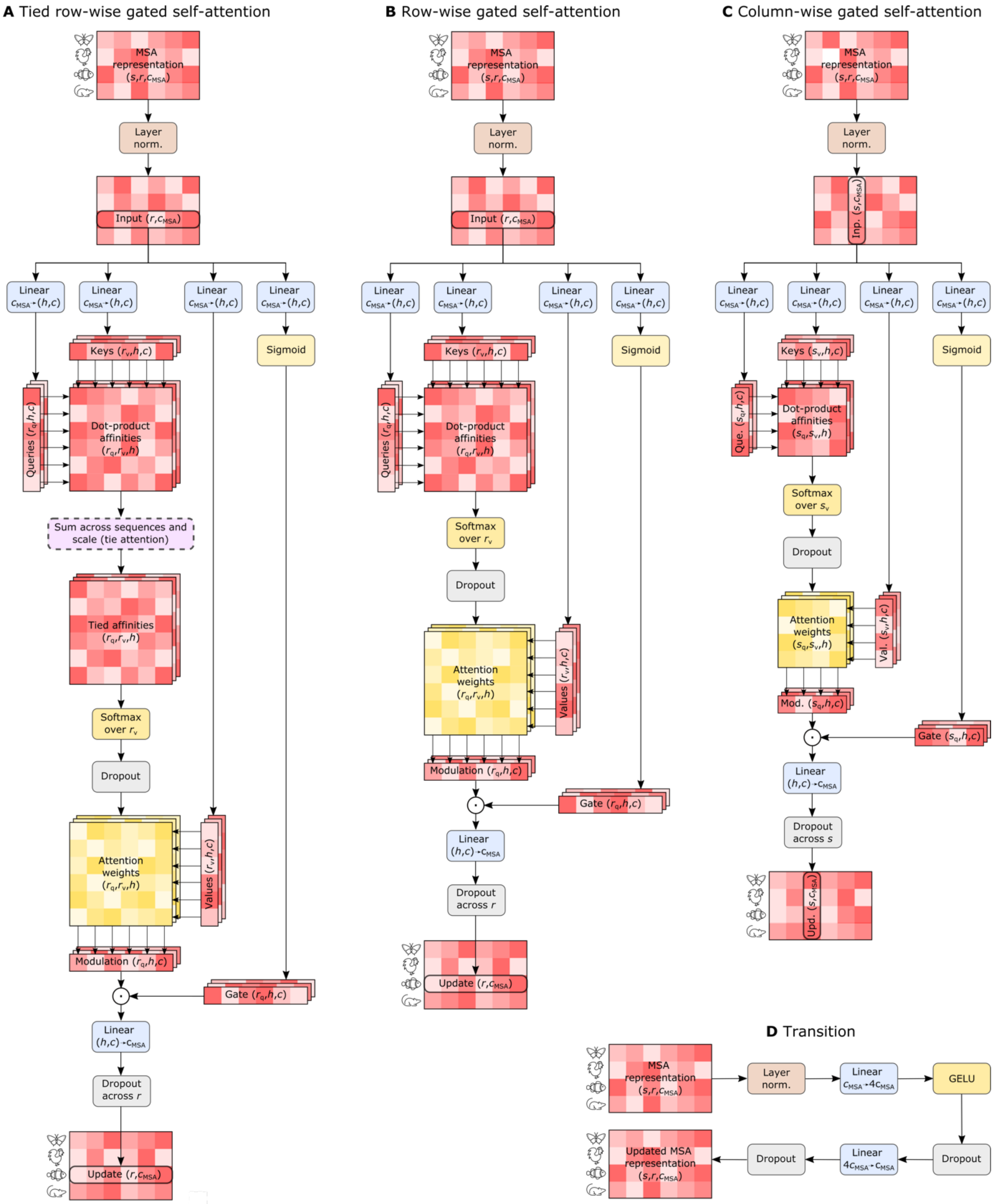

Fig. S25. PrimateAI language model components. (**A**) Tied row-wise gated self-attention. (**B**) Row-wise gated self-attention. (**C**) Column-wise gated self-attention. (**D**) Transition. Dimensions are shown for sequences, $s = 32$, residues, $r = 256$, attention heads, $h = 12$, and channels, $c = 64$ and $c_{\text{MSA}} = 768$.

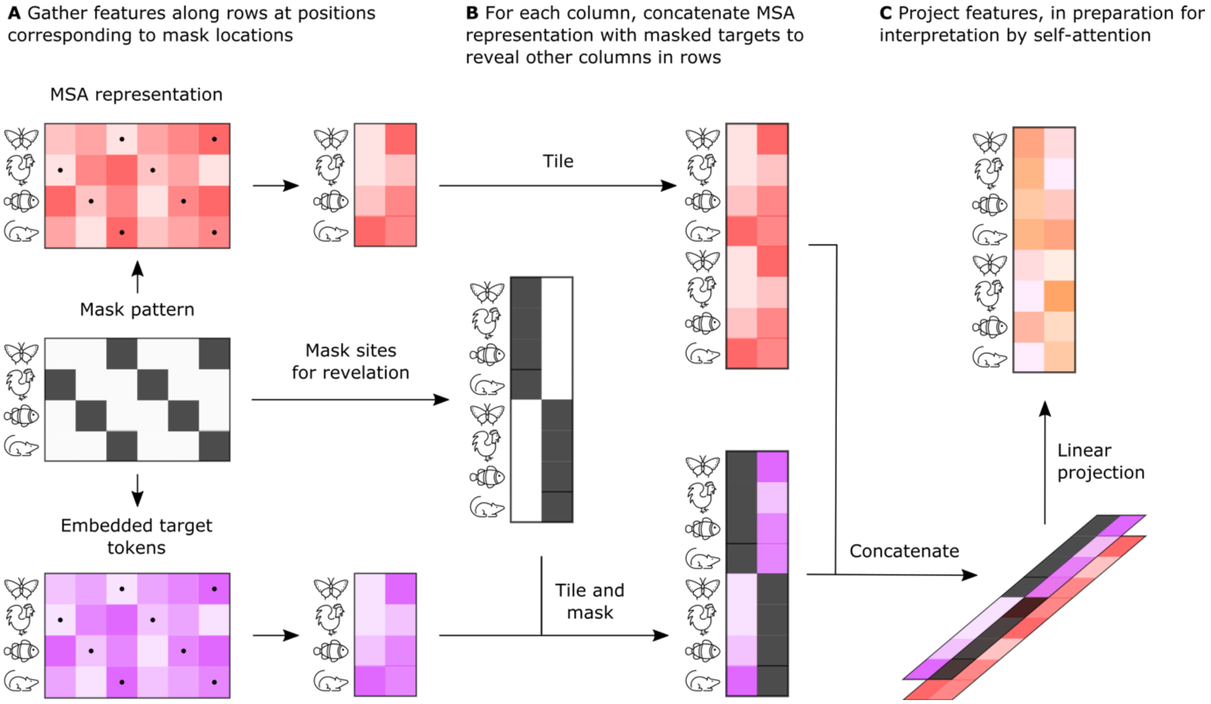

Fig. S26. Mask revelation. (**A**) A mask pattern is used to gather features, indicated with dots, from the updated MSA representation and embedded target tokens. (**B**) For each protein, for each masked residue in that protein, reveal embeddings for residues at other masked locations within that protein. The partially revealed target embeddings are concatenated with the MSA representation and (**C**) linearly projected, in preparation for interpretation by self-attention.

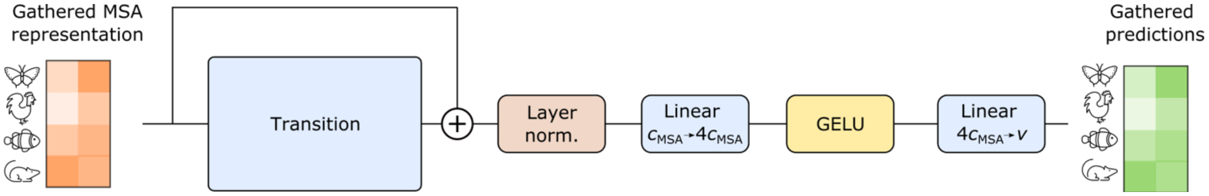

Fig. S27. Revelation output head. Dimensions are shown for channels, $c_{\mathrm{MSA}} = 768$, and vocabulary size, $v = 21$.

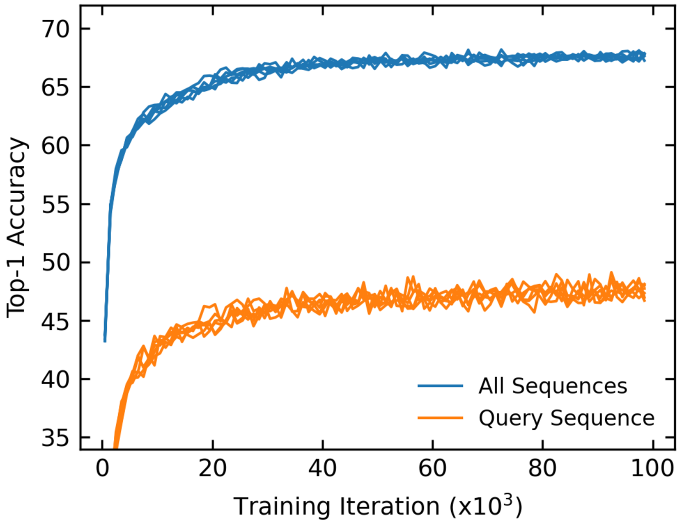

Fig. S28. Top-1 training accuracy. Training accuracies are averaged over 10^3 iteration segments for six PrimateAI LM models used in our ensemble. The accuracies are lower for query sequences, which do not contain gap tokens.

5

Supplemental tables

Table S1. **36 pathogenic ClinVar variants present in primates curated by our clinical laboratory experts.** A variant may occur in multiple species, shown in multiple rows. Curation evidence is provided along with extra information on each variant, including in silico tool predictions, penetrance, hypomorphic or not, recessive/dominant, etc.

Table S2. **Expected and observed counts, inferred selection coefficients, and missense : synonymous ratio deviation for 18,883 human genes.** Expected and observed synonymous counts in humans are in columns exp_syn_h and obs_syn_h, respectively, and expected and observed missense counts in humans are exp_mis_h and obs_mis_h, respectively. Expected and observed synonymous counts in the primate cohort are exp_syn_p and obs_syn_p, respectively, and expected and observed missense counts in the primate cohort are obs_mis_p and exp_mis_p, respectively. Selection coefficients in human and primate are indicated by s_human and s_primate, respectively. Benjamini-Hochberg corrected p-values testing the null hypothesis that s_human = s_primate are provided under p.adj.popgen. MSR regression was only performed on 12,738 genes passing cut offs. Genes that did not pass the cutoff have a low_quality flag set to TRUE. For genes in the MSR regression, the log-scaled deviation from expected MSR is given under MSR_deviation. Benjamini-Hochberg corrected p-values testing the null hypothesis MSR_deviation = 0 are provided under p.adj.MSR.

Table S3. **Performance of PrimateAI-3D and 16 other pathogenicity classifiers on six benchmarking datasets.** Information about the six evaluation datasets (UKBB, DDD, ASD, CHD, ClinVar and DMS assays) is provided, including the number of patients and the number of variants, as well as evaluation methods. Performance metrics of PrimateAI-3D and 16 pathogenicity classifiers are provided in the remaining columns. The average rank of performance across datasets of each method is provided in the last row, with 1 corresponding to the best overall performing across all datasets and a rank of 17 corresponding to the worst.

Table S4. PrimateAI-3D performance on 42 genes with phenotype associations from UKBB. Column “Phenotype” provides 41 phenotypes and column “EnsembleID” provides 42 genes. For each of 78 gene-phenotype pairs, the number of common variants and evaluation metric of PrimateAI-3D (absolute value of Spearman correlation) are provided.

Table S5. **Enrichment of de novo mutations for all genes with >0 nonsynonymous de novo mutations.** P-values are provided for two enrichment tests, one with missense mutations restricted to PrimateAI-3D scores ≥ 0.821, and the other including all missense mutations.

Table S6. Performance of PrimateAI-3D and 16 other pathogenicity classifiers on 9 saturation mutagenesis assays. Absolute value of Spearman correlation of prediction scores of 17 classifiers (rows) with assay measurement across the 9 saturation mutagenesis assays (columns labelled by gene symbol) are provided.